The Improvement of the Battery Thermal Management System of an Electric Vehicle

by
Christoffel Jacobus Vosloo

Thesis presented in partial fulfilment of the requirements for the degree of Master of Engineering (Mechanical) in the Faculty of Engineering at Stellenbosch University

Supervisor: Prof Sybrand Johannes van der Spuy

March 2020

Declaration

By submitting this thesis electronically, I declare that the entirety of the work contained therein is my own, original work, that I am the sole author thereof (save to the extent explicitly otherwise stated), that reproduction and publication thereof by Stellenbosch University will not infringe any third party rights and that I have not previously in its entirety or in part submitted it for obtaining any qualification.

Date: March 2020

Abstract

The increasing cost of fossil fuels, along with the growing concern over climate change, has sparked renewed interest in the research and development of Electric Vehicles (EVs). This thesis focusses on the utilization of Thermosyphon Heat Pipes (THPs) for the purpose of improving an existing Battery Thermal Management System (BTMS) of an EV.

The current battery pack utilizes aluminium plates that are compressed between the Lithium-ion (Li-ion) cells, to serve as the BTMS. These plates have protrusions extending into a cooling channel, to allow heat transfer to the cooling air via forced convection. Problems with heat transfer and temperature uniformity arise, since these protrusions (or fins) are orientated perpendicular to the flow direction. When air is forced over these fins, a low pressure wake is created after the first set of fins, compromising the heat transfer from the fins behind it.

It was decided to implement a THP BTMS that could replace the aluminium plate BTMS without requiring a reconfiguration of the battery pack. Copper fins were brazed to the condenser section in order to increase the heat transfer surface area. These fins were orientated parallel to the flow in order to improve the uniformity of the heat transfer from the fins. It was decided to use methanol as the working fluid as it vaporises easily at low temperatures. The filling ratio of the methanol was calculated to be 30 %.

To compare the new BTMS with the old version, an analytical model was developed of the two BTMSs. These models were improved by incorporating the results of CFD simulations and verified experimentally. To assist in the numerical modelling of the THPs, the THPs were modelled as solid superconductors. The thermal conductivity of these superconductors was calculated to be 3032.9 W/m·K.

To conduct the experiments an existing test bench, similar to the existing battery pack, was modified to accommodate four Li-ion cells along with three THP sections. This small scale experiment was used to determine the thermal characterization of the Li-ion cells and the two different BTMSs, as well as verify the results of the CFD simulations. The experiments were performed for two cases. For the first case the cells were cycled through charging and discharging cycles, in order to increase the cell temperature. After 4 hours the cooling fan was switched on in order to cool down the cells. For the second case the cooling fan was switched on from the start of the first charging cycle. This allowed the cell temperatures to reach a steady state throughout the subsequent charging and discharging cycles.

The utilization of the THP BTMS resulted in a 16 % increase in heat transfer coefficient with a 589 % increase in total heat transfer rate. This resulted in a 5 %

decrease in steady state cell temperature. This shows the potential of using heat pipe technology for the cooling of EV battery packs.

Uittreksel

Die toenemende koste van fossielbrandstowwe, tesame met kommer oor klimaatsverandering, het hernude belangstelling in die navorsing en ontwikkeling van Elektriese Voertuie (EV's) teweeg gebring. Die fokus van hierdie tesis is beperk tot die gebruik van Termohewel Hittepype (THPe) om ‘n bestaande Battery Termiese Bestuur Sisteem (BTBS) te verbeter.

Die huidige batterypak gebruik aluminiumplate wat saamgedruk is tussen die litium-ioon (Li-ion) selle, as die BTBS. Hierdie plate het vinne wat in 'n verkoelingskanaal uitsteek om hitte-oordrag via geforseerde konveksie moontlik te maak. Probleme met hitte-oordrag en temperatuur eenvormigheid ontstaan, aangesien hierdie vinne loodreg op die vloei gerig is. As lug oor hierdie vinne geforseer word, vorm 'n lae druk zone na die eerste stel vinne wat die hitte-oordrag van die agterste vinne negatief beïnvloed.

Daar was besluit om 'n THP BTBS te implementeer wat die aluminiumplaat BTBS kan vervang sonder om die uitleg van die batterypak te herontwerp. Kopervinne is op die kondensor seksie gesoldeer om die hitte-oordrag oppervlakte te vergroot. Hierdie vinne is parallel met die vloei gerig om die eenvormigheid van die hitte-oordrag vanaf die vinne te verbeter. Daar is besluit om metanol as werkvloeistof te gebruik, aangesien dit maklik verdamp by lae temperature. Die vulverhouding van die metanol was bereken as 30 %.

Om die nuwe BTBS met die ou weergawe te vergelyk, was 'n analitiese model van die twee BTBS'e ontwikkel. Hierdie modelle is verbeter deur die resultate van CFD-simulasies in die modelle te inkorporeer en eksperimenteel geverifieer. Om die numeriese modellering van die THPe te vergemaklik, was die THPe as soliede supergeleiers gemodelleer. Die termiese geleiding van hierdie supergeleiers was bereken as 3032,9 W/m·K.

Om die eksperimente uit te voer, was 'n bestaande toetsbank, soortgelyk aan die bestaande batterypak, aangepas om 4 Li-ioon-selle te akkommodeer tesame met 3 hittepyp seksies. Hierdie kleinskaalse eksperiment was gebruik om die termiese karakterisering van die Li-ion-selle en die twee BTBSe te bepaal, asook om die resultate van die CFD-simulasies te verifieer. Die eksperimente was vir twee gevalle uitgevoer. Vir die eerste geval was die selle deur laai- en ontladingsiklusse gesirkuleer om die seltemperatuur te verhoog. Na 4 uur was die verkoelings waaier aangeskakel om die selle af te koel. In die tweede geval is die verkoelings waaier van die begin van die eerste laaisiklus af aangeskakel sodat die temperatuur 'n konstante toestand kon bereik regdeur die laai- en ontlaaisiklusse.

Die gebruik van die THP BTMS het gelei tot 'n 16 % toename in hitte-oordragskoëffisiënt met 'n 589 % toename in die totale hitte-oordragstempo. Gevolglik lei dit tot 'n 5 % afname in die stabiele batterytemperatuur. Die resultate

dui op die potensiële voordele in die gebruik van hittepype vir die verkoeling van EV batterypakke.

Acknowledgements

Special thanks to Prof Johan van der Spuy, for all the hard work, patience, incredible vision and patience throughout the project. It has been a privilege to work under your guidance.

Thank you Ernie, Bartho and the whole Mellowcabs team for their assistance, inputs and all the necessities for the experimental setup. It has been a pleasure working with you.

Thank you to Mr David-John van der Merwe and the people of Cape Heat Exchange with their assistance in manufacturing the thermosyphons.

Thank you Julian, Nathi and Maurisha for all of the additional lab equipment and help with the experimental setup.

Thank you to Mr Carel Landman for his assistance with all the electrical aspects of this thesis.

Thank you to my family and partner for all the love and support throughout this thesis.

Lastly thank you to the Lord for the knowledge and opportunity to study at such a fantastic university.

Contents

List of Figures

Page

List of Tables

Page

Nomenclature

Abbreviations

AC	Alternating Current
ANSYS® Inc.	American computer-aided engineering software developer
ANSYS® Fluent	Computational Fluid Dynamics Software
BTMS	Battery Thermal Management System
BLDC	Brushless Direct Current
CFD	Computational Fluid Dynamics
CFM	Cubic Feet per Minute
DAQ	Data Acquisition
DC	Direct Current
EV	Electric Vehicle
FCC	Face Centred Cubic
HEV	Hybrid Electric Vehicle
ICE	Internal Combustion Engine
I/O	Input/Output
LCO	Lithium Cobalt Oxide
LFP	Lithium Iron Phosphate
Li-ion	Lithium-Ion
$LiFePO_4$	Lithium Iron Phosphate
LMO	Lithium Manganese Oxide
PC	Personal Computer
PLX	Parallax® Inc.
SOC	State of Charge
TDAS	Thermal Data Acquisition System
THP	Thermosyphon Heat Pipe
UMHP	Ultra-thin Micro Heat Pipe

Symbols

A	Area	mm^2
C	C-rate	Ah

c_p	Specific heat	kJ/kg·K
D	Diameter	m
E	E-rate	Ah
f	Darcy friction factor	
F	Faraday number	°C/mol
G	Air mass velocity	kg·m/s
g	Gravitational acceleration	m/s^2
H	Height	m
h	Heat transfer coefficient	$W/m^2·K$
h_{fg}	Latent heat of vaporization	kJ/kg
I	Current	A
i	Current per unit volume	A/m^3
j	Colburn j-factor	
k	Thermal conductivity	W/m·K
	Turbulent kinetic energy	J
L	Length	m
$\dot{m}$	Mass flow rate	kg/s
m	Mass	kg
N	Number	
p	Pressure	Pa
	Perimeter	m
ΔP	Pressure drop	Pa
q	Heat flux	W/m^2
$\dot{Q}$	Heat transfer rate	W
r	Radial coordinate	m
	radius	m
R	Resistance	Ω
	thermal resistance	°C/W
R_g	Gas constant	kJ/kg·K
S_L	Longitudinal pitch	m

s_R	Fin pitch	m
S_T	Transverse pitch	m
ΔS	Change in entropy	kJ/kg·K
T	Temperature	K
	Period	s
t	Time	s
	Thickness	m
t_R	Fin thickness	m
v	Radial component of velocity	m/s
V	Velocity	m/s
	Volume	m^3
	Voltage	V
V^+	Fill ratio	%
W	Width	m
w	Axial component of velocity	m/s
x	Cartesian coordinate	m
y	Cartesian coordinate	m
z	Cartesian coordinate	m

Greek letters

α	Filter strength	
β	Coefficient of thermal expansion	
Γ	Liquid mass flow rate per unit width	kg/m·s
δ	Liquid film thickness	m
ε	Emissivity	
	Specific rate of dissipation	m^2/s^3
μ	Dynamic viscosity	Pas
ξ	Pressure drop coefficient	
ρ	Density	kg/m^3
σ	Stefan-Boltzmann constant	W/m^2K^4

	Area ratio	
υ	Kinematic viscosity	m^2/s
Φ	Source term	
ω	Frequency	Hz
	Specific rate of dissipation	m^2/s^3

Subscripts

0	Free stream
∞	Ambient
a	Adiabatic
act	Actual
b	Base
c	Cold
	Condenser
	Cross section
	Cut-off
$cond$	Conduction
$conv$	Convective
$crit$	Critical
cv	Control volume
Dh	Hydraulic diameter
e	Evaporator
f	Fluid
h	Hot
	hydraulic
i	Inner
	Internal
k	Kinetic energy
l	Liquid
m	Mean
max	Maximum

ncs	Narrowest Cross section
o	Outer
oc	Open Circuit
s	Source
	Sample
sat	Saturation
t	Turbulent
	Total
THP	Thermosyphon Heat Pipe
tot	Total
v	Vapour
	Volume
w	Wall
	Wetted surface area
x	x-direction
y	y-direction
z	z-direction
δ	Liquid film

Dimensionless numbers

Bo	Bond number
Nu	Nusselt number
Pr	Prandtl number
Re	Reynolds number
St	Stanton number

1 Introduction

1.1 Background

The increasing cost of crude oil, along with the growing concern over climate change, has led to an increase in demand for electric and hybrid powered vehicles. Electric Vehicles (EVs) cover a wide range of products from small carts to assist personal mobility, to large vehicles designed to be used for transporting heavy cargo. Today's manufacturers utilise three different types of electrical motors in EVs, namely: the brushless DC motor, brushed DC motor, and AC induction motor. In EVs this motor is powered by a battery pack, where as in Hybrid Electrical Vehicles (HEVs) the electric motor is combined with an internal combustion engine (ICE) to lower the effective emissions of the vehicle. The HEV is driven by the ICE and utilises the electric motor when the efficiency of the ICE is low, for instance during traffic congestion or when additional power is required. In both EVs and HEVs the energy generated during braking is stored in the batteries and used later during acceleration.

The main disadvantages of EVs and HEVs are the added weight of the battery packs and the limited battery range and lifespan. To mitigate some of these shortcomings EVs and HEVs are equipped with a battery thermal management system (BTMS), as the battery temperature directly affects the performance and lifespan of the batteries. The performance parameters that are influenced by battery temperature, are the availability of discharge power (for acceleration) and charge acceptance during regenerative braking. Therefore, ideally, batteries should be operated within an optimum temperature range. This temperature range differs for different battery types.

In addition to the temperature of the battery pack, the temperature distribution should also be considered. An uneven temperature distribution in the modules could lead to a difference in charge or discharge behaviours of the modules. This, in turn, could cause the battery pack to be electrically unbalanced, and therefore reduce the performance of the pack (Panchal, 2016).

The vehicle used as a reference case for this thesis was a small 3-wheeled EV manufactured by Mellowcabs, as shown in Figure 1.1. Mellowcabs was founded in 2012 and is located in Stellenbosch, South Africa. The company manufactures micro EVs to provide a short range taxi service for two passengers or be used as local courier delivery vehicles.

Figure 1.1: A Mellowcabs EV

The battery pack of the vehicle consists of two rows of densely packed Lithium iron phosphate ($LiFePO_4$) cells, manufactured by Liyuan Battery Company Ltd. The cells are separated by aluminium plates that extend into a cooling channel as seen in Figure 1.2. This layout leads to thermal management issues since the heat generated by the $LiFePO_4$ cells are not sufficiently extracted by the BTMS due to the orientation of the aluminium plates in the cooling channel.

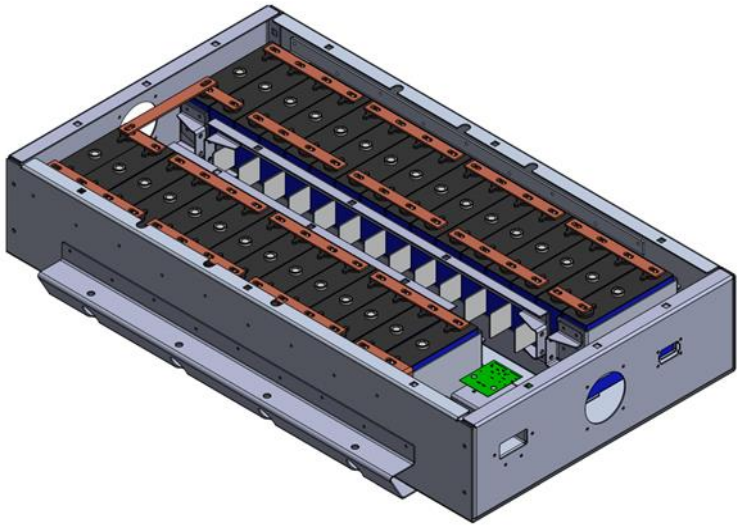

Figure 1.2: The Mellowcabs battery pack

The focus of this thesis was therefore to improve the BTMS currently used in the Mellowcabs EV. This would increase the lifespan and performance of the battery pack (Panchal, 2016). Additionally, the thesis also considered the management of these systems in general. It is foreseen that the usage of EVs, and consequently battery packs, will increase dramatically in the immediate future.

1.2 Objectives

As mentioned in Section 1.1 the primary objective of this research was to improve the BTMS of the Mellowcabs EV, in order to increase the performance and lifespan of the battery pack. It was hypothesised that improving the BTMS would result in improved heat transfer from the system and a more uniform temperature distribution amongst the cells inside the battery pack. The following secondary objectives were formulated to aid in testing the hypothesis for this thesis:

1. Analytically model the current BTMS of the EV to characterise the thermal behaviour of the BTMS.

2. Simulate the current BTMS using Computational Fluid Dynamics (CFD), using the results to improve the analytical model. In the expectation that it would pinpoint the source of the problems associated with the current BTMS.

3. Use the modified test rig developed by Van Zuydam (2018) to perform small scale experiments on the current BTMS to confirm the results of the CFD simulations.

4. Conduct experiments to characterise the thermal behaviour of the Li-ion cells utilized in the Mellowcabs EV.

5. Develop an improved BTMS that is compatible with the current battery layout so that it can be implemented on the battery pack.

6. Repeat objectives 1 to 4 for the improved BTMS. Consideration should be given to the expected cost of implementing the improved BTMS.

7. Compare the improvements in performance and temperature uniformity to determine if the hypothesis was proven correct.

1.3 Thesis Outline

This thesis is organized into nine chapters as follows:

Chapter 2 presents the literature review related to battery definitions, types of lithium-ion cells and their operating requirements, thermal management of batteries (air cooling, liquid cooling, direct refrigerant cooling and the

implementation of heat pipe technology), background and analysis of thermosyphon heat pipes (THPs). Finally some background on the numerical modelling of THPs and turbulence models used in Computational Fluid Dynamics (CFD).

Chapter 3 details the design of the improved Battery Thermal Management System, including the problem description and areas of improvement.

Chapter 4 presents the analytical calculations for the heat generation of Lithium-ion (Li-ion) batteries as well as the heat transfer analysis of the two BTMSs. The first system is the existing aluminium plate BTMS currently utilized in the Mellowcabs Electric Vehicle (EV). The second system is the improved THP BTMS developed for this thesis. The section details the calculation methods and governing equations used for determining the convective heat transfer equation, temperature distribution, pressure drop and overall heat transfer of the two systems.

Chapter 5 presents the numerical solution of the two BTMSs. It details the computational domain created for each system, the computational mesh, the boundary conditions applied to the various named sections, and control parameters implemented in the ANSYS® CFD software.

Chapter 6 introduces an experimental study that includes the design of the electrical circuit and test bench developed to charge, discharge and monitor the Li-ion cells. Experiment 1 details the thermal characterization of the aluminium plate BTMS. Experiment 2 utilizes the same test bench and procedure and details the experimental setup for determining the thermal characteristics of the THP BTMS.

Chapter 7 presents the results and discussions. The first part of this chapter explains the experimental results obtained from the cells in terms of the discharge/charge voltage and heat generation profiles. The second part includes the results of the CFD simulations. It includes the temperature, velocity and pressure profiles, the simulated heat transfer coefficient as well as the overall heat transfer. These results are then validated by the experimental results and used to improve the analytical models of the two BTMSs. The different systems are also compared to each other, in order to determine the success of the thesis.

Chapter 8 summarises the conclusions and presents the recommendations for future work.

2 Literature Study

As part of this literature study, literature sources on battery definitions, Lithium-ion (Li-ion) cells and various Battery Thermal Management Systems (BTMSs), which included previous research related to the use of heat pipe technology as BTMSs, were studied.

2.1 Definitions

The following section explains some of the basic definitions regarding Lithium-ion (Li-ion) batteries.

2.1.1 Battery Basics

Cells, modules and packs – A cell is defined as the smallest, packaged form of a battery. A module is made up of several cells connected in either a series or parallel configuration. Finally a battery pack is created by assembling modules, again either in a series or parallel configuration (MIT Electric Vehicle Team, 2008). Figure 2.1 illustrates the cell module and battery pack configuration of the Mellowcabs Electric Vehicle (EV).

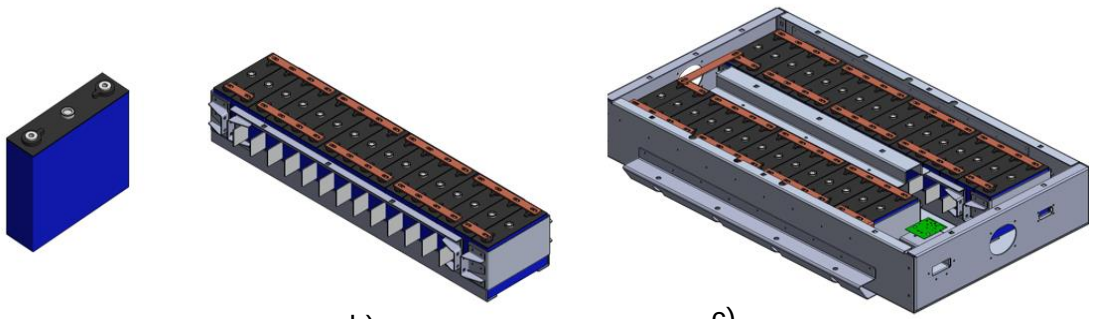

a) b) c)

Figure 2.1: a) The cell, b) module and c) battery pack configuration typical of the Mellowcabs EV

C- and E- rates – The term C-rate is used to express the discharge current of cells. This is normalized against cell capacity, which very often differs between batteries. The C-rate is therefore a measure of the cells discharge rate relative to its capacity and E-rate refers to the battery's discharge power. For instance a cell with a capacity of 100 Ah discharging at 1C will draw a discharge current of 100 A for one hour. A 5 C rate would result in a discharge current of 500 A and a 0.5 C rate would yield 50 A. This is similar for E-rates as a 1E rate is the discharge power required to discharge the entire battery in 1 hour (MIT Electric Vehicle Team, 2008).

Primary and secondary cells – A primary cell is defined as a cell that cannot be charged and a secondary cell is defined as rechargeable (MIT Electric Vehicle Team, 2008).

2.1.2 Battery Conditions

State of charge (SOC)(%) – This refers to the current cell capacity as a percentage of the maximum cell capacity. SOC can be determined by using current integration to determine the change in battery capacity over time (MIT Electric Vehicle Team, 2008). Mohammadian and Zhang (2017) formulated SOC as follows:

$$SOC = 1 - \frac{I\,t}{C} \tag{2.1}$$

where t is the time (in hours) of the charge/discharge cycle, I is the current delivered by or from the battery (in A) and C is the C-rate (in Ah).

Terminal voltage (V) – The voltage between the cell terminals when a load is applied to the cell. This varies with SOC and the charge or discharge current (MIT Electric Vehicle Team, 2008).

Open-circuit voltage (V) – This refers to the voltage between the cell terminals when no load is applied. The open circuit voltage is dependent on the battery SOC and increases with the SOC (MIT Electric Vehicle Team, 2008).

Internal resistance (Ω) – This refers to the resistance within the cell, it mostly differs for charging and discharging cycles and is dependent on the SOC. Cell efficiency and thermal stability decreases with an increase in internal resistance as more of the charging energy is converted into heat (MIT Electric Vehicle Team, 2008).

2.1.3 Battery Technical Specifications

Nominal and cut-off voltage (V) – The reported or reference voltage is referred to as the nominal voltage of the cell, and can be described as the approximate voltage at which the cell is delivering power. This nominal voltage is dependent on the internal resistance, R_i of the cell. Assuming that a current, I is flowing out of a battery, as illustrated in Figure 2.2, then from basic circuit theory the nominal voltage can be expressed as:

$$V = V_{oc} - IR_i \tag{2.2}$$

where V_{oc} is the open circuit voltage (Larminie and Lowry, 2003). The cut-off voltage is defined as the minimum allowable voltage of a Cell. It is the voltage at which a cell is defined as “empty” (MIT Electric Vehicle Team, 2008).

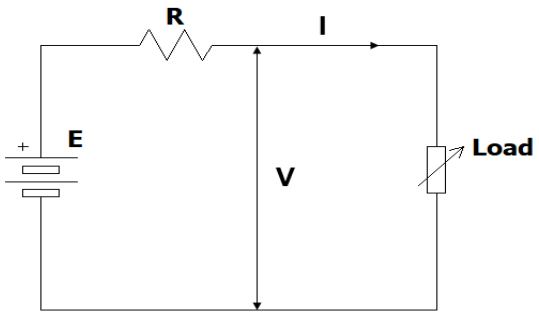

Figure 2.2: Equivalent circuit model of a battery

Nominal Capacity (Ah) – The nominal capacity is referred to as the coulometric capacity and is defined as the total Amp-hours available when the cell is discharged at a specific C-rate. It is calculated by the product of the discharge current (in A) and the discharge time (in hours). The capacity of a cell decreases with an increasing C-rate (MIT Electric Vehicle Team, 2008).

Nominal Energy (Wh) – This represents the energy capacity of the cell. It is defined as the total Watt-hours available when the cell is discharged at a specific C-rate. The energy is calculated by the product of the discharge power (in W) and the discharge time (in hours). Like capacity, energy also decreases with an increase in the C-rate (MIT Electric Vehicle Team, 2008).

Specific Power (W/kg) – The specific power of a cell is highly variable, since the power delivered by the cell depends far more on the load connected to it than the cell itself. It can be defined as the maximum available power per unit mass of the cell (MIT Electric Vehicle Team, 2008; Larminie and Lowry, 2003).

Specific Energy (Wh/kg) – Defined as the nominal cell energy per unit mass of the cell (MIT Electric Vehicle Team, 2008). Some cells have a high specific energy but low specific power. This results in the cell being able to store a lot of energy, but only being able to supply it at a low rate (Larminie and Lowry, 2003).

Energy Density (Wh/m^3) – This represents the volumetric energy density, defined as the nominal cell energy per unit volume. It is highly dependent on the chemistry of the cell (MIT Electric Vehicle Team, 2008).

Power Density (W/m^3) – Defined as the nominal cell power per unit volume, and is highly dependent on the cell chemistry (MIT Electric Vehicle Team, 2008).

Cycle Life – This alludes to the number of times a cell can be charged and discharged before it fails to meet specific performance criteria. This is usually when its nominal capacity falls below 80% of its original value (Larminie and Lowry, 2003).

2.2 Lithium Ion Batteries

Lithium-ion (Li-ion) batteries are considered an attractive energy storage option for HEVs, EVs and various other alternative energy sources, for example solar and wind. It has several advantages (Panchal, 2016): i) high power and energy densities; ii) high nominal voltages; and iii) long cycle lives. The Mellowcabs EV used in this thesis utilises Lithium Iron Phosphate ($LiFePO_4$) cells as the vehicle's energy storage medium.

2.2.1 Lithium-Ion cell operation

A Li-ion cell typically consists of two current collectors (a positive and negative current collector) and two electrodes (the anode and cathode). The anode and cathode are separated by a liquid electrolyte soaked in a polymer separator which conducts the lithium ions during charging and discharging (Panchal, 2016). An example of the layout of a Li-ion cell can be seen in Figure 2.3.

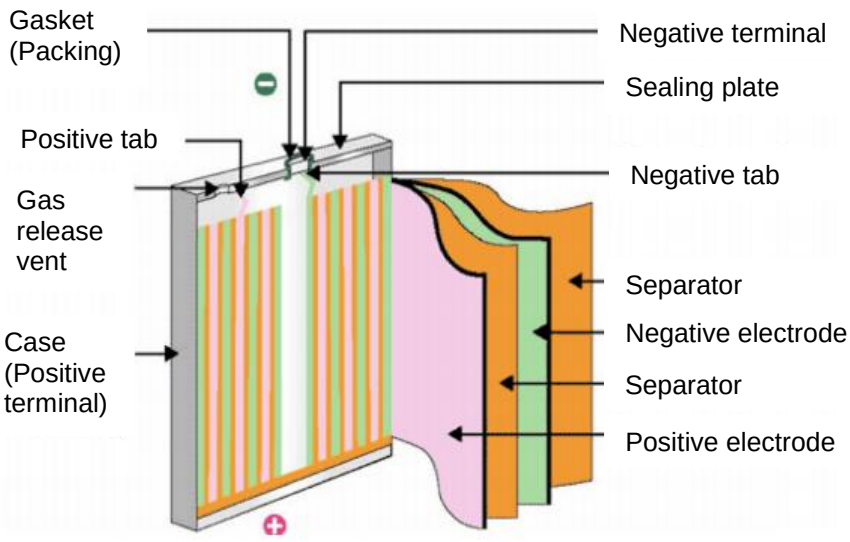

Figure 2.3: Structural layout of a Li-ion cell (Zhu, 2014)

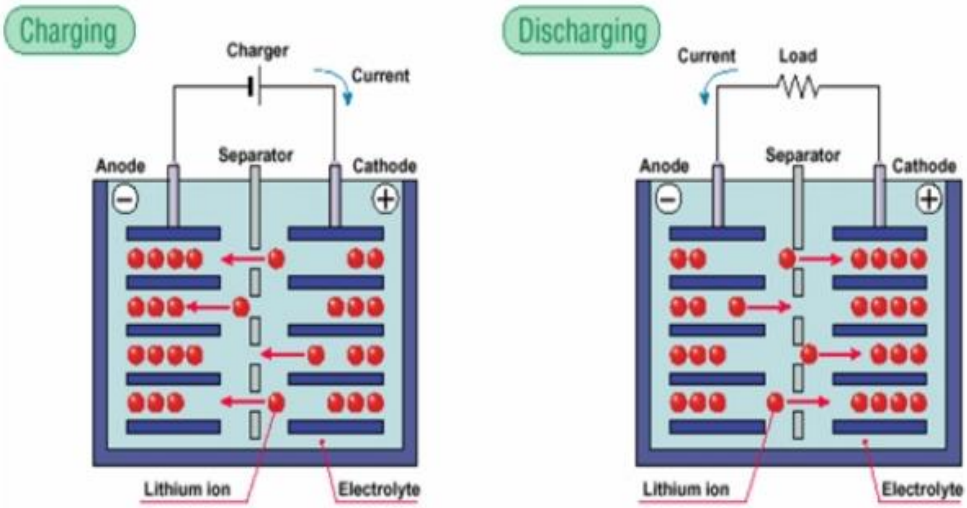

Figure 2.4: Working principle of a Li-ion cell (Marques, 2014)

Figure 2.4 illustrates the working principle of a Li-ion cell. The Li-ion cell utilises a lithiated transition metal intercalation oxide for its anode and lithiated carbon for the cathode (Larminie and Lowry, 2003). The overall chemical reaction for the cell is defined as:

$$C_6Li_x + M_yO_z \leftrightarrow 6C + Li_xM_yO_z \quad (2.3)$$

During a Li-ion cell's discharge cycle, the anode releases Li-ions which travel through the liquid electrolyte toward the cathode. When the Li-ions reach the cathode, the Li-ions react chemically with the cathode and surrounding electrolyte. The lithium ions are then incorporated into the cathode material. This process is easily reversible resulting in quicker charge and discharge times than other battery types. In addition, Li-ion cells have a higher specific energy level than other cell types, allowing for more cells to be used in an EV battery with a limited total weight. This increases the amount of energy stored and therefore increases the vehicle's range (Dhameja, 2002).

2.2.2 Types of Lithium-ion batteries

The cathode material defines the name of the Li-ion cell. This subsection discusses three of the most popular types of cathode materials used in EV batteries, namely:

Lithium Manganese Oxide ($LiMn_2O_4$) – Also referred to as an LMO. The cathode material has a cubic spinal structure as shown in Figure 2.5. The oxygen atoms are located the corners of each tetrahedron and octahedron. Due to this three dimensional spinal structure the cell has a much lower internal resistance (Panchal, 2016).

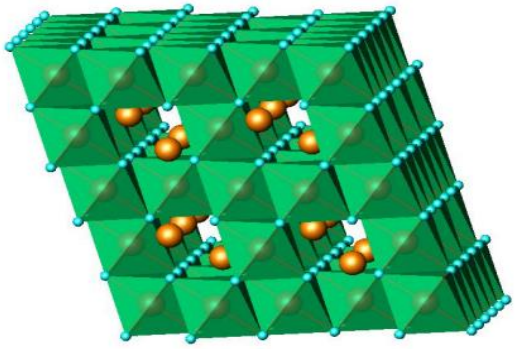

Figure 2.5: Cubic spinal structure of a $LiMn_2O_4$ cathode (Zhu, 2014)

The theoretical specific capacity of a LMO cell is 148 mAh/g, current cells achieve a discharge capacity between 115 and 130 mAh/g at a 1C rate or less (Panchal, 2016).

Lithium Cobalt Oxide ($LiCoO_2$) - Or LCO for short. This is the most commonly used cathode material. This type of cathode features a layered compound. The oxygen anions form a close packed face centred cubic (FCC) lattice with the cations situated in the 6-coordinated octahedral site (Zhu, 2014), as shown in Figure 2.6.

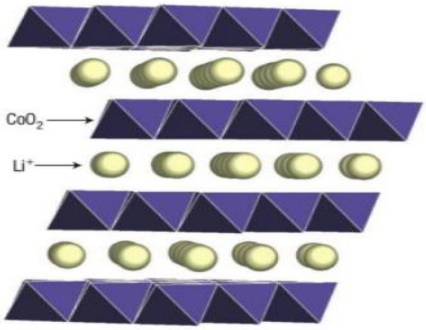

Figure 2.6: Layered structure of a $LiCoO_2$ cathode (Delmas et al., 2003)

LCO cells have a good discharge capacity capable of supplying 136 mAh/g at a 5C rate. The high chemical potential of lithium associated with the highly oxide cobalt cathode provides a high cell voltage of around 4V. However cobalt is relatively expensive compared to other cathode materials, despite all the attractive electrical properties of LCO cathodes (Panchal, 2016; Zhu, 2014). According to Dhameja (2002) the cathode equation during charging is expressed as:

$$LiCoO_2 \rightarrow xLi^+ + xe^- + Li(1-x)CoO_2 \qquad (2.4)$$

And the cathode equation during discharge:

$$xLi^+ + xe^- + Li(1-x)CoO_2 \rightarrow LiCoO_2 \quad (2.5)$$

where x represents the number of electrons dispersed and inserted.

Lithium Iron Phosphate ($LiFePO_4$) – Also referred to as LFP. This cathode material has an olivine structure with high inherent stability. This delays the oxygen loss traditionally occurring in layered or spinel oxides, resulting in a long cycle life (Zhu, 2014). An illustration of this olivine structure is presented in Figure 2.7.

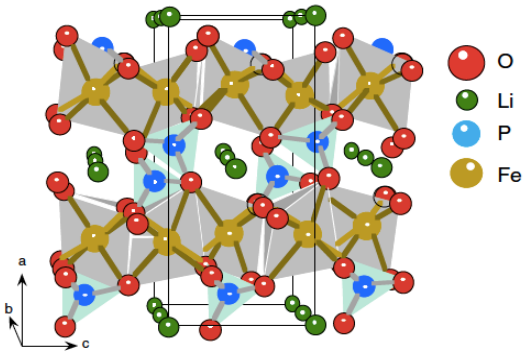

Figure 2.7: Olivine structure of a LiFePO4 cathode (Zhu, 2014)

LFP cells have a theoretical specific capacity of 170 mAh/g and is capable of achieving a discharge of 129 mAh/g at a 10C rate. It is also more environmentally friendly and less expensive than other cell types (Panchal, 2016). According to Li et al. (2012)the extraction of lithium to charge the cathode is expressed as:

$$LiFePO_4 - xLi^+ - xe^- \rightarrow xFePO_4 + (1-x)LiFePO_4 \quad (2.6)$$

During discharge the insertion of lithium into the cathode is expressed as:

$$FePO_4 + xLi^+ + xe^- \rightarrow xLiFePO_4 + (1-x)FePO_4 \quad (2.7)$$

where x represents the number of electrons dispersed and inserted.

2.2.3 Operating Requirements of Li-ion Batteries

In order for EVs to operate at maximum performance and efficiency, it is important that the cell temperatures in the battery pack remain uniform and within the desired temperature limits. This will avoid thermal runaway, improve the performance and cycle life of the cells. According to Li and Zhu (2014) these temperature limits should typically be between 20 °C and 40 °C.

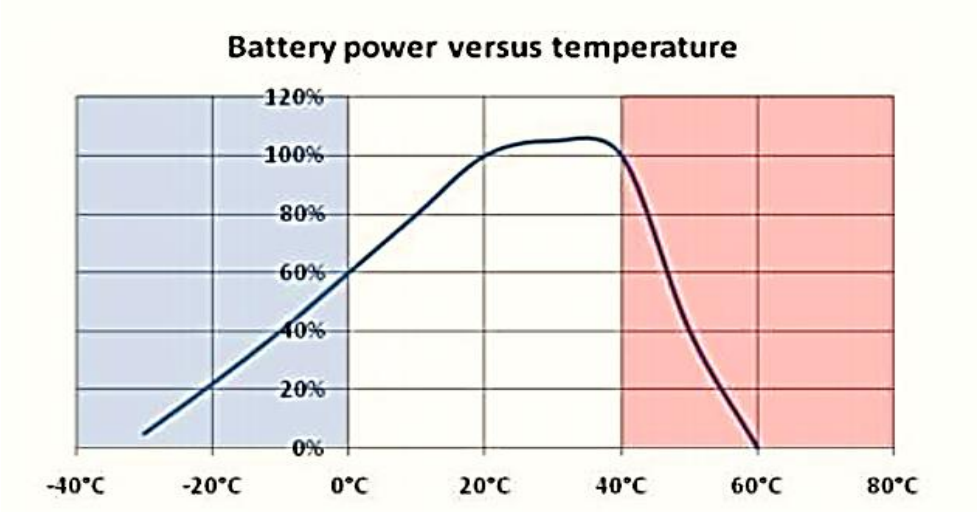

Figure 2.8: Li-ion battery cycle life vs temperature (Matthe et al., 2011)

From Figure 2.8 it is clear that the battery power output decreases once the cell temperature drops below 20 °C, this is due to lithium plating on the anode. When the cell temperature exceeds 40 °C the cycle life rapidly decreases due to the breakdown of the electrode materials (Li and Zhu, 2014). In addition to this, uneven temperatures between the individual cells would result in uneven power distribution and SOC misbalance. This misbalance may produce accelerated cell aging as the difference in temperatures can cause certain cells to discharge faster/slower than others, which would impair the life of the whole battery.

2.3 Thermal Management of Batteries

The following subsections will look at the different thermal management systems currently available. It should be noted that there will always be trade-offs between performance, lifespan, cost and functionality.

2.3.1 Air Cooling

Air cooling systems utilize air as the working fluid. The intake air could either be derived from the cabin of the vehicle or the atmosphere. A direct air system utilises ambient air to cool the battery, whereas an indirect system conditions the air with either a heater or evaporator, therefore offering additional heating or cooling power. Air systems can also be used to heat the battery in cases of very low ambient temperatures, where it makes use of a heat recovery system (Li and Zhu, 2014). Figure 2.9 illustrates a schematic of an air cooling system with heat recovery.

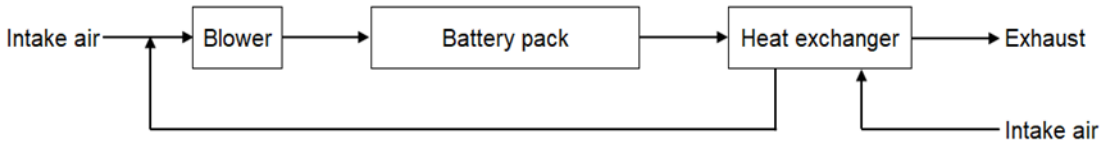

Figure 2.9: Forced air system with heat recovery

2.3.2 Liquid Cooling

Liquid systems are also categorized into direct and indirect systems. indirect systems have no ability to heat and it uses a radiator as a heat sink. The heat transfer medium is circulated in a closed loop by means of a pump. Heat is absorbed by the fluid from the battery pack and released via the radiator. This system relies heavily on the difference in temperature between the ambient air and the battery. If this difference becomes too small the system will become ineffective (Li and Zhu, 2014). The schematic description of a passive liquid system can be seen in Figure 2.10.

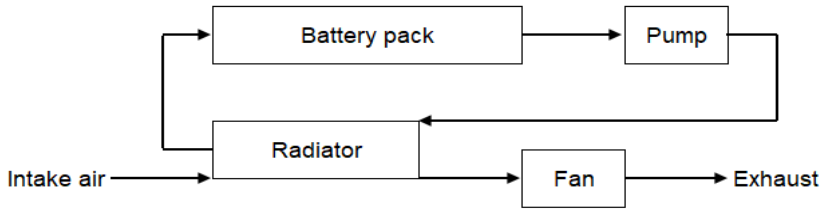

Figure 2.10: Indirect Liquid Cooling

Direct liquid systems utilize two loops, namely a primary and secondary loop. The primary loop is similar to that of a indirect liquid system with the fluid being circulated by a pump. The secondary circuit is an air conditioning loop with the upper heat exchanger functioning as a cooling evaporator. The evaporator heat exchanger connects the two loops. There is also a 4-way valve that switches to enable the upper heat exchanger working as a condenser, for heating operation (Li and Zhu, 2014). A schematic description of this system can be seen in Figure 2.11.

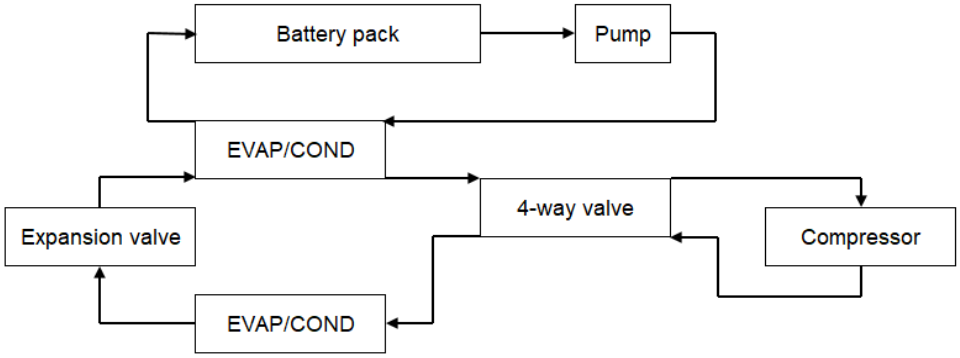

Figure 2.11: Direct Liquid Cooling

2.3.3 Direct Refrigerant Cooling

According to Li and Zhu (2014) direct refrigerant cooling works similar to an active liquid system and consists of an air conditioner loop that uses the refrigerant directly as a heat transfer medium. Figure 2.12 illustrates the schematic layout of a direct refrigerant cooling system.

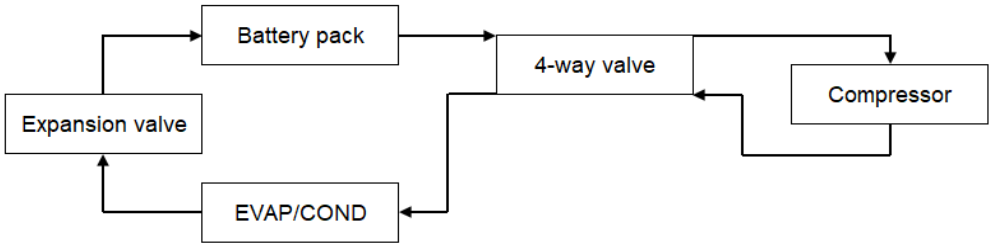

Figure 2.12: Direct Refrigeration System

2.3.4 Heat-pipe based cooling

In addition to the cooling systems mentioned above, heat pipe technologies have recently been receiving significant attention for use in high efficiency battery cooling systems. Air cooling systems are widely utilised because of their uncomplicated installation and low cost (He and Xu, 2013). However, non-uniform temperatures still exist in the battery packs even when using a forced air supply (Fan et al., 2013). Liquid cooling systems usually have a higher heat transfer coefficient and cooling or heating capacity than air cooling systems. However the cost, weight, energy consumption and maintenance complexity are increased due to the inclusion of pumps, heat exchangers, valves and tanks (Chen and Li, 2014). Heat pipes (HPs) are well known for their high efficient phase change heat transfer. Some of the research conducted is summarized below:

Rao et al. (2013) studied the cooling effect of a BTMS with oscillating heat pipes (OHP) for EVs. For these experiments the heat generating power was regulated by adjusting the voltage and current through an aluminium made heater (the same size as a real $LiFePO_4$ cell). An adiabatic environment was created around the heater to maintain the temperature surrounding the evaporator section of the heat pipes, similar to the conditions of a battery pack in an EV. Four heat pipes were dispersed evenly and attached to the surface of the heater with silica (ZC-801). The heat pipes were made from 5 mm copper tube. The evaporator sections of the heat pipes were flattened. The heat pipes had a wick structure of 0.9 mm. A vacuum pump was used to create a vacuum. Whilst the liquid filling ratio was controlled around 50 %, utilising water as the working fluid. The temperature measurements were then taken using k-type thermocouples. The experimental layout can be seen in Figure 2.13.

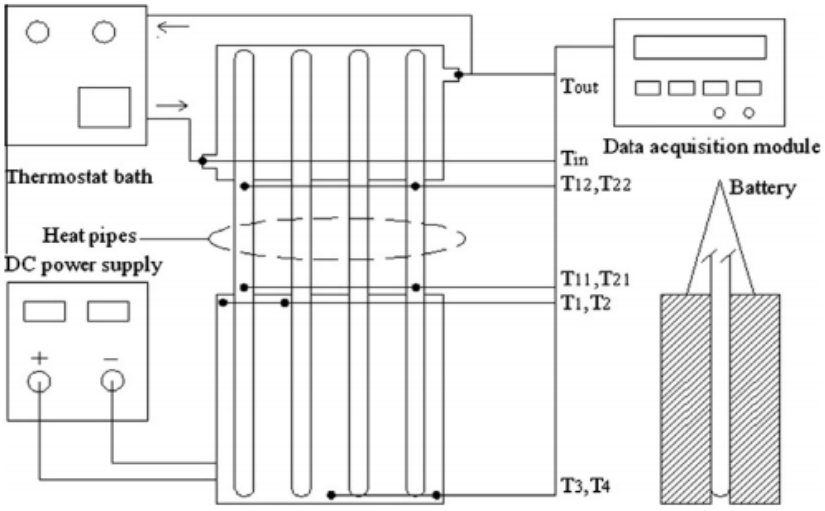

Figure 2.13: Experimental setup of Rao et al. (2013)

Figure 2.14 illustrates the experimental results of Rao et al. (2013). From this figure: a) it is clear that when the heater was loaded with less than 30 W the heat pipes started to cool down the heater, as seen by the cell temperature (red) and temperature difference (black) curves. This meant the temperature and temperature difference were maintained within the desired range, and b) it can be seen that the temperature and temperature difference were below 40 °C and 5 °C, respectively. It was therefore concluded that for most EVs with slow charging and discharging rates, the heat pipes based BTMS is sufficient. For fast charging batteries the heat pipes would still effective, if well designed.

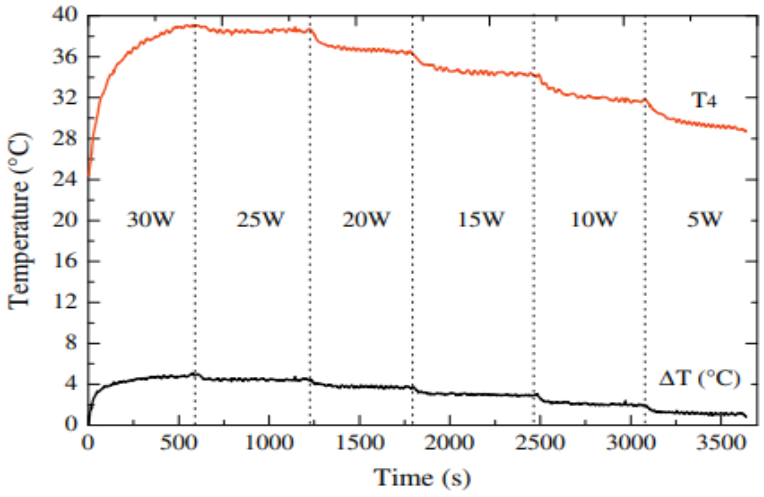

Figure 2.14: Experimental results of Rao et al. (2013)

Chen et al. (2018) experimentally investigated the cooling and heating characteristics of Ultra-thin Micro Heat Pipes (UMHPs) for the thermal management of an EV battery pack. The experiments involved connecting five 3.2 V 50 Ah Li-ion cells in parallel with four sets of three UMHP in between as seen in Figure 2.15.

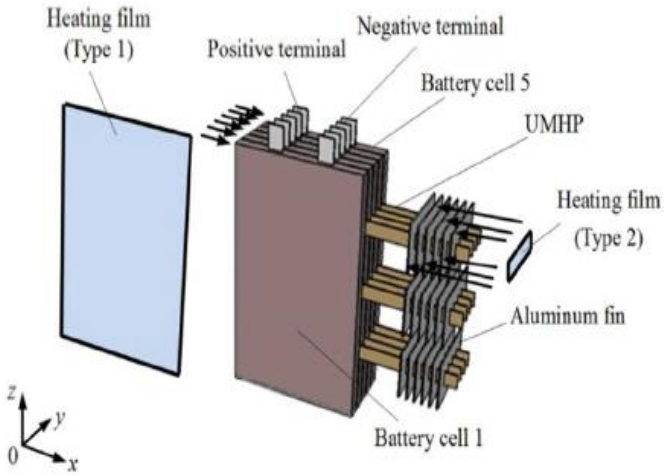

Figure 2.15: UMHP BTMS developed by Chen et al. (2018)

The cells were charged and discharged at constant rates ranging from 1C to 3C and special heating films were placed between each cell and on the finned condenser section of the UMHPs to preheat them to certain temperatures. The temperature measurements were taken with 20 k-type thermocouples attached to various locations on the cells and heat pipes. The temperature curves of this

experiment are shown in Figure 2.16. In this figure it is shown that without the addition of the UMHPs the cell temperatures varied from 30 to 52 °C during the different charge and discharge cycles. However the addition of the UMHPs indicated a substantial improvement, with the maximum temperature of the cells only reaching 38 °C, thereby ensuring the cells operate within the desired temperature range of 20 to 40.

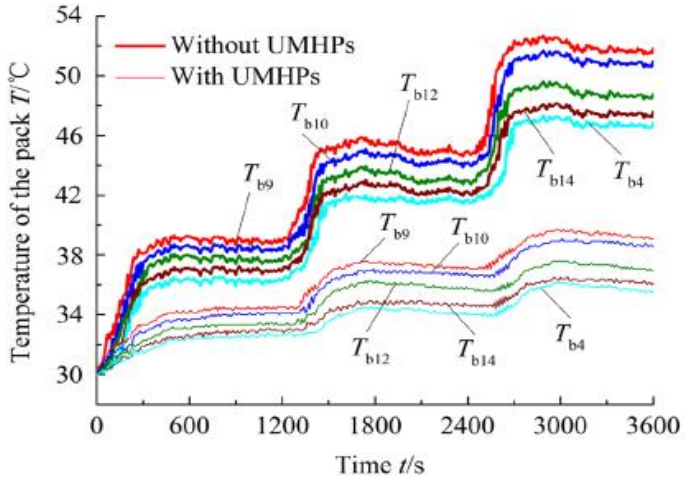

Figure 2.16: Comparison of the experimental results by Chen et al. (2018)

Desmet et al. (2014) evaluated the thermal behaviour of a HEV battery pack when using flat heat pipes at different orientations. Like Rao et al. (2013) a heater plate was used to simulate the heat flux of a battery. Two systems were compared the first being a simple copper heat sink, whilst the second utilized a heat sink attached to the condenser side of a flat heat pipe as illustrated by Figure 2.17.

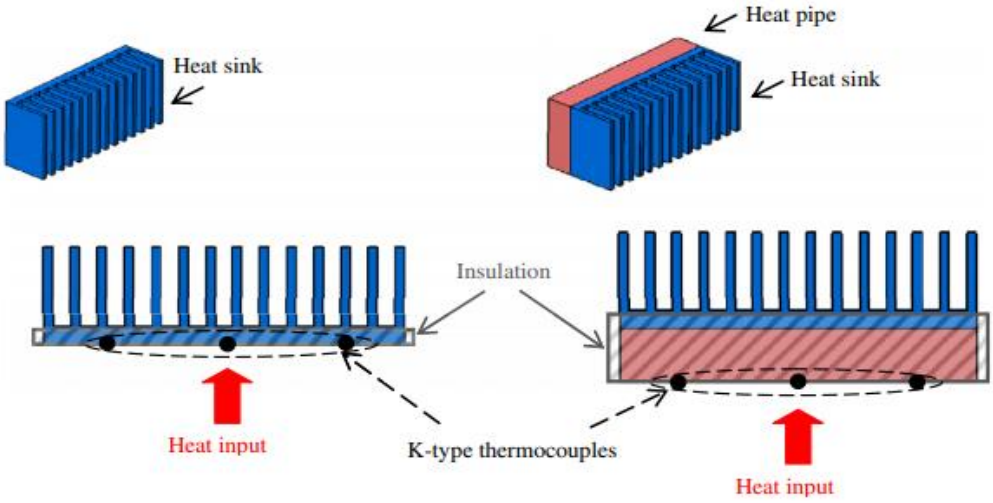

Figure 2.17: The two experiments conducted by Desmet et al. (2014)

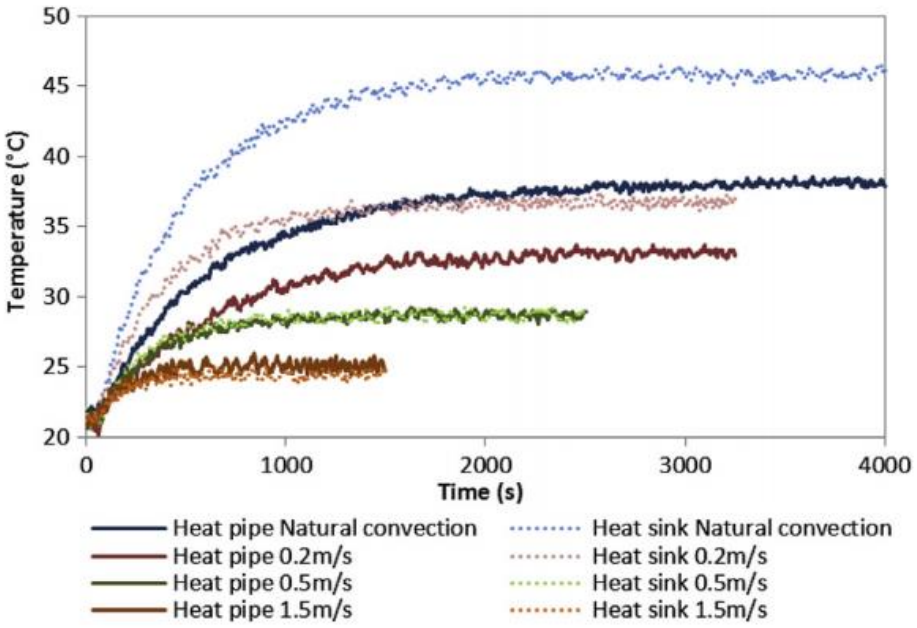

Figure 2.18: Comparison of the experimental results by Desmet et al. (2014)

Figure 2.18 presents the experimental results obtained by Desmet et al. (2014). The temperatures at the heating/cooling interface of both systems were investigated for different airflow rates over the heatsink. In this figure, one can clearly see that there is a distinct difference in temperature at this interface between the two systems at low air flow rates. The two systems provide very similar temperatures at higher air flow rates with no clear improvement. The addition of the flat heat pipes also ensured that the heater remain in the desired temperature range of 20 °C to 40 °C.

2.4 Thermosyphon Heat pipes

2.4.1 Background

A normal heat pipe is typically made up of a sealed metal pipe containing a wicking structure filled with a small amount of working fluid. Heat pipes typically consist of three sections, namely, an evaporator section, a condenser section and an adiabatic section. When heat is applied to the evaporator section, the working fluid in the wick structure vaporises and flows to the cooler condenser section where it gives up its latent heat of evaporation and condenses. Capillary forces in the wick structure then “pump” the condensate back to the evaporator section (Dunn and Reay, 1994). Thermosyphon heat pipes (THP) on the other hand, are essentially heat pipes without the wick structure, thus relying on gravity to return the condensate back to the evaporator section. The THP must be orientated such that the evaporator section is below the condenser section to ensure that the

condensate can return to the evaporator (Dobson and Meyer, 2006). Figure 2.19 illustrates the differences between HPs and THPs.

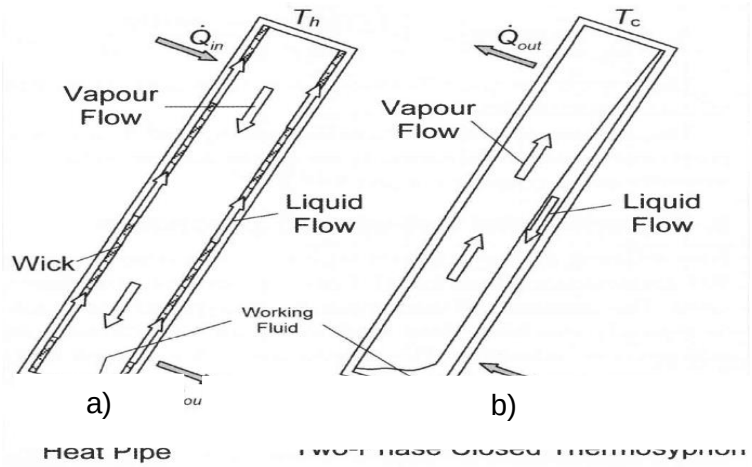

Figure 2.19: The principle difference between a) a heat pipe, and b) a thermosyphon heat pipe (Dobson and Meyer, 2006)

It has been proven that when under the correct orientation, THPs are preferred to HPs. This is based on the grounds that the wick structure in a HP could increase the resistance to the flow of the condensate (Pioro and Pioro, 1997). THPs have a very high thermal conductance. According to Russwurm (1980) THPs and HPs can conduct up to a thousand times more heat, under optimal conditions, than a solid copper tube of the same diameter. It is due to this trait that the application of heat pipe technology in BTMSs has been receiving more attention.

2.4.2 Simplified heat transfer in THPs

The thermal resistance diagram of a single THP is shown in Figure 2.20. In this figure heat transfer occurs between a heat source and the wall of the evaporator section. The heat is then transferred into the working fluid and out through the condenser wall into a heat sink.

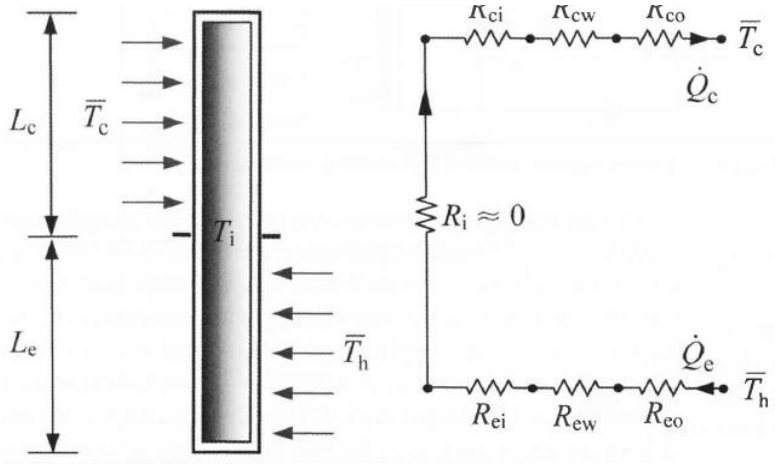

Figure 2.20: Thermal resistance diagram of a THP (Dobson and Meyer, 2006)

The heat transfer rate may then be expressed as the temperature difference divided by the sum of a series of thermal resistances as:

$$\dot{Q} = \frac{\overline{T}_h - \overline{T}_c}{\sum R} = \dot{Q}_e = \frac{\overline{T}_h - \overline{T}_i}{\sum R_e} = \dot{Q}_c = \frac{\overline{T}_i - \overline{T}_c}{\sum R_c} \tag{2.8}$$

where $\overline{T}_h$ is the average temperature of the heat source, $\overline{T}_c$ is the average temperature of the heat sink, $\sum R = R_e + R_c$, $\sum R_e = R_{eo} + R_{ew} + R_{ei}$ and $\sum R_c = R_{co} + R_{cw} + R_{ci}$. These thermal resistances can be expressed as follows:

$$R_{eo} = \frac{1}{h_{eo}A_{eo}}, R_{ew} = \frac{\ln(d_o/d_i)}{2\pi k L_e}, R_{ei} = \frac{1}{h_{ei}A_{ei}}$$

$$R_{co} = \frac{1}{h_{co}A_{co}}, R_{cw} = \frac{ln(d_o/d_i)}{2\pi k L_c}, R_{ci} = \frac{1}{h_{ci}A_{ci}}$$

$$A_{eo} = \pi d_o L_e, \quad A_{ei} = \pi d_i L_e, \quad A_{co} = \pi d_o L_c, \quad A_{ci} = \pi d_i L_c$$

According to Dobson and Meyer (2006), if the temperature differences over the heat source and heat sink are known along with the mass flow rates of the fluids used, then in accordance with the conservation of energy, the condenser and evaporator section heat transfer rates can be calculated as:

$$\dot{Q}_e = \dot{m}_e c_p \Delta T_h \pm \dot{Q}_{loss/gain} \tag{2.9}$$

and

$$\dot{Q}_c = \dot{m}_c c_p \Delta T_c \pm \dot{Q}_{loss/gain} \tag{2.10}$$

where

$$\dot{Q}_{loss/gain} = \left(h_{c,wall} + h_{r,wall}\right)A(T_{wall} - T_{amb}) \tag{2.11}$$

The heat lost or gained from the environment, $\dot{Q}_{loss/gain}$, accounts for the heat transfer losses from the working fluid in the evaporator and condenser section. The free convection, $h_{c,wall}$, and radiative, $h_{r,wall}$, heat transfer coefficients can be determined from correlations by Mills and Ganesan (1999). The free convection heat transfer coefficient is determined from the Nusselt number (Nu) which for natural convection is reliant on the shape of the heat source/heatsink and the Rayleigh number (Ra). However the radiative heat transfer coefficient can be defined as:

$$h_{r,wall} = 4\varepsilon\sigma {T_m}^3 \tag{2.12}$$

where ε is the emittance, σ the Stefan-Boltzmann constant defined as $(5.67 \times 10^{-8}\ W/m^2K^4)$ and T_m the mean temperature of the body. According to Faghri (1995) the average heat transfer coefficients, between the working fluid and the wall, in the evaporator and condenser sections can be expressed as follows:

$$\bar{h}_e = \frac{4}{3}\left[\frac{{\rho_l}^2 {k_l}^3 g h_{fg}}{4\mu_l\left(T_{w,e} - T_i\right)L_e}\right]^{1/4} \tag{2.13}$$

$$\bar{h}_c = \frac{4}{3}\left[\frac{{\rho_l}^2 {k_l}^3 g h_{fg}}{4\mu_l\left(T_i - T_{w,c}\right)L_c}\right]^{1/4} \tag{2.14}$$

Where ρ_l is the density, μ_l the viscosity, h_{fg} the latent heat of evaporation and k_l the thermal conductivity of the working fluid. The different heat transfer coefficients can also be determined experimentally by rearranging equation 2.8. The external heat transfer coefficients h_{co} and h_{eo} can also be determined using well known correlations from text books such as Ganesan and Mills (1999).

2.4.3 Limitations

The heat transfer limitations of THPs include flooding, dryout and boiling. Where flooding is as a result of the interfacial shear stress between the counter current liquid and vapour flows. Dryout is caused by a shortage of working fluid required to carry a specific heat rate. Boiling occurs as a result of a vapour bubble covering a section of the pipe wall, causing damage to the THP (Faghri, 1995).

Dryout

To illustrate this, consider an almost horizontal thermosyphon with a rivulet of working fluid traveling from the condenser to the evaporator section. When the rivulet reaches its lowest point in the evaporator section, severe evaporation

occurs as a result of nucleate boiling, which sprays droplets over the unwetted surface. This evaporation causes a temporary receding of the rivulet. It should be noted that dryout oscillation is not a limitation of heat transfer (Faghri, 1995). The critical heat input at which dryout will occur can be calculated from the following improved equation developed by (Bayley and Cohen, 1955):

$$\frac{q_{crit}}{\rho_v h_{fg}}\left[\frac{g\sigma(\rho_l-\rho_v)}{{\rho_v}^2}\right]^{-1/4} = AB^3C^3 \tag{2.15}$$

where

$$A = \frac{g{\rho_l}^2(D_c/D_e)}{3\mu L_e\sqrt[4]{g\sigma{\rho_v}^2(\rho_l-\rho_v)}}$$

$$B = \frac{V_t/\pi D_c}{4L_c/5 + L_{ac} + (D_e/D_c)^{2/3}(L_{ae}+3L_e/4)}$$

$$C = \frac{(V_e/V_t)(V') - \rho_v/\rho_l}{1-\rho_v/\rho_l}$$

where D_e, D_c, L_e and L_c refers to the evaporator and condenser diameters and lengths respectively. L_{ac} and L_{ae} is the adiabatic length to the centre of the condenser and evaporator section respectively. The liquid fill volume is presented by V'.

Boiling

When the fill amount is moderately high, the heat input upon startup may be insufficient to result in steady nucleate boiling. The temperature of the fluid in the liquid pool will increase until it is superheated, at which point a vapour bubble will appear somewhere inside the liquid pool and grow until its size is the same as the diameter of the tube. This bubble will continue to grow in size and propel the liquid slug towards the condenser end cap. This sudden burst will cause the vapour above the liquid slug to subside and the liquid slug may hit the condenser end cap and fall back down. While this condition is usually a temporary, it could cause the container to rupture if it occurs frequently (Faghri, 1995). The maximum heat flux at which boiling will occur is given by Gorbis and Savchenkov (1976) as

$$\frac{q_{max}}{q_{max,\infty}} = C^2\left[0.4 + 0.01R\sqrt{\frac{g(\rho_l-\rho_v)}{\sigma}}\right]^2 \tag{2.16}$$

where $q_{max,\infty}$ is the critical heat flux for pool boiling, defined as:

$$q_{max,\infty} = 0.142\sqrt{\rho_v}[g\sigma(\rho_l-\rho_v)]^{1/4} \tag{2.17}$$

The coefficient C in equation 2.47 is

$$C = A\left(\frac{D}{L_c}\right)^{-0.44}\left(\frac{D}{L_e}\right)^{0.55} V^{+n}$$

Where $V^{+}$is the fill ratio, and D the inside diameter of the thermosyphon. The coefficient A and power n may be defined as follows

$$V^{+} \leq 0.35: \;\; A = 0.538, \;\; n = 0.13$$

$$V^{+} > 0.35: \;\; A = 3.54, \;\; n = -0.37$$

Flooding

This is interpreted as the dryout of the evaporator section as a result of the interfacial shear between the vapour and liquid that prevents the liquid film from falling to the condenser section. This causes large temperature and vapour pressure swings within the thermosyphon. At very high rates, the liquid-vapour interfacial shear stress results in liquid droplets being torn from the falling film, this is referred to as entrainment. Entrainment is not deemed a limitation of operation since the thermosyphon continuous to operate under these conditions. During operation a significant amount of vapour will become entrained such that dryout will begin to occur in the region preceding the liquid pool. This causes a decrease in vapour pressure. When the liquid film overcomes the interfacial shear, the film falls back down reflooding the evaporator. If this behaviour continuous to oscillate it is referred to as the flooding limit (Faghri, 1995). According to Chen et al., (1989) the maximum heat transfer rate allowed before flooding occurs can be calculated by:

$$Q_{max} = Kh_{fg}A[g\sigma(\rho_l - \rho_v)]^{1/4}\left[{\rho_v}^{-1/4} + {\rho_l}^{-1/4}\right]^{-2} \qquad (2.18)$$

where K can be expressed as

$$K = \left(\frac{\rho_l}{\rho_v}\right)^{0.14} tanh^2\, Bo^{1/4} \qquad (2.19)$$

and Bo is the Bond number defined as

$$Bo = \left(\frac{C_k}{C_w}\right)^4 \left[\frac{\sigma}{g(\rho_l - \rho_v)}\right]^{1/2} \qquad (2.20)$$

where $C_k = \sqrt{3.2}$ and $C_w = 1$.

2.4.4 Minimum fill requirement

As discussed above, the heat transfer limitations of a THP are dependent on the filling ratio of the working fluid. Faghri (1995) developed a simplified equation to determine the minimum fill requirement for a THP:

$$V_t = \left[\frac{4}{5}(L_e + L_c) + L_a\right]\left[\frac{3Q\mu_l(\pi D)^2}{{\rho_l}^2 g h_{fg}}\right]^{1/3} \tag{2.21}$$

2.5 Numerical modelling

This section describes the two most common turbulence models used to solve turbulent flows and heat transfer using Computational Fluid Dynamics (CFD), as well as the method for modelling THPs technologies using CFD.

2.5.1 Turbulence models

Most engineering flows are turbulent in nature, meaning the flow is characterized by chaotic changes or irregular movement of fluid within a specific flow region (Panchal, 2016). Laminar flow is characterised by regular, repeatable flow patterns.

The most economic approach for solving complex turbulent flows is the Reynolds Averaged Navier-Stokes (RANS) momentum equations. The different forms of the k-ε and k-ω models are examples of the RANS turbulence models. These models simplify the turbulence problem to two additional transport equations and introduce an Eddy viscosity to compute the Reynolds stresses (ANSYS, 2013b). This section will focus on the two most commonly used RANS turbulence models, namely the Realizable k-ε model and the Shear Stress Transport (SST) k-ω model.

The Realizable k-ε model was developed by Liou et al. (1995) and is different from the standard model in two ways (ANSYS, 2013a):

1. The turbulent viscosity is formulated alternatively.

2. The transport equation for the dissipation rate, ε, has been obtained from an exact transport equation of the mean-square vorticity fluctuation.

The term “realizable” implies that the model satisfies some of the mathematical constraints on the Reynolds stresses (ANSYS, 2013a). The transport equations for k and ε in the Realizable k-ε model can be expressed as follows.

$$\frac{\partial}{\partial t}(\rho k) + \frac{\partial}{\partial x_j}(\rho k u_j) = \frac{\partial}{\partial x_j}\left[\left(\mu + \frac{\mu_t}{\sigma_k}\right)\frac{\partial k}{\partial x_j}\right] + G_k + G_b - \rho\varepsilon - Y_m + S_k \tag{2.22}$$

and

$$\frac{\partial}{\partial t}(\rho\varepsilon) + \frac{\partial}{\partial x_j}(\rho\varepsilon u_j) = \frac{\partial}{\partial x_j}\left[\left(\mu + \frac{\mu_t}{\sigma_\varepsilon}\right)\frac{\partial \varepsilon}{\partial x_j}\right] + \rho C_1 S\varepsilon - \rho C_2 \frac{\varepsilon^2}{k + \sqrt{\nu\varepsilon}} + C_{1\varepsilon}\frac{\varepsilon}{k}C_{3\varepsilon} + S_\varepsilon \tag{2.23}$$

The SST k-ω model was developed by Menter (1994) and has a similar form to the standard model. The SST k-ω model includes the following refinements over the standard k-ω model (ANSYS, 2013a):

1. A damped cross diffusion derivative term is incorporated in the ω-equation of the k- ω SST model.

2. To consider the transport of the turbulent shear stress, the definition of the turbulent viscosity is altered.

3. The models have different modelling constants.

4. The transformed k-ε model and standard k-ω model are each multiplied by a blending function and joined together. In the near wall region the blending function is designed to be one, which activates the standard k-ω model. Whilst further away from the wall the blending function becomes zero, activating the transformed k-ε model.

The SST k-ω model can be presented with the following transport equations (ANSYS, 2013a).

$$\frac{\partial}{\partial t}(\rho k) + \frac{\partial}{\partial x_i}(\rho k u_i) = \frac{\partial}{\partial x_j}\left(\Gamma_k \frac{\partial k}{\partial x_j}\right) + G_k - Y_k + S_k \tag{2.24}$$

and

$$\frac{\partial}{\partial t}(\rho\omega) + \frac{\partial}{\partial x_j}(\rho\omega u_i) = \frac{\partial}{\partial x_j}\left(\Gamma_\omega \frac{\partial \omega}{\partial x_j}\right) + G_\omega - Y_\omega + D_\omega + S_\omega \tag{2.25}$$

2.5.2 Heat pipe modelling

This section explains the modelling of THPs as solid superconductors in an attempt to reduce the computational expense when used in numerical models. Chong et al., (2016) developed a solid superconductor model of a THP to accurately simulate a heat pipe based heat exchanger using CFD. The model utilized a thermal resistance diagram similar to the one illustrated in Figure 2.20 by Dobson and Meyer (2006). Figure 2.21 explains the thermal resistance diagram.

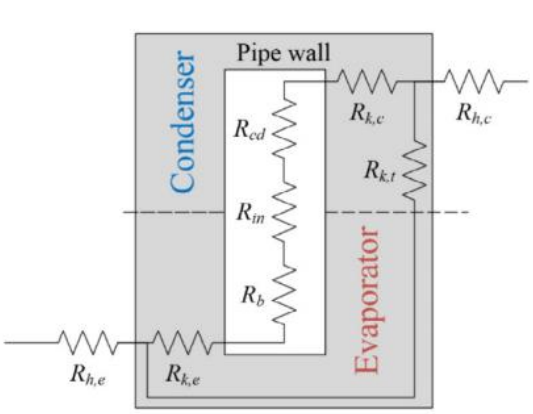

$R_{h,e}$	Thermal resistance from convection on outside of evaporator section
$R_{k,e}$	Thermal resistance from conduction across wall of evaporator section
R_b	Thermal resistance from boiling on TS wall
R_{in}	Thermal resistance from change in pressure between top and bottom
R_{cd}	Thermal resistance from condensation on TS wall
$R_{k,c}$	Thermal resistance from conduction across wall of condenser section
$R_{h,c}$	Thermal resistance from convection on outside of condenser section
$R_{k,t}$	Thermal resistance from Axial conduction across thermosyphon

Figure 2.21: Thermal resistance of thermosypon model developed by Chong et al. (2016)

According to Chong et al. (2016), the total thermal resistance of the THP can be calculated as follows:

$$R_t = R_{h,e} + R_{k,e} + R_b + R_{in} + R_{cd} + R_{k,c} + R_{h,c} \tag{2.26}$$

The thermal resistances for the conduction through the THP wall, $R_{k,e}$ and $R_{k,c}$ along with the thermal resistances for the convection on the outside of the THP wall, $R_{h,e}$ and $R_{h,c}$, was calculated as explained in section 2.4.3.

The thermal resistance from the vapour pressure drop, R_{in}, was that of Faghri, (1995) and can be expressed as:

$$R_{in} = \frac{8R_g\mu_v{T_v}^2}{\pi{h_{fg}}^2P_v\rho_v}\left(\frac{(L_e + L_c)/2 + L_a}{{r_i}^4}\right) \tag{2.27}$$

Where $R_g, h_{fg}, T_v, \mu_v, P_v$ and ρ_v are the specific gas constant, the latent heat of vaporisation and temperature, viscosity, pressure and density of the vapour phase respectively. The vapour temperature was taken as the average of the condenser and evaporator temperatures and the vapour pressure was the pressure at the vapour temperature.

The THPs were all designed to operate in the nucleate pool boiling regime, therefore the expression chosen for the pool boiling was that of Rohsenow (1952).

$$q'' = \mu_l h_{fg}\left(\frac{g(\rho_l - \rho_v)}{\sigma}\right)^{1/2}\left(\frac{c_{p,l}(T_{sat} - T_s)}{c_{sf}h_{fg}{Pr_l}^n}\right)^3 \tag{2.28}$$

The THPs in this study were made from carbon steel with water as the working fluid, therefore the values of c_{sf} and n are 0.006 and 1 respectively. The thermal resistance from boiling on the THP wall can therefore be expressed as:

$$R_b = \frac{T_s - T_{sat}}{q'' A_{ei}} \tag{2.29}$$

The heat transfer coefficient used to obtain the condensation was that of McAdams (1954) and can be expressed as

$$h_{cond} = 1.13 \times \left(\frac{{k_l}^3 {\rho_l}^2 g h_{fg}}{\mu_l \theta l} \right)^{1/4} \tag{2.30}$$

Equation 2.30 is then substituted into the equations for the thermal resistance of the inner condenser section described in section 2.4.2. It should be noted that equation 2.30 is very similar to equation 2.14 developed by Faghri (1995). Finally to calculate the thermal conductivity of the solid superconductor the following expression is used:

$$k_{THP} = \frac{L}{R_t A_c} \tag{2.31}$$

Where L is the length and A_c is the cross sectional area of the THP. It was found that this model slightly under predicted the results at higher evaporator temperatures and over predict the results at lower evaporator temperatures. However, it still produced accurate results with an average temperature difference of 5% in the evaporator side and 7% in the condenser side, between the experimental and numerical results.

3 Battery Thermal Management System Design

This chapter describes the design of a thermosyphon heat pipe (THP) Battery Thermal Management System (BTMS) for the reference Electric Vehicle (EV).

3.1 Problem description

The following section details the problem description of the current aluminium plate BTMS.

3.1.1 Heat transfer and temperature distribution

As mentioned in Section 1.1, the current BTMS consists of aluminium plates sandwiched between the Li-ion cells of the batteries. The plates conduct heat from the batteries and dissipate it into the cooling channel through forced convection. The airflow in the channel is as a result of an extraction fan at the outlet of the cooling channel.

As mentioned in Section 2.3 air cooling BTMSs are widely used in industry. These systems usually consist of a finned heat sink where the heat is removed via forced or free convection. However, in order for optimum heat transfer in these fins they have to be orientated perpendicular to the flow direction. This is not the case in the current battery pack. When air is forced over these aluminium fins, the flow separates from the first fins leaving a low pressure region behind the fin where recirculation and backflow occurs. At high flowrates other fins may be located in this low pressure region. This would impair the heat transfer from these fins, causing uneven cooling in the battery pack.

The parameters of the aluminium plates extending into the cooling channel currently used in the battery are shown in Figure 3.1, with the values of these parameters summarized in Table 3.1

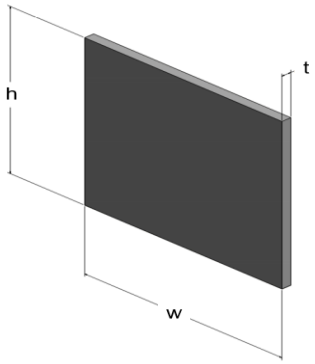

Figure 3.1: Parameters of the cooling duct and aluminium fins

Table 3.1: Parameter values of the aluminium fins

	Parameter	Value [mm]
Aluminium fins	h	42
	w	45
	t	2

3.1.2 Geometrical constraints

The compact layout of the battery pack meant there were two major geometrical constraints. The first being the 2 mm gap between the cells. The improved BTMS had to be compact enough to replace the aluminium plates between the cells without requiring a re-design of the battery pack layout.

The second geometrical constraint is the cooling channel. The cooling channel can be modelled as a rectangular duct, with the aluminium fins protruding into it. The location of the inlet of the cooling channel meant it would be hard to manipulate the airflow to cool down the cells directly. Thus the improved BTMS had to conduct the heat into the cooling channel. It also meant that the heat sink of the proposed improved BTMS was constrained to the dimensions of the cooling channel. The parameters of the cooling channel are shown in Figure 3.2, with the values of these parameters summarized in Table 3.2.

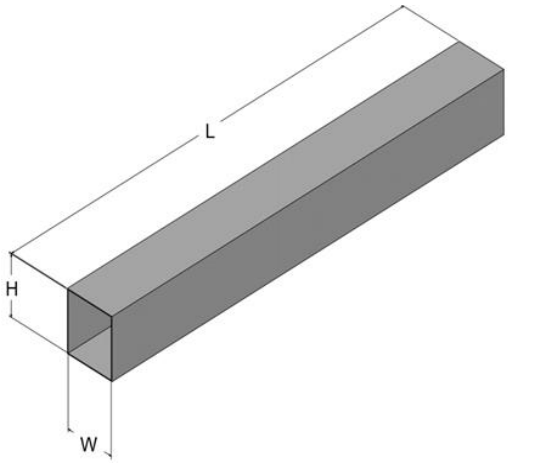

Figure 3.2: Parameters of the cooling channel

Table 3.2: Parameter values of the cooling channel

	Parameter	Value [mm]
Cooling channel	H	128
	W	110
	L	1000

3.2 BTMS enhancement

This section describes the design and parameters of the improved BTMS.

3.2.1 Improved BTMS design

To ensure that the footprint for the battery pack is kept the same, it was decided to develop a BTMS that could replace the aluminium fins without requiring the battery pack to be redesigned. As mentioned in Section 2.3.4, heat pipe based technologies have recently been receiving significant attention for use in battery cooling systems. Therefore it was decided to develop a THP BTMS, since they are very compact and excellent conductors. It was decided to use THPs instead of normal heat pipes, since it would be costly and difficult to manufacture a regular heat pipe with a wick structure capable of fitting in the 2 mm gap left by the aluminium plates.

The heat sink attached to the condenser section was also constrained by the geometry of the cooling channel. The fins needed to be sufficiently compact in order to allow the addition of a sufficient number of fins for optimum heat transfer, as well as sufficiently porous in order to ensure minimal pressure loss in the channel. It was determined iteratively that eight fins with a fin spacing of 5 mm would deliver the best performance.

The THPs were manufactured by Cape Heat Exchange (Pty) Ltd in Paarl, South Africa. The THPs were made from 6 mm copper tubes flattened to a thickness of 2 mm, in order to fit between the Li-ion cells. The heat sink was created by brazing the eight 0.5 mm thick copper fins to the condenser section of the THPs. Schrader valves were soldered to the endcaps of the evaporator section to enable the THPs to be filled with working fluid and pressurized. To pressurize the THPs, they were heated to ±60 °C and “bled” at atmospheric pressure, in order to create a vacuum inside. This was done to decrease the temperature at which the working fluid inside evaporates, thereby improving the efficiency of the THPs at lower temperatures.

3.2.2 Heat transfer enhancements

To improve the heat transfer of the BTMS, two major characteristics of the current BTMS were adjusted.

The first characteristic was the ability of the system to conduct heat from the batteries to the cooling channel. Therefore, by replacing the aluminium plates with copper THPs, the conductive heat transfer was improved. To optimise this conduction it was decided to use methanol as the working fluid. This would enable the THP to function better at lower temperatures, since methanol has a high latent heat of vaporization in comparison to other working fluids.

The second was the ability of the system to dissipate heat via forced convection. This was achieved by increasing the effective heat transfer area as a result of brazing eight copper fins to the condenser section. Since these fins were orientated parallel to the flow, the airflow over these fins should improve. This should result in a more uniform heat transfer rate throughout the battery pack, thereby improving the temperature uniformity of the cells. The final parameters of the THP and fins can be seen in Figures 3.3 and 3.4, with the parameter values summarised in Table 3.3.

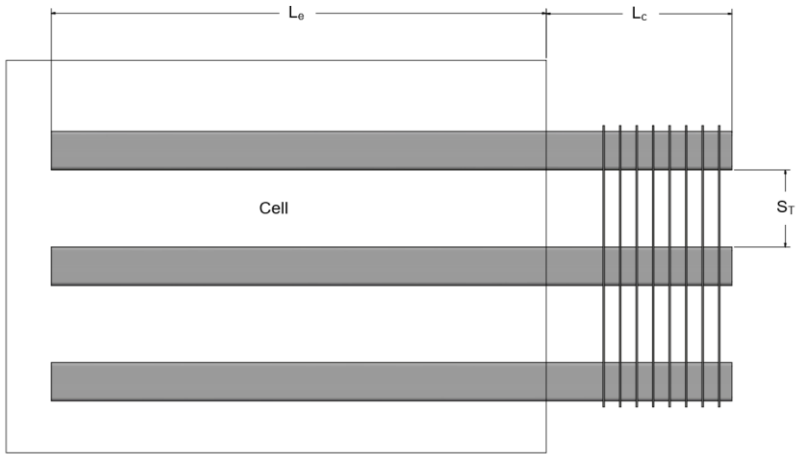

Figure 3.3: Frontal view of the THP parameters

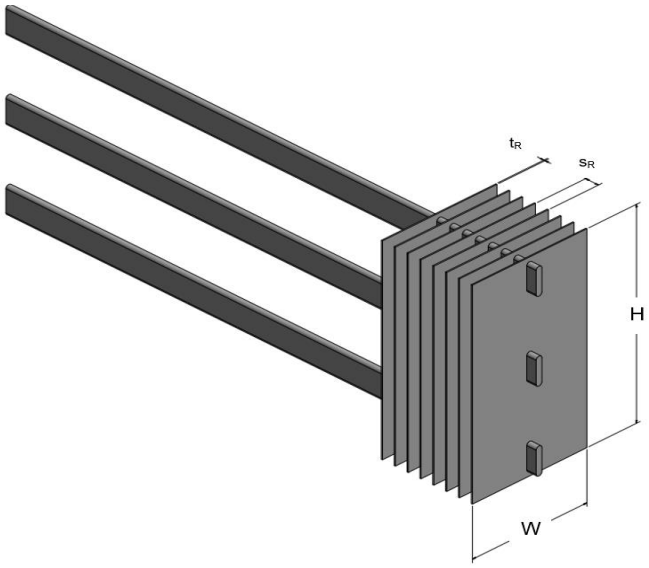

Figure 3.4: Isometric view of the THP parameters

Table 3.3: Parameter values of the THPs

	Parameter	Value [mm]
THP	H	96
	W	49
	s_R	5,5
	t_R	0,5
	L_e	175
	L_c	53
	S_T	38
	S_L	49
	a	2
	b	11
	Wall thickness	0,6

3.2.3 Battery pack changes

In order to install the new THP BTMS into the existing battery pack, new callipers had to be used to connect the cells to one another. These new callipers were supplied along with the cells from Liyuan Battery Company Ltd. They are composed of plastic and can be tightened together via four 6 mm threaded rods that slide through the four holes in the corners. When tightened there is a 2 mm gap between each cell where the THPs fit in. The THPs are orientated such that

the evaporator section is slightly lower than the condenser section, to allow the condensed working fluid to return to the evaporator. The orientation of the THPs and the callipers are illustrated in Figure 3.5 and Figure 3.6 respectively.

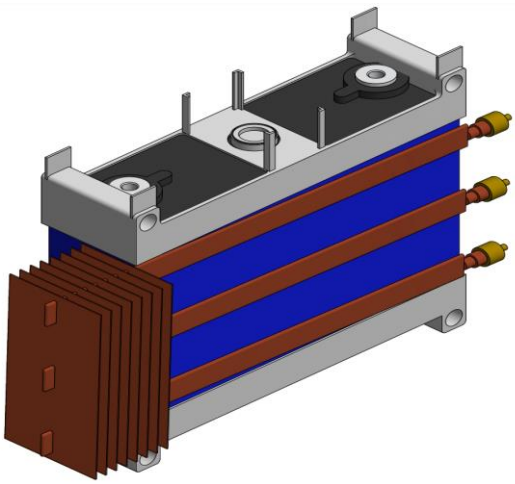

Figure 3.5: Illustration of the orientation of the THP BTMS

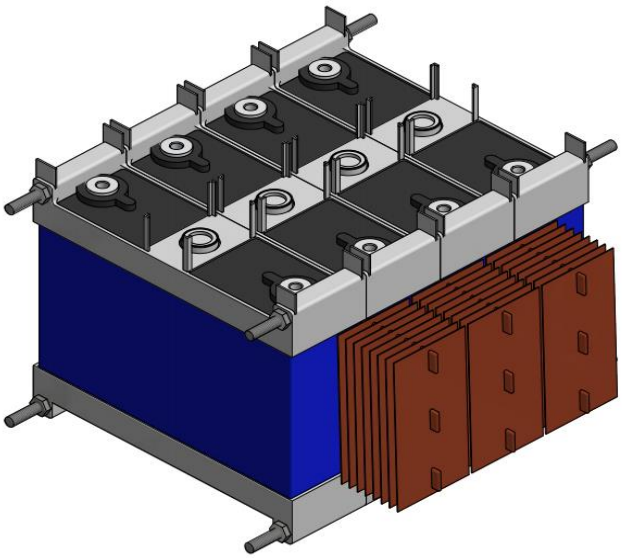

Figure 3.6: Illustration of new calliper design

4 Heat Transfer Analysis

This chapter presents the methods used to determine the air side heat transfer coefficient, temperature distribution, pressure drop and heat transfer rate of the different battery thermal management systems. The performance of these systems were compared by calculating the heat generated by the Lithium-ion (Li-ion) cells and comparing it to the heat dissipated to the surroundings through forced convection.

4.1 Heat Generation of Li-ion Batteries

According to Karimi and Li (2013) heat in a cell is generated by (i) Entropy change as a result of electrochemical reactions and (ii) Joule's effect, also referred to as ohmic heating. The heat generation rate in a cell can be calculated from (Chen and Evans, 1994):

$$Q = I(V_{oc} - V) - IT\frac{dV_{oc}}{dT} \tag{4.1}$$

Where Q is the heat generation rate, I is the current, V_{oc} is the open circuit voltage, V is the cell voltage, T is the temperature and $\frac{dV_{oc}}{dT}$ is the temperature coefficient. The first term, $I(V_{oc} - V)$, refers to the heat generated from internal resistances present in the cell and the second term, $-IT\frac{dV_{oc}}{dT}$, refers to the heat generated due to irreversible entropy change as a result of the cell's electrochemical reactions. The internal resistances and entropy changes differs for different kinds of Li-ion cells. The internal resistances are dependant on the State of Charge (SOC) and the temperature of the cells and is, to the knowledge of the author, unavailable in open literature. However an expression of the internal resistance of small size Li-ion batteries, SONY-US18650, has been determined by Inui et al. (2007). This experimental data was curve fitted for numerical implementations as follows:

$$R_i = \begin{cases} 2.258 \times 10^{-6} SOC^{-0.3952} & T = 20\ °C \\ 1.857 \times 10^{-6} SOC^{-0.2787} & T = 30\ °C \\ 1.659 \times 10^{-6} SOC^{-0.1692} & T = 40\ °C \end{cases} \tag{4.2}$$

where R_i is the equivalent internal resistance of unit volume in ($\Omega\ m^3$). Panchal (2016) suggested using an adaptation of Ohm's law to calculate the internal resistance, where the voltage drop is divided by the current as illustrated below:

$$R_{V_{oc}} = \frac{V_{OC} - V_{act}}{I} \tag{4.3}$$

In addition the change in entropy, ΔS, is determined by measuring the dependence of the open circuit voltage of the cell on the temperature of the cell at various SOC's. The change in entropy is defined as (Inui et al., 2007):

$$\Delta S = F\frac{dV_{oc}}{dT} \tag{4.4}$$

Where F is defined as the Faraday number (96485 °C mol^{-1}). According to Karimi and Li (2013) their experiments indicated that for a temperature range, ranging from 20 °C to 40 °C, ΔS is almost independent of the temperature and can therefore be calculated as a function of SOC using the following equations:

$$\Delta S = \begin{cases} 99.88\,SOC - 76.67 & 0 \leq SOC \leq 0.77 \\ -30 & 0.77 \leq SOC \leq 0.87 \\ -20 & 0.87 \leq SOC \leq 1 \end{cases} \tag{4.5}$$

Considering the equations above, the heat generation rate equation can be rewritten as:

$$q = R_i i^2 - iT\frac{\Delta S}{F} \tag{4.6}$$

Where q represents the rate of heat generation per unit volume and i represents the discharge current of a Li-ion cell per unit volume.

4.2 Analytical Solution of Cooling Plate BTMS

This section describes the analytical solution of the convective heat transfer coefficient, temperature distribution and pressure drop of the original aluminium plate BTMS.

4.2.1 Convective Heat Transfer Coefficient

To calculate the convective heat transfer coefficient, the flow through the rectangular cooling channel is treated as an internal flow configuration, and the flow over the fins as external forced convection. Wang et al. (2012) investigated the flow and heat transfer characteristics of pin fin arrays in a rectangular channel. Due to the similarities between the two geometries the same procedure is used for the heat transfer analysis of the cooling plate BTMS. The hydraulic diameter of the rectangular duct with a fin array is calculated as the ratio of the open duct volume available for the fluid flow divided by the total wetted surface area of the aluminium fin array region. This ratio is the most suitable characteristic length due to the fact that it captures all the length scales in the problem (Wang et al., 2012).

$$D_h = \frac{4V_f}{A_w} \tag{4.7}$$

where V_f is the total fluid volume inside rectangular duct and A_w the wetted surface area, also defined as the total heat transfer area in contact with the fluid. For a rectangular duct with a width W, height H, lenth L containing N number of fins with cross section area A_f and perimeter p_f, the fluid volume and wetted surface area can be calculated as follows:

$$V_f = L\,W\,H - N\,A_f\,l \tag{4.8}$$

$$A_w = 2\,L\,(W + H) + N\,(p_f\,l - 2\,A_f) \tag{4.9}$$

The Reynolds number is calculated with the hydraulic diameter and defined by:

$$Re_{Dh} = \frac{v_{max}\,D_h}{\nu} \tag{4.10}$$

where v_{max} is the maximum velocity of the fluid in the channel and ν the kinematic viscosity of the cooling fluid. The average Nusselt number is used to determine the convective heat transfer coefficient and is formulated as:

$$Nu = \frac{h_{conv}\,L_c}{k} \tag{4.11}$$

where L_c is the characteristic length of the fin and k the thermal conductivity of the fluid. The average Nusselt numbers for Reynolds numbers ranging from 6300 to 79000 for flow over a vertical plate is presented by Cengel and Ghajar (2015). The average Nusselt number can be expressed as follows:

$$\begin{aligned} Nu &= 0.257\,Re^{0.731}\,Pr^{1/3} \quad 6300 \le Re \le 23600 \\ Nu &= 0.094\,Re^{0.675}Pr^{1/3} \quad 23600 \le Re \le 79000 \end{aligned} \tag{4.12}$$

Substituting this average Nusselt number into equation 4.11 yields the convective heat transfer coefficient.

4.2.2 Fin Temperature Distribution

According to Cengel and Ghajar (2015) the temperature along a fin drops from the base to the tip. For this analysis it is assumed that there is convective heat transfer from the fin tip to the surroundings, therefor allowing the fin temperature distribution $T(x)$ to be expressed as follows:

$$\frac{T(x) - T_\infty}{T_b - T_\infty} = \frac{\cosh m(L - x) + \left(\frac{h_{conv}}{m \cdot k}\right)\sinh m \cdot (L - x)}{\cosh mL + \left(\frac{h_{conv}}{mk}\right)\sinh m \cdot L} \tag{4.13}$$

where,

$$m = \sqrt{\frac{h_{conv}\, p_f}{k\, A_f}} \tag{4.14}$$

4.2.3 Pressure Drop

The total pressure drop of the aluminium cooling plate BTMS is calculated as; the sum of the pressure drop caused by the drag over the fins and the pressure drop due to the length of the cooling channel. Kröger (1998) defined the pressure drop over a plate perpendicular to the flow as:

$$\Delta P = N C_D \left(\frac{\rho\, v^2}{2} \right) \tag{4.15}$$

The drag coefficient C_D for a flat plate, perpendicular to the flow, was determined by Kröger (1998) to be 1.96. The number of tubes are presented by N, and v refers to the velocity flowing over the fins. Cengel and Ghajar (2015) stated that the pressure drop caused by the flow through a duct can be calculated with the following expression:

$$\Delta P = 4f \frac{L}{D_h} \frac{\rho v^2}{2} \tag{4.16}$$

where f is the Darcy friction factor read off from the moody chart in Figure A.12 of Cengel and Cimbala (2014).

4.3 Analytical solution of the THP BTMS

This section describes the analytical solution for the convective air side heat transfer coefficient of the finned evaporator section, the temperature distribution and pressure drop of the improved THP BTMs.

4.3.1 Convective Heat Transfer Coefficient

Due to the geometric similarities, the finned heat pipes are modelled as finned tube bundles with continuous smooth fins. Numerous literature sources describing the theoretical modelling of finned tube bundles exist, however for this analysis the methods and equations of Frass (2015) and Kröger (1998) were used and compared. These methods are explained below.

Frass (2015)

In this model a tube fin bundle with continuous smooth fins and non-circular tubes is modelled. For this analysis the calculation equations rely on a characteristic

length which is defined as the hydraulic diameter of a single flow channel or control volume, as seen in Figure 4.4.

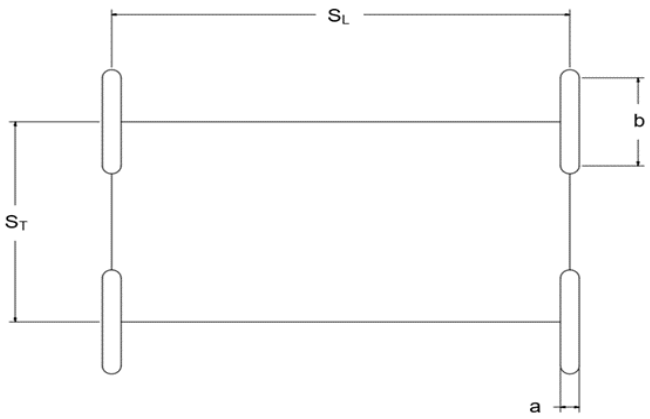

Figure 4.1: THP condenser section control volume

This hydraulic diameter is obtained using $D_h = 4\,V/A$:

$$D_h = \frac{4\left[(s_R - t_R)\left(S_T\,S_L - \left(a(b-a)\right) - a^2\frac{\pi}{4}\right)\right]}{A_{Ftot}} \tag{4.17}$$

The individual terms in this equation are: the fin thickness t_R, the fin pitch s_R, the transverse and longitudinal pitch S_T and S_L and a and b representing the small and large axis of the heat pipe. The effective heating surface A_{Ftot} is formulated as:

$$A_{Ftot} = 2\left[S_T S_L - a(b-a) - \frac{\pi a^2}{4}\right] + [2(b-a) + a\pi](s_R - t_R) \tag{4.18}$$

The dimensionless Nusselt number for heat transfer in an in-line tube arrangement is given by Gross and Kaminski (2000) as:

$$Nu = 0.0842\,{Re_{Dh}}^{0.7}\,Pr^{1/3}\left(\frac{D_h}{S_L}\right)^{1/3} \tag{4.19}$$

This representation of the Nusselt number given above is, however, a simplification and therefore only valid for Reynolds numbers ranging from 1000 to 10000. This corresponds roughly to air at ambient temperatures with a velocity of 3 m/s to 30 m/s. According to Kays and Londen (1984), the Reynolds number in this case is determined using D_h, but with the velocity in the narrowest cross section v_{ncs}, defined as:

$$v_{ncs} = \frac{v_0}{A_f} \tag{4.20}$$

where A_f is the free cross sectioned area formulated by:

$$A_f = \left(\frac{S_T - a}{S_T}\right)\left(\frac{s_R - t_R}{s_R}\right) \tag{4.21}$$

The convective heat transfer coefficient is then calculated with Equation 4.11. However, there are a number of ways to calculate the characteristic length L_c. According to the calculation method of Schmidt (1963), Skrinska and Stasiulevicius (1988) the diameter of the core tube d_o can be used for L_c. Several other expressions include the equation by Mirkovics (1974):

$$L_c = \frac{2A_{tot}}{\pi \frac{2h + s_R}{s_R}} \tag{4.22}$$

and Brandt (1985):

$$L_c = \frac{\pi}{2}\sqrt{{d_o}^2 + h^2} \tag{4.23}$$

Kröger (1998)

For this model a small control volume, similar to the control volume used by Frass (2015) is considered. The volume is situated between the centrelines of two adjacent tubes and fins. The tubes have flattened sides with semi-circular ends. Therefor the minimum free flow area through the control volume is:

$$A_{cvc} = (S_T - b)(s_R - t_R) \tag{4.24}$$

The corresponding frontal area is:

$$A_{cvfr} = t_R s_R \tag{4.25}$$

Using these values the area ration can be defined as:

$$\sigma_a = \frac{A_{cvc}}{A_{cvfr}} \tag{4.26}$$

The fin surface exposed to the air stream may be expressed as:

$$A_{cvc} = 2\left[t_R s_R - a(b - a) - \frac{\pi a^2}{4}\right] \tag{4.27}$$

and the total area in contact with the air stream flowing through the control volume:

$$A_{cva} = A_{cvc} + (s_R - t_R)[2(b - a) + \pi a] \tag{4.28}$$

From the equations above the hydraulic diameter D_h can be expressed as:

$$D_h = \frac{4A_{cvc}S_L}{A_{cva}} \tag{4.29}$$

The air mass velocity flowing through the minimum free flow area of the control volume can be expressed as:

$$G_{acv} = \frac{m_a}{A_{fr}\sigma_a} \tag{4.30}$$

The corresponding Reynolds number may be defined as:

$$Re = \frac{G_{acv}D_h}{\mu} \tag{4.31}$$

Using this Reynolds number the Colburn j-factor is read from Figure 5.4.1 in Kröger (1998). Kays and Londen, (1984) expressed the dimensionless form of the Colburn j-factor, originally proposed by Colburn (1933) as:

$$j = StPr^{0.67} = \frac{NuPr^{0.67}}{Re\ Pr} = \frac{h_{conv}Pr^{0.67}}{G_{acv}c_p} \tag{4.32}$$

The convective heat transfer coefficient is then determined by computing all of the above values and substituting them into equation 4.32.

4.3.2 Temperature Distribution in the THP

To calculate the temperature distribution throughout the THP, it was sectioned into smaller control volumes, as shown in Figure 4.2.

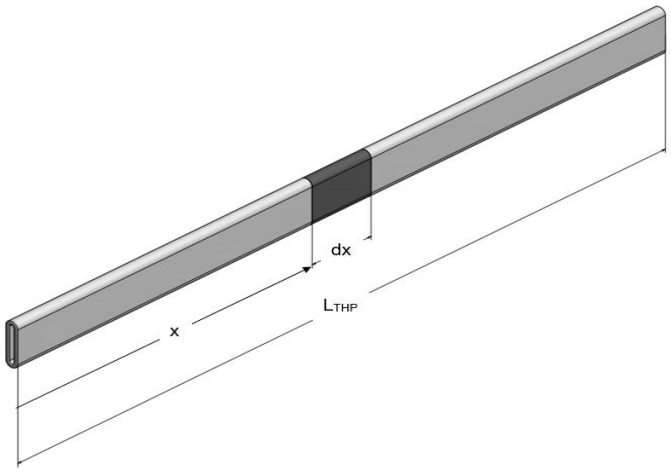

Figure 4.2: Isometric view used to define the control volume along the length of the THP

According to Faghri (1995) a constant vapour temperature can be assumed throughout the THP, which is equal to the saturation temperature. This saturation temperature is calculated using:

$$T_{sat} = \frac{T_{w,e}L_e + T_{w,c}L_c}{L_e + L_c} \tag{4.33}$$

Strel'tsov (1975) derived a simplified analysis where the assumption was made that the minimum fill volume is only that which required the walls of the THP to be covered in the liquid film, thereby eliminating the liquid pool from the analysis. The film thickness is then given as:

$$\delta = \left(\frac{\pi k \mu_l (T_{sat} - T_w) z}{{\rho_l}^2 g h_{fg}}\right)^{1/4} \tag{4.34}$$

where z can be substituted with the evaporator, condenser and adiabatic lengths, to calculate the thickness of the liquid film in each region. The mass flow rate of the liquid film inside the THP can then be determined with the following formula:

$$\dot{m} = \frac{\pi {\rho_l}^2 D g \delta^3}{3\mu_l} \tag{4.35}$$

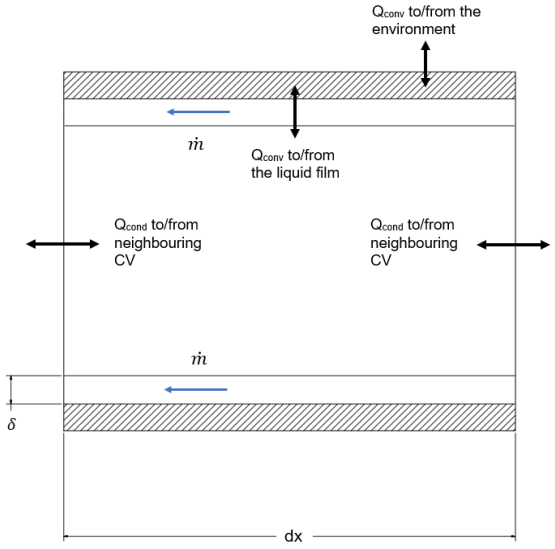

Figure 4.3: Control volume boundary conditions

Figure 4.3 illustrates the control volume of the THP wall and all of the boundary conditions. To determine the temperature at the wall node for each control volume, an energy balance was done for each control volume. A finite difference approach is then used to calculate the temperature at each wall node. The node temperatures in the condenser section are then used as the base temperatures in Equation 4.13 to calculate the temperature distribution in the fins attached to the THP. The relevant equations for the energy balance and matrices used to solve the temperature distribution can be found in Appendix C.

4.3.3 Pressure Drop

To calculate the pressure drop as a result of the flow over a flat tube bundle with continuous fins, Frass (2015) used expressions for the pressure drop coefficient and pressure drop expressed by Gross and Kaminski (2000) as:

$$\xi = 0.7\, {Re_{Dh}}^{-0.339} \left(\frac{D_h}{S_L}\right)^{0.6} \tag{4.36}$$

and

$$\Delta P = N\xi\rho \frac{{v_{ncs}}^2}{2} \tag{4.37}$$

According to Kröger (1998), the pressure drop may be expressed as:

$$\Delta P = \frac{{G_{acv}}^2}{2}\left[\frac{4Nf}{\rho_m}\left(\frac{A_{cva}}{A_{cvc}}\right) + (1+{\sigma_a}^2)\left(\frac{1}{\rho_o}-\frac{1}{\rho_i}\right)\right] \tag{4.38}$$

where N represents the number of tube rows and ρ_m, ρ_o and ρ_i the mean air, outlet and inlet density of the fluid as it flows through the core. The friction factor f is read off from Figure 5.4.1 in Kröger (1998).

5 Numerical Solution

The following section describes the Computational Fluid Dynamics (CFD) study conducted using ANSYS® Fluent Version 19.1.

5.1 Aluminium plate BTMS

5.1.1 Computational domain

Figure 5.1 shows the three dimensional geometry of the aluminium cooling plate BTMS that was modelled for this thesis. The geometry was created using Autodesk© Inventor Professional 2018 and then imported into ANSYS® Fluent's Design Modeller. The aluminium plates extending into the cooling channel were modelled as solid components inside of the fluid domain.

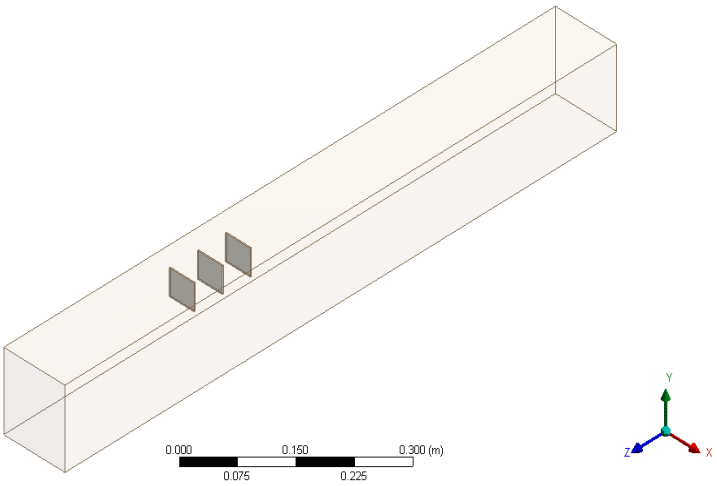

Figure 5.1: The isometric view of the geometry

The dimensions of the computational domain corresponds to the dimensions of the analytical solution and experimental setup of the aluminium cooling plate BTMS. This was done in order to validate the solution with the experimental results. The dimensions of the computational domain are presented in Chapter 3.

5.1.2 Computational mesh

The fluid zone in this simulation is meshed using an unstructured mesh in order to enable automatic mesh refinement at a later stage. It makes use of edge and face sizing, as well as inflation layers. The edge and surface sizings allow for refinement of the mesh, enabling a high degree of control as to where the mesh needs to be finer or can afford to be coarser. The use of inflation layers on the surfaces of the aluminium fins allow for accurate mesh sizing in order to accommodate the use of turbulence wall functions employed in the different turbulence models. Figure 5.2

shows the side view of the final refined mesh where the inflation layers and differences in mesh sizing for different regions is apparent. A closer view of the inflation layers around the aluminium fins can be seen in Figure 5.3.

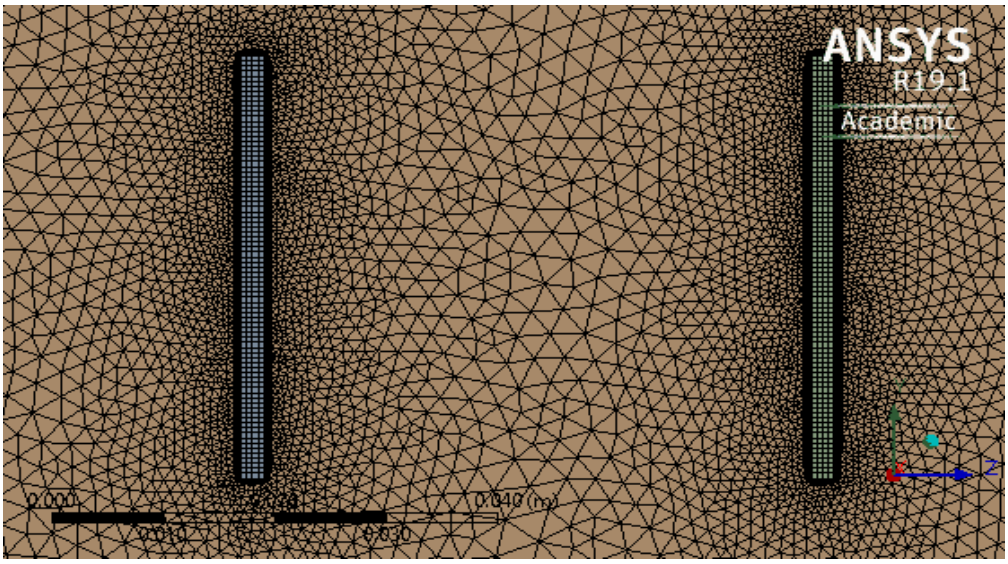

Figure 5.2: Side view of computational mesh

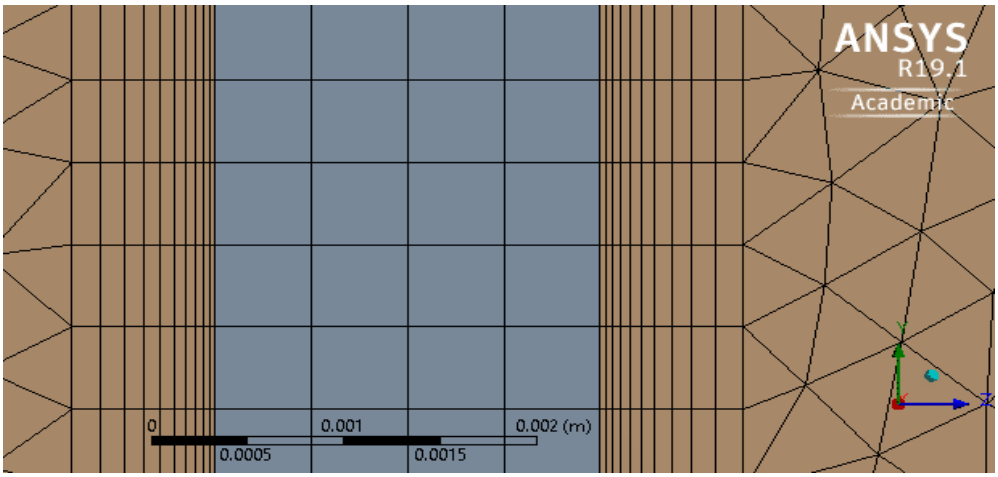

Figure 5.3: Close up view of the inflation layers

The meshing strategy followed for this simulation was employed over a number of mesh iterations. Initially a coarse mesh was created to confirm a functioning model. A grid independence study was carried out to identify changes in the results of the solution upon refinement of the mesh. It was conducted based on the area weighted average of the first aluminium fin's wall temperature, surface heat transfer coefficient and heat flux. For this study the bases of the fins were given a constant temperature of 26 °C, whilst the inlet air was given a temperature of 18

°C. The results of the study, as well as the mesh particulars, can be seen in Table 5.1. It was decided to use the fine mesh to perform the final simulations.

Table 5.1: Particulars of the grid independence study of the aluminium fin simulations

	Mesh			% diff. Coarse to Medium	% diff. Medium to Fine
	Coarse	**Medium**	**Fine**		
Cells	2912527	4460261	6834616	41,98504	42,043043
Faces	5942441	9663500	16703868	47,68772	53,402129
Nodes	555152	1332261	3638754	82,34647	92,797668
$Q_{1,wall}$ [W]	1,92518	1,88724	1,89552	1,990599	0,4378816
$T_{s,ave}$ [°C]	24,4955	24,4927	24,4931	0,011676	0,0017148
h_1 [W/m²·K]	64,0142	62,7819	62,30435	1,943782	0,7635372

During the refinement of the mesh, a basic version of the simulation was run until relative convergence was achieved and then a contour plot of the y^+ values was generated. The process was repeated in order to adjust the inflation layers and the individual edge and face sizings to ensure that the y^+ values were in the desired range (~1) required for the k-ω turbulence model. Figure 5.4 illustrates the y^+ values of the initial coarse mesh (left) and the refined mesh (right). Note that the variation of the y^+ values are less for the refined mesh.

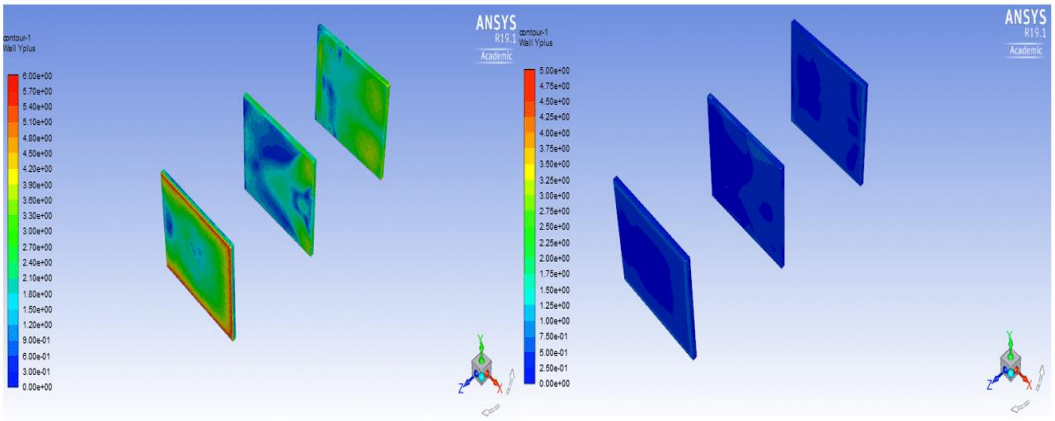

Figure 5.4: Comparison of the plate wall y^+ values

The final mesh refinement yielded a mesh with an element sizing of 0.01 m on all edges and faces of the cooling channel and a 0.0005 element sizing on the edges of the aluminium fins. The universal growth rate of the mesh was set to 1.1, and the inflation layers used smooth transition with a maximum of 10 layers and a growth rate of 1.2. Finally in an effort to further improve the quality of the mesh and reduce the overall cell count, the mesh was converted to a polyhedral mesh. A

comparison between the refined tetrahedral and polyhedral meshes can be seen in Table 5.2.

Table 5.2: Comparison of polyhedral and tetrahedral mesh particulars for the aluminium fin simulations

	Mesh	
	Tetrahedral	**Polyhedral**
Cells	6834616	5489389
Faces	16703868	21058396
Nodes	3638754	10753577
Minimum orthogonal quality	0,0987433	0,108967

From Table 5.2 it is clear that the conversion reduced the cell count while also improving the minimum orthogonal quality. According to ANSYS (2013b) the minimum orthogonal quality should not be less than 0.01.

5.1.3 Boundary conditions

The geometry was split into several named sections during the meshing phase. These are the “Channel Wall” sections, “Inlet”, “Outlet”, “Fin Walls” and “Fin Source”. Figure 5.5 and 5.6 shows the different boundary conditions.

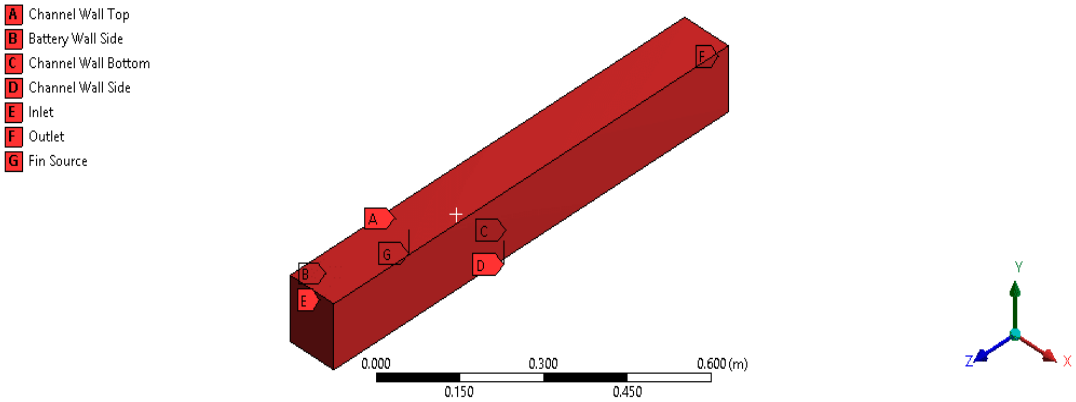

Figure 5.5: Named sections for outer boundary conditions

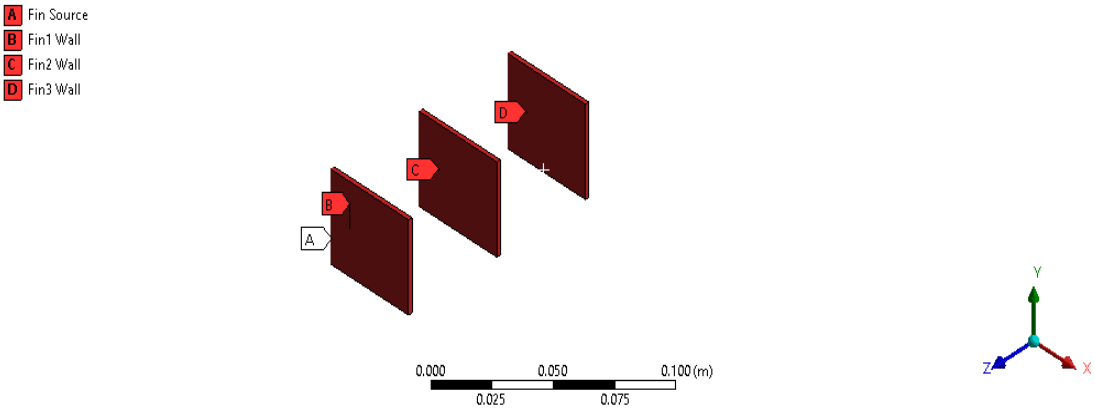

Figure 5.6: Named sections for fin boundary conditions

The “Channel Wall” sections were classified as stationary adiabatic wall boundaries with a no slip boundary condition. The walls were assumed to be perfectly smooth.

The “Fin Wall” sections located inside the fluid domain were allocated a “Coupled” boundary condition. This is the default interfacial boundary condition between a fluid zone and solid zone. To ensure that each side of the wall is a distinct wall zone the software automatically creates a “shadow” of the zone. No additional thermal boundary conditions are required as the solver calculates the heat transfer directly from the solution of the adjacent cell (ANSYS, 2013b).

The “Fin Inlet” sections were given a constant temperature boundary condition, since the temperature of the aluminium plate between the cells will have the same temperature as the cells. This temperature was specified as 27.25 °C.

The “Inlet” surface is located where the ambient air will enter the cooling channel. It was specified as a pressure-inlet and it was assumed that the air is at atmospheric pressure. Therefore the total gauge pressure was set to 0 Pa. The “Turbulence Specification Method” was set to “Intensity” and “Hydraulic diameter”. At the core of a fully developed duct flow, the turbulence intensity, I, can be calculated as follows (ANSYS, 2013b):

$$I = 0.16(Re_{Dh})^{-1/8} \tag{5.1}$$

Using this equation, the turbulent intensity was calculated to be 4.1 %.

The “Outlet” plane at the end of the cooling channel is where the air exits the geometry through the extraction fan. To model the effect of the fan accurately the plane was modelled as a mass flow outlet. The mass flow rate was determined from the operating point on the fan curve, shown in Appendix B. To plot the fan curve, the pressure had to be converted to static pressure. The “static pressure”

referred to by the fan supplier is in reality the fan total-to-static pressure. To calculate the static-to-static pressure of the fan, the dynamic pressure was added to the total-to-static pressure (Van der Spuy and Von Backström, 2009). The mass flow rate was then determined to be 0.1009 kg/s.

5.1.4 Control parameters

This section describes the control parameters used for this simulation.

A “Pressure-Based” solver was used, and the simulation was treated as steady state simulation. For this simulation gravity was enabled and assumed to be -9.81 m/s^2 in the y-direction. The energy equation was enabled in order to calculate the heat transfer.

It was decided to use the Shear Stress Transport (SST) k-ω rather than the k-ε viscous model, since k-ω models are typically better at predicting separation and adverse pressure gradient boundary layer flows. The SST model differs from the standard model as it includes a modified turbulent viscosity equation (Panchal, 2016). All k-ω models use enhanced wall treatment as default.

The properties of the fluid (air) and solids (aluminium) are shown in Appendix B. The air properties were taken at 25 °C, the same as the ambient temperature measured during the experiments, whilst the aluminium was modelled as aluminium 5754.

The pressure velocity coupling was set to “Coupled”, as it provides a more robust solution for steady state single phase flows (ANSYS, 2013b). The gradient for the spatial discretization scheme was set to “Least Squares Cell Base”, as the inflation layer mesh is structured therefore it will yield better results than a node based scheme. The pressure spatial discretization scheme was set to “PRESTO!” as it is well suited for the steep pressure gradients associated with swirling flows. For accuracy the spatial discretization schemes for the momentum, energy, turbulent kinetic energy and specific dissipation rate were set to “Second Order Upwind”.

The residuals were set at 1e-6 for the energy equation and 1e-3 for the velocity, k and omega equations. The hybrid initialization method was used to initialize the simulation. It solves the Laplace equation to calculate the pressure and velocity fields. All other variables are automatically patched based on domain averaged values (ANSYS, 2013b).

The convergence levels are shown in Appendix G, it can be seen that the solution converged after approximately 150 iterations. Report definitions of the fin temperature, inlet velocity and outlet velocity were also created to monitor the convergence of the simulation. These figures are shown in Appendix G.

5.2 Thermosyphon heat pipe BTMS

5.2.1 Computational domain

The computational domain for the numerical analysis of the Thermosyphon Heat Pipe (THP) BTMS can be seen in Figure 5.7. Like the previous geometry, the geometry was created using Autodesk© Inventor Professional 2018, and imported into ANSYS Fluent's Design Modeller.

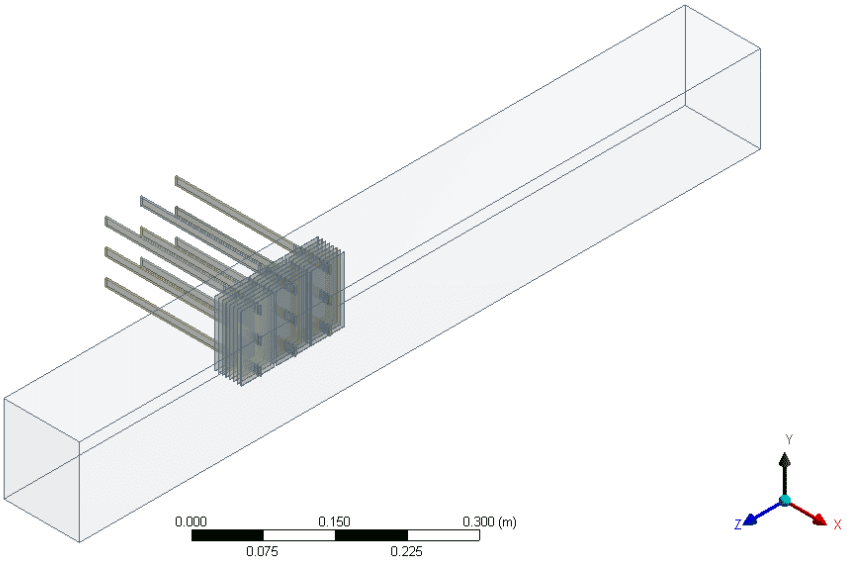

Figure 5.7: Isometric view of THP geometry

As with the previous geometry the THPs were modelled as solids within the fluid domain. The dimensions of the channel corresponds to that of the first simulation.

5.2.2 Computational mesh

The meshing strategy for this simulation involved creating an initial coarse mesh, and refining it until the y^+ values met the requirements of the specified turbulence model. The geometry was split into sections to enable a greater degree of control when refining the mesh. The different sections also made it easier to generate a coarser mesh at areas of less interest. A detailed view of the different sections can be seen in Figure 5.8.

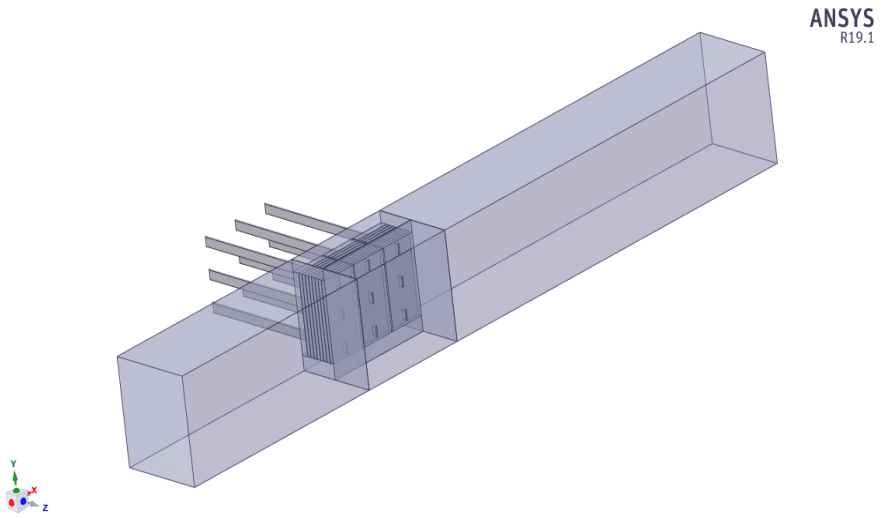

Figure 5.8: Illustration of the different sections of the geometry

During the mesh refinement a grid independence study was carried out to view the effects of the mesh size on the results of the simulation. As with the first simulation, the grid independence study conducted was based on the area weighted average of the temperature and heat transfer coefficient of the end fin on the first THP as well as the heat flux from the first set of THPs. For this study the evaporator sections of the THPs were given a constant temperature of 26 °C, whilst the inlet air was modelled at 18 °C. The results of the study, as well as the mesh particulars, can be seen in Table 5.3.

Table 5.3: Particulars of the grid independence study of the THP simulations

	Mesh			% diff. Coarse to medium	% diff. Medium to fine
	Coarse	**Medium**	**Fine**		
Cells	2161067	5214937	17373485	82,8055	107,653
Faces	5586935	13375352	47516849	82,1464	112,138
Nodes	1428597	3326449	13613694	79,8248	121,454
Q_{THP} [W]	3,32537	3,874579	4,632694	15,2559	17,8227
Ts,ave [°C]	22,9424	22,64493	22,74534	1,30525	0,44243
$h_{1,THP}$ [W/m2·K]	23,5199	27,44846	27,24292	15,4159	0,75163

The fine mesh was used to perform the final simulations, since its y^+ values met the requirements of the k-ω turbulence model the best, as illustrated in Figure 5.9 below.

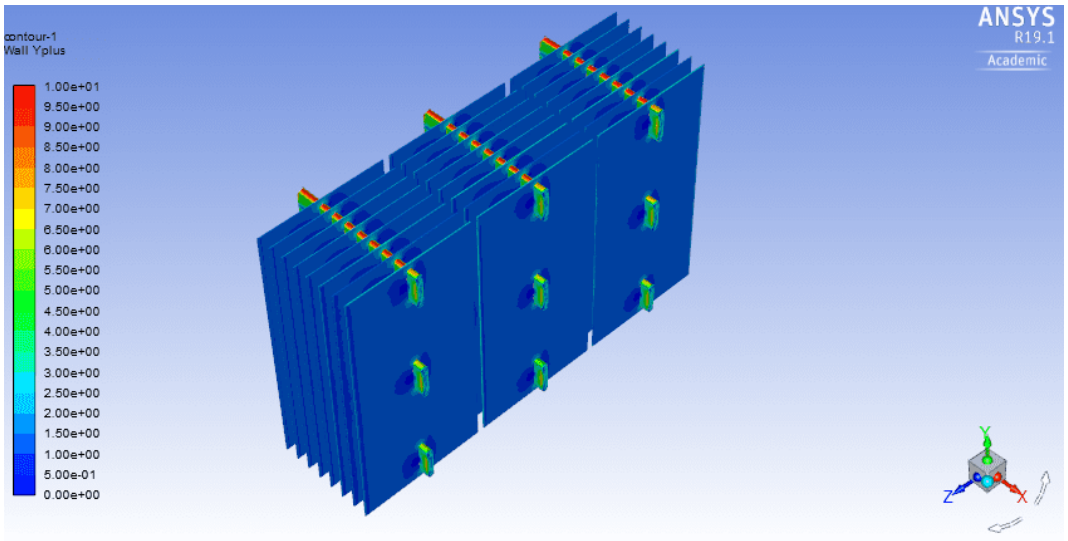

Figure 5.9: Wall y+ values for the THP simulation

The final tetrahedral mesh can be seen in Figure 5.10 and 5.11. In Figure 5.10 one can see the tetrahedral mesh sections surrounding the THP section, whereas Figure 5.11 illustrates the hexahedral mesh layers between the fin surfaces.

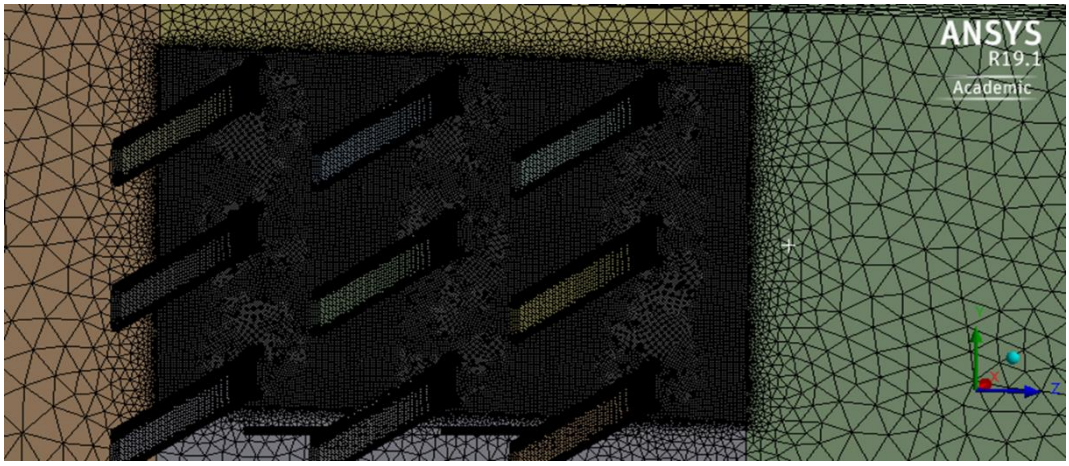

Figure 5.10: Illustration of tetrahedral and hexahedral mesh zones

In Figure 5.10 it can be seen that the fluid geometry surrounding the THPs is split into five different sections, the “inlet” section in front, the “outlet” section behind, the “side” section to the side, the “top” section above and the “bottom” section below the THPs. These sections are of less importance, therefore unstructured tetrahedral meshes were created on these sections as they are less time consuming to generate.

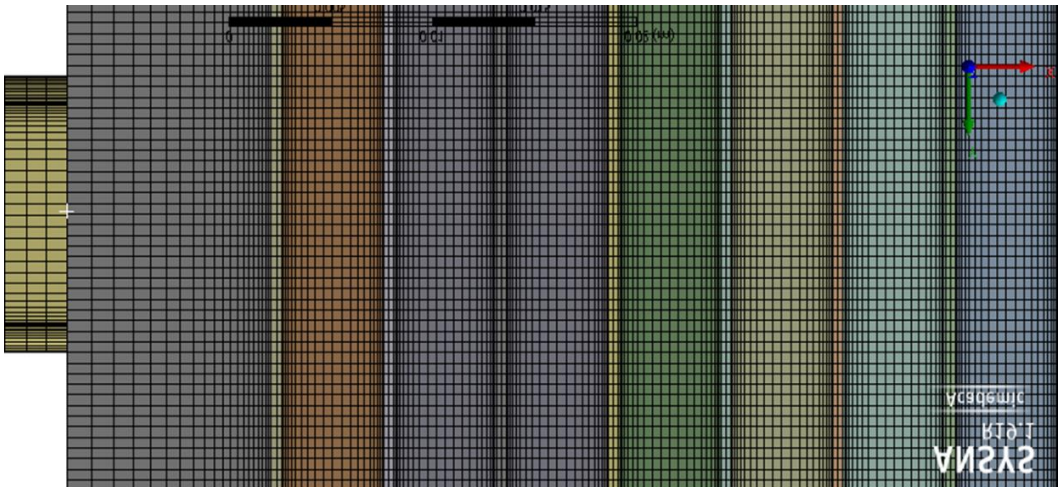

Figure 5.11: Detailed view of hexahedral mesh between the fins

It can be seen in Figure 5.11 that the THP solid and internal fluid mesh sections are entirely composed of hexahedral cells. This was done to accurately capture the steep velocity gradients of the near wall boundary layer while simultaneously decreasing the computational time of the simulation. From Figure 5.11 it can also be seen that bias factors were used to increase the cell size away from the fin walls (typically a bias factor of 8). The edges of the fins were given an element sizing of 0.25 mm, whilst an element sizing of 0.5 was allocated to the edges of the endcaps and evaporator section of the THPs. The mesh had a universal growth rate of 1.3.

To improve the overall quality and reduce the computational expense of the mesh, the tetrahedral mesh sections were converted to polyhedral elements in the Fluent solver. The comparison between the initial and converted mesh can be seen in Table 5.4.

Table 5.4: Comparison between tetrahedral and polyhedral meshes for the THP simulations

	Mesh	
	Tetrahedral	**Polyhedral**
Elements	17373485	15402766
Faces	47516849	53453858
Nodes	13613694	23496172
Minimum orthogonal quality	0,111594	0,136183

5.2.3 Boundary conditions

This section discusses the boundary conditions for each named section created during the meshing phase. Figure 5.12 and 5.13 illustrate these sections.

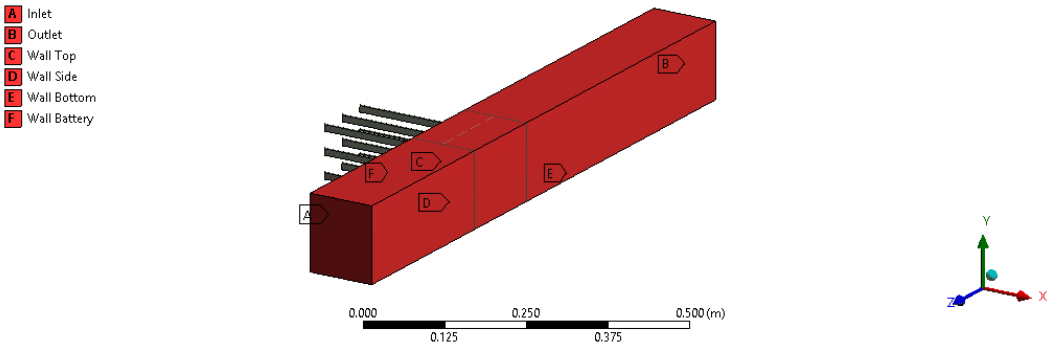

Figure 5.12: Outer boundary conditions

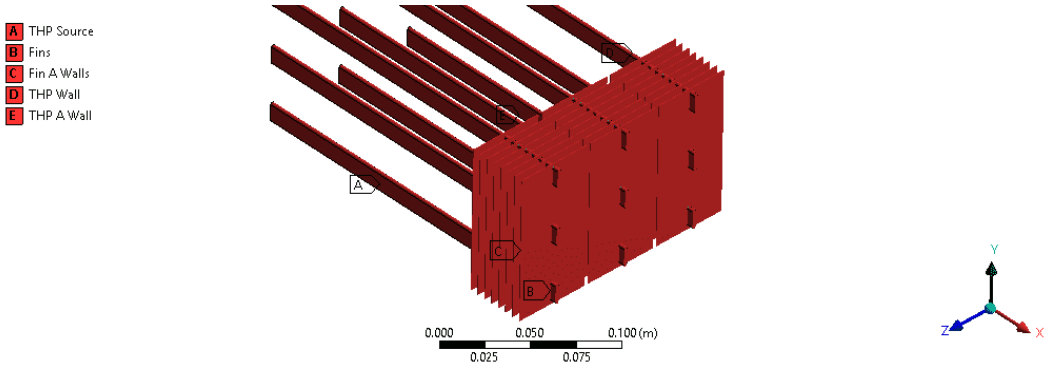

Figure 5.13: Inner boundary conditions

The “Wall”, “Inlet”, “Outlet” sections were classified the same as Section 5.1.3. Since the operating point for the THP BTMS differed from the aluminium plate BTMS, the mass flow rate at the outlet was specified as 0.0872 kg/s. Using Equation 5.1 the turbulent intensity at the inlet was calculated to be 4 %

The walls of the solid zones (THPs) located inside the fluid domain were given a “Coupled” boundary condition, to represent an interfacial boundary condition between a fluid zone and solid zone.

The “THP Source” sections were given a constant heat flux boundary condition, since the temperature across these surfaces are not constant. This heat flux was calculated to be 456 W/m^2. The calculations to determine this heat flux can be seen in Appendix C.

5.2.4 Control parameters

This section describes the control parameters used for the THP simulation.

The simulation was treated as steady state and solved with a “Pressure-Based” solver. Gravity was enabled and assumed to be -9.81 m/s^2 in the y-direction. To determine the heat transfer of the THPs, the energy equation was enabled. As with the first simulation it was decided to use the SST k-ω turbulence model.

The air properties were taken at a temperature of (25 °C). The copper was modelled as pure copper. The THPs were modelled as super conductors according to the method of Chong et al. (2016) specified in Section 2.5.2. A new material was created and assigned to the THPs. The properties for this material as well as the properties of the copper and air used in this simulation are specified in Table B.6 in Appendix B.

The “Coupled” pressure velocity coupling was used. The gradient for the spatial discretization scheme was set to “Least Squares Cell Base”. The “PRESTO!” pressure spatial discretization scheme was used. Lastly the spatial discretization schemes for the momentum, energy, turbulent kinetic energy and specific dissipation rate were set to “Second Order Upwind”.

The residuals were set to 1e-6 for the energy equation and 1e-3 for the velocity, k and omega equations. To initialize the simulation the hybrid initialization method was used.

The convergence levels of the simulation is shown in Appendix G. It can be seen that the solution converged after approximately 110 iterations. Report definitions were also created to monitor the convergence of the temperature of the first fin, the inlet and outlet velocity.

6 Experimental Study

This section focuses on the experimental set-ups, procedures and data analysis.

6.1 Background

The first experiment focuses on the existing Battery Thermal Management System (BTMS) of the Mellowcabs Electric Vehicle (EV). The experiment follows a similar method to Panchal (2016) and Chen et al (2018) in order to determine the effect of the BTMS on the thermal characteristics of the Li-ion cells at a constant charge and discharge rate. The method involved attaching T-type thermocouples at specific locations on the surfaces of the $LiFePO_4$ cells and BTMS to monitor the cell temperatures during charging and discharging, as well as cooling. The second experiment followed a similar procedure, however the cells were cooled with the improved thermosyphon heat pipe (THP) BTMS.

To conduct the experiments, the cells were connected to a modified test bench developed by Van Zuydam (2018). The reason for the modification was to accommodate the addition of three more Li-ion cells for the purpose of testing the effects of the BTMS on the temperature distribution in the cells. The test bench utilises an electric circuit along with a microcontroller to control the loading condition, as well as to monitor the voltages of the cells. The specifications of these $LiFePO_4$ cells can be seen in Table B.1.

The thermocouple calibration was performed using a Fluke 9142 calibration device. The calibration method, along with the results is shown in Appendix E. In addition to this, an experimental uncertainty analysis was conducted, with the procedure and results presented in Appendix F.

All of the experiments were carried out in the Heat Transfer Laboratory of Stellenbosch University.

6.2 Electrical Circuit Design

The experiments were conducted on a modified test bench that consists of an electric circuit and microcontroller to control and monitor the loading conditions of the cells. The following subsection describes the electrical circuit.

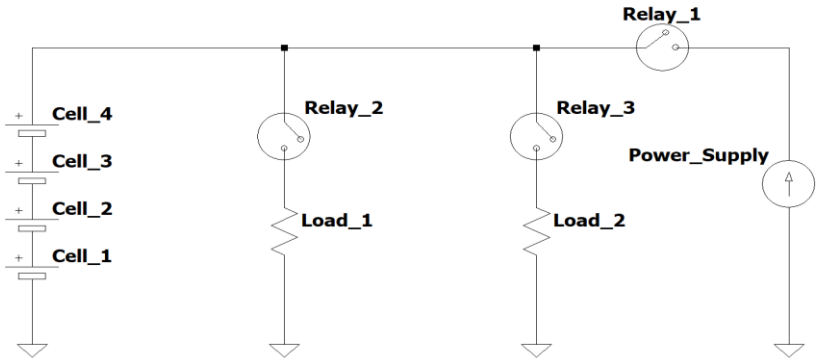

Figure 6.1: Electrical circuit for the experiments

Figure 6.1 illustrates the electric circuit that was set up for the experiments. The electric circuit was constructed using heavy duty copper wire with the thickness depending on the current travelling through the specific section. Since the Electro-Automatik BCI 84-40R programmable battery charger was programmed to supply a constant current of 25 A, resulting charge rate of 0.33 C. Special care was taken to ensure that the various cable lengths never exceeded 4 m and the minimum cross sectional areas of the copper wire were 16 and 25 mm^2 depending on the lengths. Table 6.1 illustrates the minimum recommended cross sectional areas for cables of various lengths conducting different currents.

Table 6.1: Minimum cross sectional area for cables conducting various currents (Electro-Automatik, 2012)

Charging current	**Cable length 0-1,5 m**	**Cable length 1,5-4 m**
0-20 A	6 mm^2	10 mm^2
20-40 A	16 mm^2	25 mm^2
40-60 A	25 mm^2	35 mm^2

The circuit features three heavy duty 30 A, 30 VDC Songle® relays, the first of which connects the Li-ion cells to the programmable battery charger and the other two connecting the loads to the Li-ion cells. To decrease the discharge time it was decided to discharge the cells at 0.4 C. This meant connecting two loads, each consisting of thirteen 10 Ω, 20 W Axial Wirewound resistors connected in parallel, as seen in Figure 6.2. Calculations detailing the electrical circuit design can be found in Appendix C.

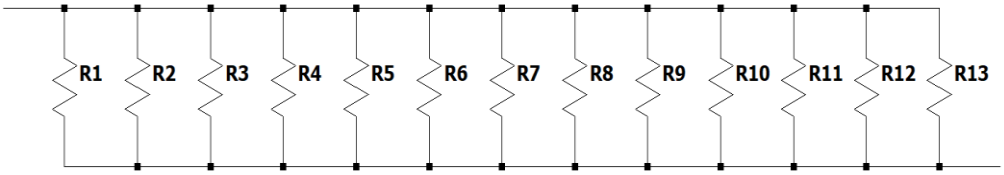

Figure 6.2: Load resistor layout

The microcontroller used to control the loading condition and monitor the cell voltage was a Generic UNO R3 microcontroller that is compatible with the Arduino® software. The Arduino® Integrated Development Environment (IDE) was programmed to initially allow the cells to discharge until one of them experienced a voltage smaller than 2.8 V. After which it would open the second and third relays and close the first to start the charge cycle. The cells would then charge until one of them reached a voltage of 3.5 V. Where after the first relay would open and the second and third would close, repeating the cycle. These upper and lower limits correspond to approximately 80 % and 20 % SOC respectably (Horn, 2017).

Since the cells were connected in series, the maximum charge voltage was 14 V. A voltage divider circuit was constructed to measure the voltage of each cell relative to ground. This was to ensure that the measured input voltage was below the 5 V maximum logic operational voltage of the Generic UNO R3 microcontroller. Figure 6.3 illustrates the voltage divider circuit.

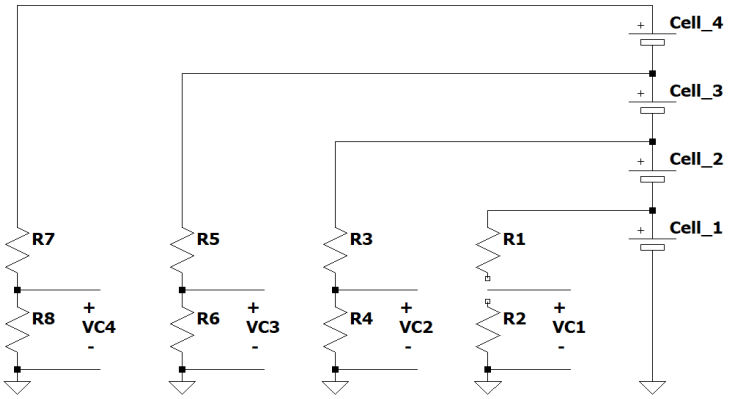

Figure 6.3: The voltage divider circuit

The analog signal was converted back to the appropriate voltage in the Arduino® IDE. It is important to note that since the cells were connected in series the voltage measured at for example VC3, was the sum of all the voltages below it i.e. the sum of voltages VC1, VC2 and VC3. The relevant Arduino® IDE code can be found in Appendix D.

The constructed circuit caused some of the data to become distorted. Therefore, similar to Horn (2017), a low-pass filter was added to the Arduino IDE code. The low pass filter can be expressed as follows:

$$y(i) = y(i-1) + \alpha(x(i) - y(i-1)) \tag{6.1}$$

Where $y(i)$ is the filtered output value, $y(i-1)$ is the previous filtered value, $x(i)$ is the raw input value and α is the filter strength formulated as:

$$\alpha = 1 - e^{-\omega_c T_s} \tag{6.2}$$

with ω_c being the cut-off frequency and T_s the sample period.

In order to convert the acquired data into usable Excel® format a Parallax® Data Acquisition tool (PLX-DAQ) was used, along with the Generic UNO R3 microcontroller.

6.3 Experiment 1: Thermal Characterisation of Aluminium cooling plate BTMS

The first experiment focussed on identifying the surface temperature of the cell and aluminium cooling plates during charging and discharging at constant rates of 0.33 C and 0.4 C respectively. In order to compare the two BTMSs the cells were cycled through several charge/discharge cycles for approximately 4 hours, after which a cooling fan was switched on and the effect of the aluminium cooling plate BTMS on the cell temperatures were monitored. The experiment was also conducted with the cooling fan switched on from the start to monitor the steady state conditions. The following subsections describe the experimental setup and procedure in more detail.

6.3.1 Experimental Setup

The test bench used in this experiment was originally developed by Van Zuydam (2018) to characterize the thermal characteristics of a single $LiFePO_4$ cell. However as mentioned in Section 6.1 it had to be modified to accommodate the addition of 3 more cells, in order for it to more accurately represent the cooling effect of the BTMS in the reference battery pack. The schematic of the hardware configuration of the modified test bench is shown in Figure 6.4.

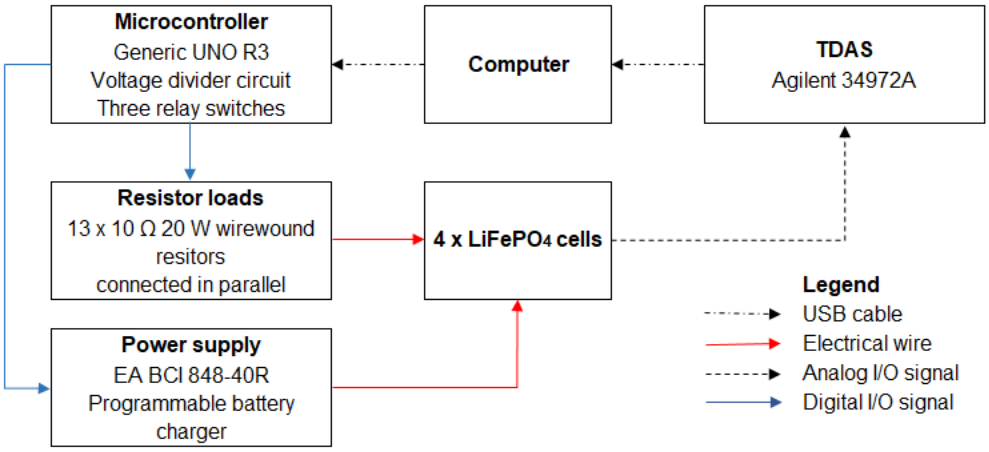

Figure 6.4: Hardware configuration of experimental setup

The personal computer (PC) provides the basic controls from the Arduino® IDE to the Generic microcontroller via a USB cable. The PC also provides a way for the user to track the progress of the experiment via the PLX-DAQ and Agilent benchlink software. The Generic UNO R3 microcontroller uses digital input/output (I/O) lines to communicate with the relays and analog I/O signals to measure the voltages of the cells. If the voltage is zero the IDE will read 0 bits, if the voltage is 5 V the IDE will read 1023 bits and any voltage in between will cause the Arduino IDE to read a number between 0 and 1023 that is proportional to the voltage being applied to the analog pin (Arduino, 2019). The detailed experimental setup and components can be seen in Figure 6.5

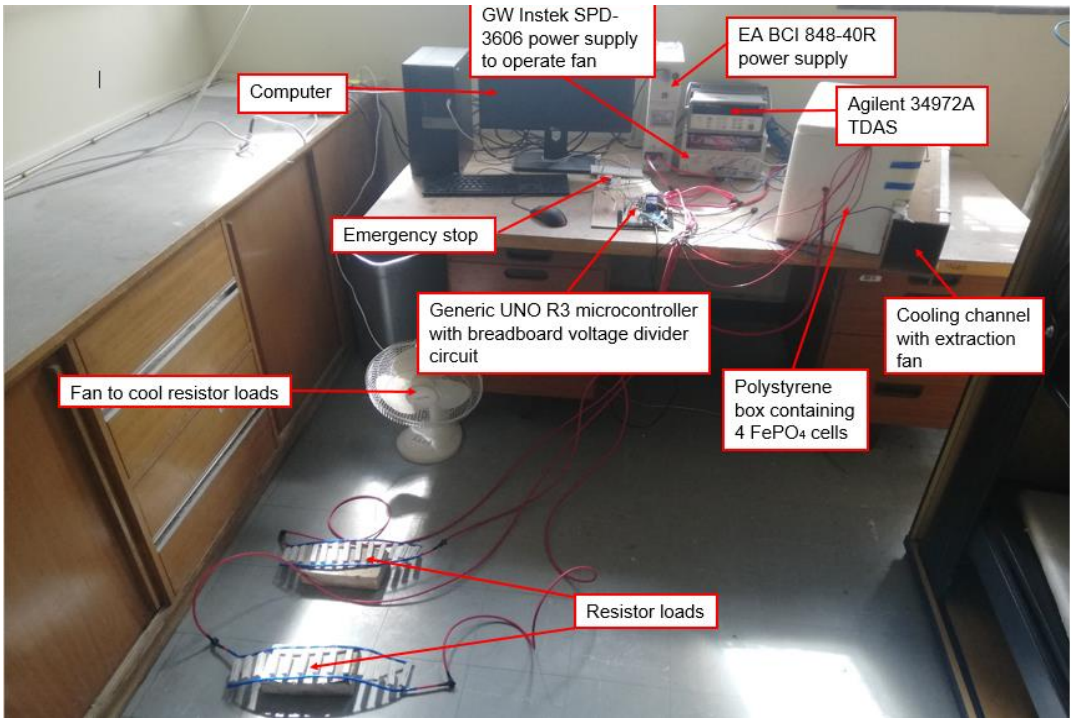

Figure 6.5: Detail layout of experimental setup

To capture and store the thermocouple measurements an Agilent 34972A Thermal Data Acquisition System (TDAS) was used. As mentioned in Section 6.1, the temperatures were taken at specific locations on the cells and BTMSs. Panchal (2016) concluded that most of the heat will be generated close to the terminals, therefore the cell temperatures will be monitored with 6 thermocouples on the top of the cells close to the terminals, as illustrated in Figure 6.6.

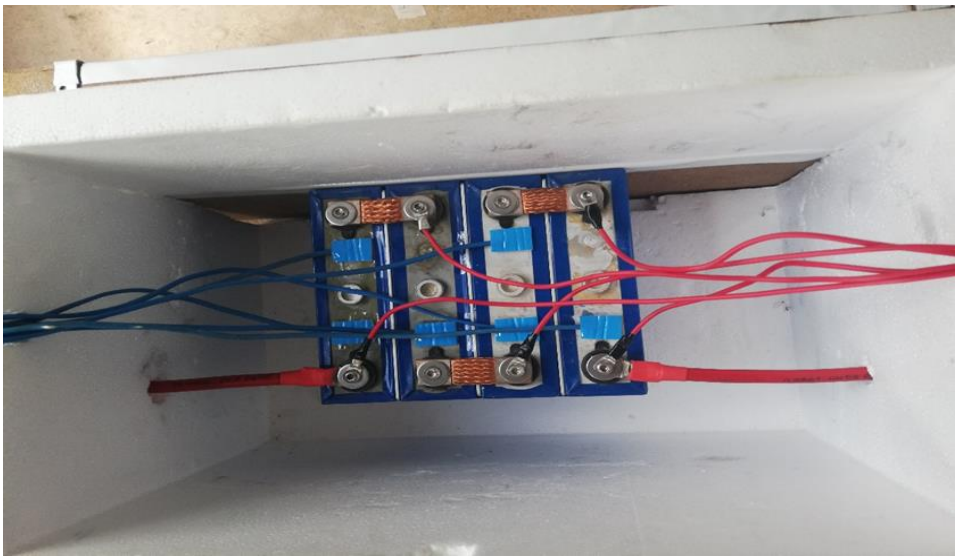

Figure 6.6: Final connected Li-ion cells in polystyrene box

To monitor the temperature on the BTMS, three thermocouples were placed on each aluminium plate that extends into the cooling channel. The cooling channel was cut from 3.2 mm Masonite board with special grooves for the aluminium plates placed 300 mm from the entrance and spaced 49 mm apart (the width of the $LiFePO_4$ cell). At the end of the cooling channel there was a 24 V, 138 CFM Sunon® extraction fan. The purpose of the fan was to enable heat transfer via forced convection from the aluminium plates extending into the cooling channel, as illustrated by Figure 6.7.

Figure 6.7: Aluminium fins extending into the cooling channel

The fan was powered by a GW Instek© SPD-3606 power supply. The ambient/inlet temperature was monitored with a single probe thermocouple at the entrance of the cooling channel. The outlet temperature was also monitored at a specific distance off from the last aluminium plate. To ensure that the cells are well insulated and to reduce the contact resistance between the cell walls and the aluminium plates, the cells and aluminium plates were pushed together and taped. The bus bars connecting the cells also ensured that the aluminium plates are compressed tightly between the cells.

After the cells were connected they were placed in a polystyrene foam box adjacent to the cooling channel and connected to the rest of the circuit as illustrated by Figure 6.6. The temperature inside the box was monitored with a thermocouple. The box ensured that the temperatures of the cells are not affected by the heat generated by the loads during charging and discharging, or the ambient temperature. The room in which these experiments were conducted also features an air-conditioning system that enabled the user to keep the ambient room temperature at $\pm$20 °C. All the thermocouples were attached with double sided tape to prevent the ambient temperatures from compromising the readings. The locations of these thermocouples are illustrated in Appendix D.

6.3.2 Experimental Procedure

The experimental procedure is summarized in the flow diagram below:

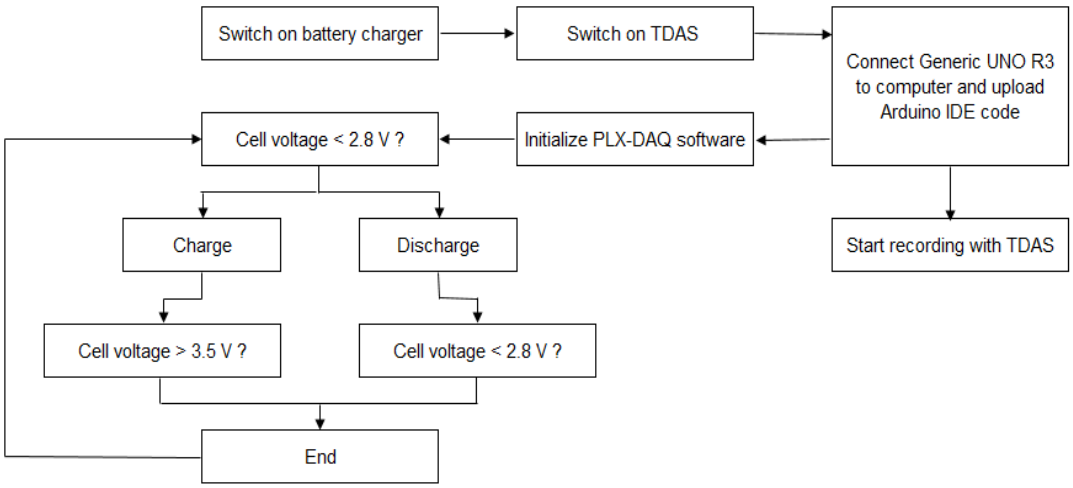

Figure 6.8: Summary of experimental procedure

6.4 Experiment 2: Thermal Characterisation of Thermosyphon Heat Pipe BTMS

The second experiment utilized the same test bench as the first experiment but with a different BTMS. For this experiment the aluminium cooling plates were replaced with the THP BTMS. Since this experiment was conducted on the same test bench as the first experiment the experimental procedure stayed the same. This was done in order to accurately compare the effects of the two BTMSs on the cell temperatures.

6.4.1 Experimental Setup

The main difference in the experimental setup from that of the first experiment is the application of the THP BTMS. As mentioned in Section 3 these THPs were designed to replace the aluminium cooling fins between the Li-ion cells. The module clamps of the battery pack had to be adjusted to accommodate attaching them onto the current Mellowcabs EV. These new clamps consist of two plastic covers that cover the top and bottom of each cell, leaving the middle bit exposed for the THP to fit in as illustrated by Figure 6.9. In this figure one can also see that the THPs were orientated at a slight angle in order to allow the condensate to drip down from the condenser side to the evaporator section.

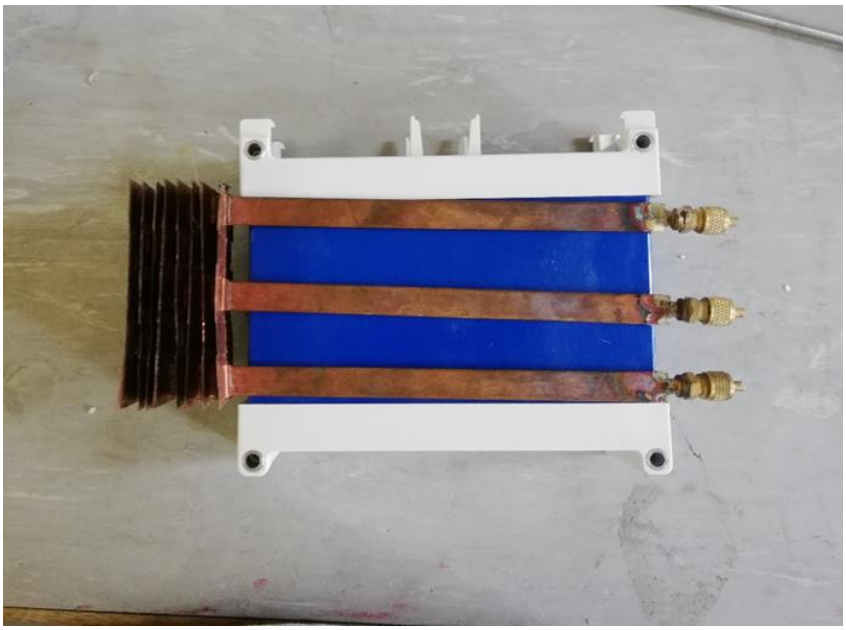

Figure 6.9: THP orientation between the new clamps

The cells were stacked on top of each other with a THP in between each cell and then tightly pulled together by four 250 mm M6 threaded rods that slide through the four holes in the corner of the cell covers. During this assembly process two thermocouples were placed at specific locations on each cell to measure the temperature of the THP evaporator section. After the cells have been tightly pulled together they are inserted into the polystyrene box and connected to the test bench circuit as seen in Figure 6.10.

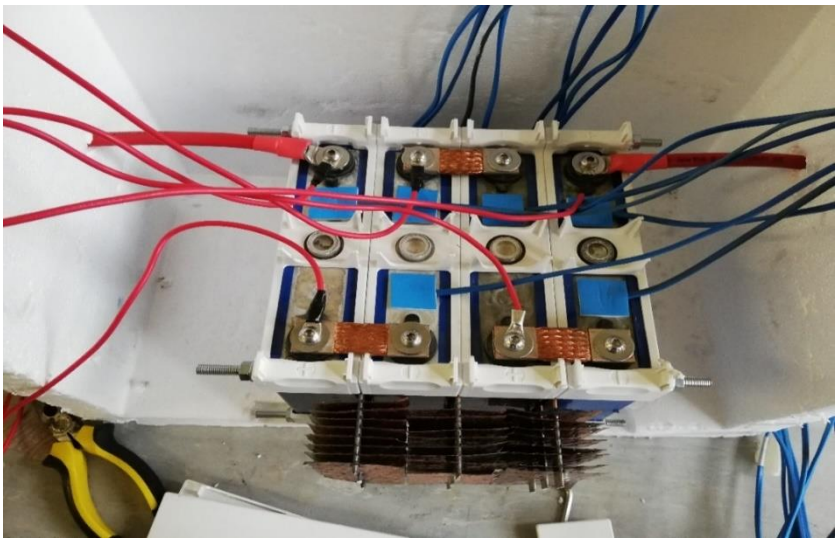

Figure 6.10: Illustration of the connected Li-ion cells and THP BTMS

After connecting the cells to the electrical circuit, the cooling channel is connected and the polystyrene box closed. The THP condenser sections protruding into the cooling channel can be seen in Figure 6.11.

Figure 6.11: THP inside the cooling channel

There was also a thermocouple connected to the end of one of the THP condenser sections. This measurement was later used with the measurements on the evaporator section to validate the numerical temperature distribution of the THPs.

In order to compare the effect of the two BTMSs on the temperatures of the cells, six thermocouples were placed at the exact same locations on the top of the cells for both experiments (see Figure 6.10). The specific locations of these and all other thermocouples can be seen in Appendix D.

7 Results and discussion

This chapter presents the results obtained from the analytical solutions, presented in Chapter 4, the numerical solutions, presented in Chapter 5, and the experimental study, presented in Chapter 6.

7.1 Heat generation results

As mentioned in Section 6.2 a low pass filter was included in the Arduino Integrated Development Environment (IDE) code. This however did not completely filter out the distorted data, hence the Savitzky-Golay filter was used in MATLAB®. The charging and discharging voltage profiles for a single cell can be seen in Figure 7.1. It can be seen that the discharge cycle is significantly shorter than the charge cycle. This is because the cells were charged at 0.33 C and discharged at 0.4 C, as mentioned in Section 6.2.

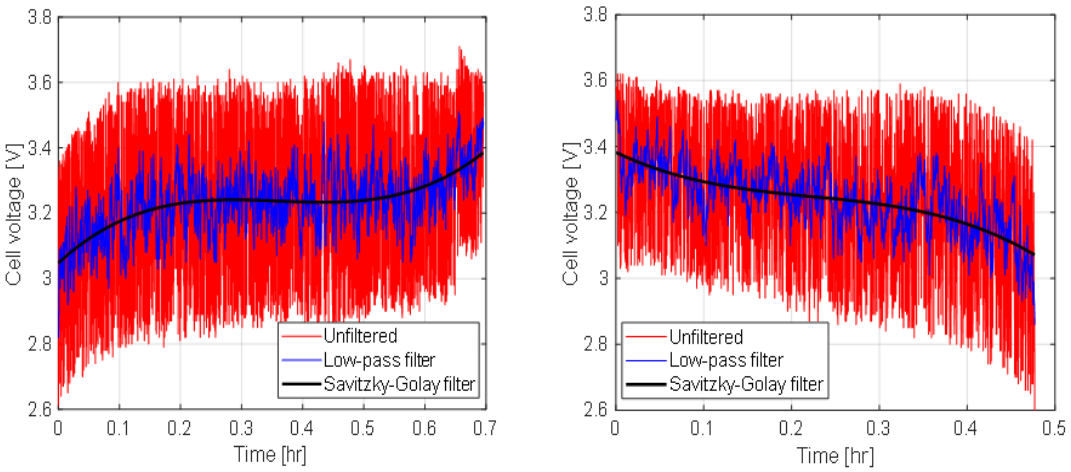

Figure 7.1: The measured charging (left) and discharging (right) voltage profiles of a single cell

Figure 7.2 illustrates the voltage profiles in terms of State of Charge (SOC) for each cell during a charging and discharging cycle. It was noted that the voltage profiles differ for each cell. The probable reason for this was that the cells were at the end of their lifespan. Therefore the internal resistances of the cells, and possible bad connections, had an effect on the charging and discharging rate of the cells.

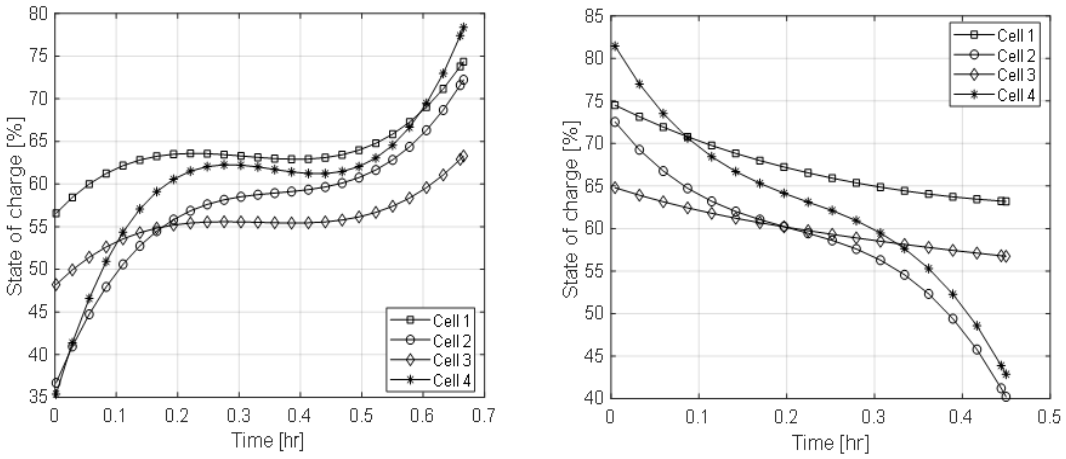

Figure 7.2: Voltage profiles in terms of SOC for each cell during a charge (left) and discharge (right) cycle

From Figure 7.2 it can be seen that the charge and discharge limit was controlled by the voltages of Cell 4 and cell 2 respectively. By using these voltage profiles as inputs to the equations by Inui et al. (2007) in Section 4.1, it was possible to generate the theoretical heat generation rate plots as seen in Figure 7.3. Rust (2017) conducted a study on the internal resistance and capacity of the cells in the reference battery pack. Using the results of this study an experimental heat generation rate was determined, and plotted alongside the theoretical results.

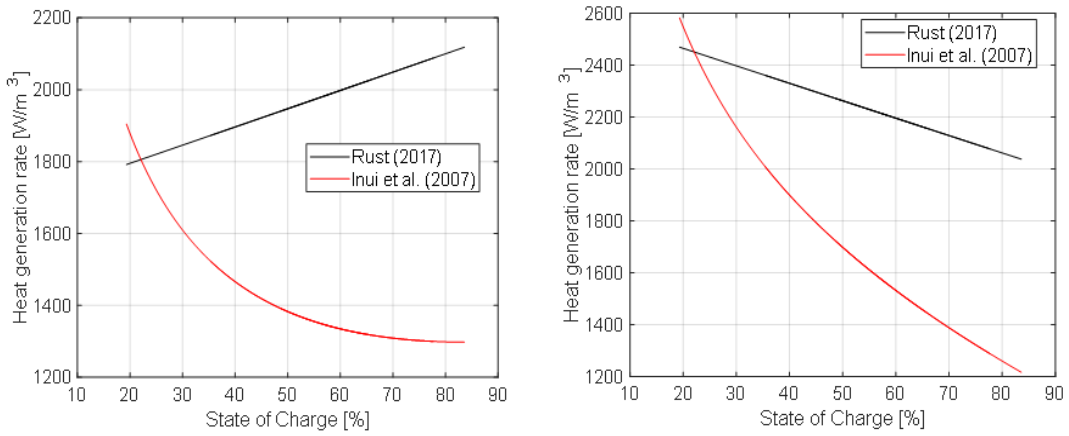

Figure 7.3: Heat generation rate during a charge (left) and discharge (right) cycle

From Figure 7.3 it can be seen that there is a distinct difference between the charging and discharging heat generation curves. This is due to the assumption that the change in entropy is negative under discharging conditions, causing the second term in equation 4.6 (the heating due to irreversible entropy change) to become positive.

7.2 Aluminium plate BTMS results

This section presents the analytical, numerical and experimental results of the aluminium plate BTMS.

In order to accurately compare the different results, the operating conditions were chosen to be identical for all three cases. The properties of the ambient air supplied to the system was determined at 22.5 °C. According to the fan curve in Appendix B, the intake velocity at the operating point was 5.9 m/s. The sample calculations of the work presented in this section are shown in Appendix C.

7.2.1 Comparison of analytical and numerical results

In order to improve the accuracy of the analytical model, the average air velocity magnitude flowing over the second and third fins was obtained from the Computational Fluid Dynamics (CFD) simulations. To calculate this average four lines were created along the cooling channel. These lines are illustrated in Figure 7.4, the average velocity magnitude along these lines is shown in Figure 7.5.

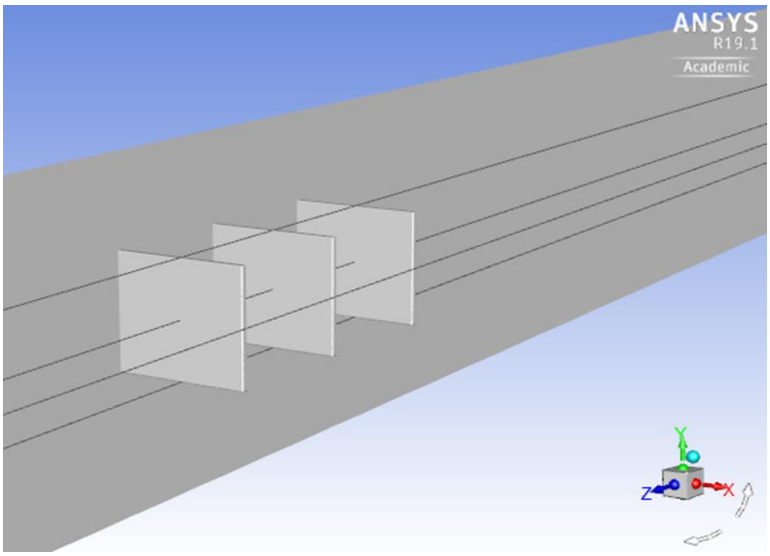

Figure 7.4: An illustration of the lines used to determine the average velocity, pressure and temperature along the cooling channel

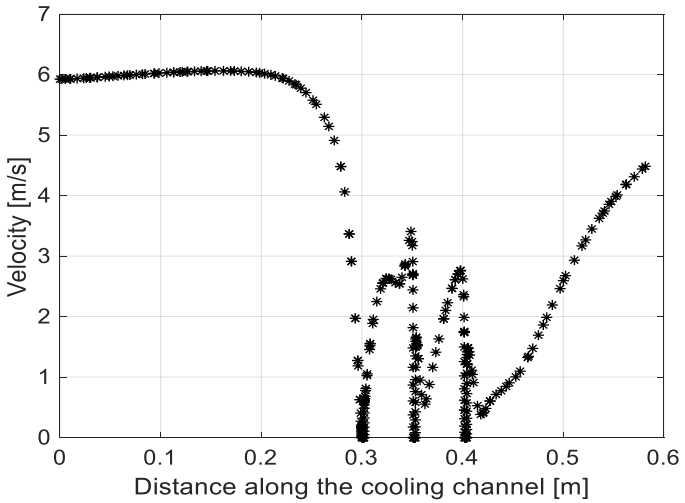

Figure 7.5: Average velocity magnitude along the cooling channel for the aluminium plate BTMS

In Figure 7.5 it can be seen that the velocity at 0.3 m, 0.35 m and 0.4 m from the entrance approaches zero, as these are the locations of the fins. The average velocity of the air flowing over the second and third fin can be read off to be 3.4 m/s and 2.8 m/s respectively.

The difference in the air velocity flowing over each fin was as a result of the low pressure wake left by the first fin. This influenced the convective heat transfer coefficient of each fin. Using the lines in Figure 7.4, the average total pressure drop along the cooling channel is shown in Figure 7.6. It can be seen that the fins caused a maximum pressure drop of just over 50 Pa.

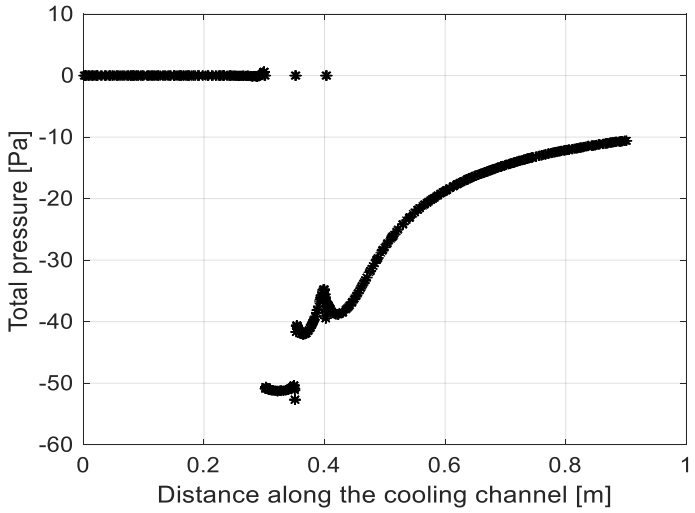

Figure 7.6: Total pressure along the cooling channel for the aluminium plate BTMS

A comparison of the analytical and numerical average temperature, convective heat transfer coefficients and the heat dissipated by each fin, is shown in Table 7.1. In this Table it can be seen that there is an average difference of 6 % between the two sets of results

Table 7.1: Comparison of the analytical and numerical results of the aluminium plate BTMS

	Analytical			Numerical		
	Fin 1	**Fin 2**	**Fin 3**	**Fin 1**	**Fin 2**	**Fin 3**
Average temperature [°C]	25,99	26,28	26,36	26,06	26,21	26,31
Heat transfer coefficient [W/m^2·K]	63,92	44,94	40,49	59,28	49,53	48,9
Heat dissipated [W]	0,8425	0,6378	0,5844	0,8814	0,7468	0,7451

The decrease in heat dissipated from the fins along the cooling channel as presented in Table 7.1, can be justified when looking at the streamlines illustrated in Figure 7.7. In this figure the low pressure wake left by the first fin is clearly illustrated.

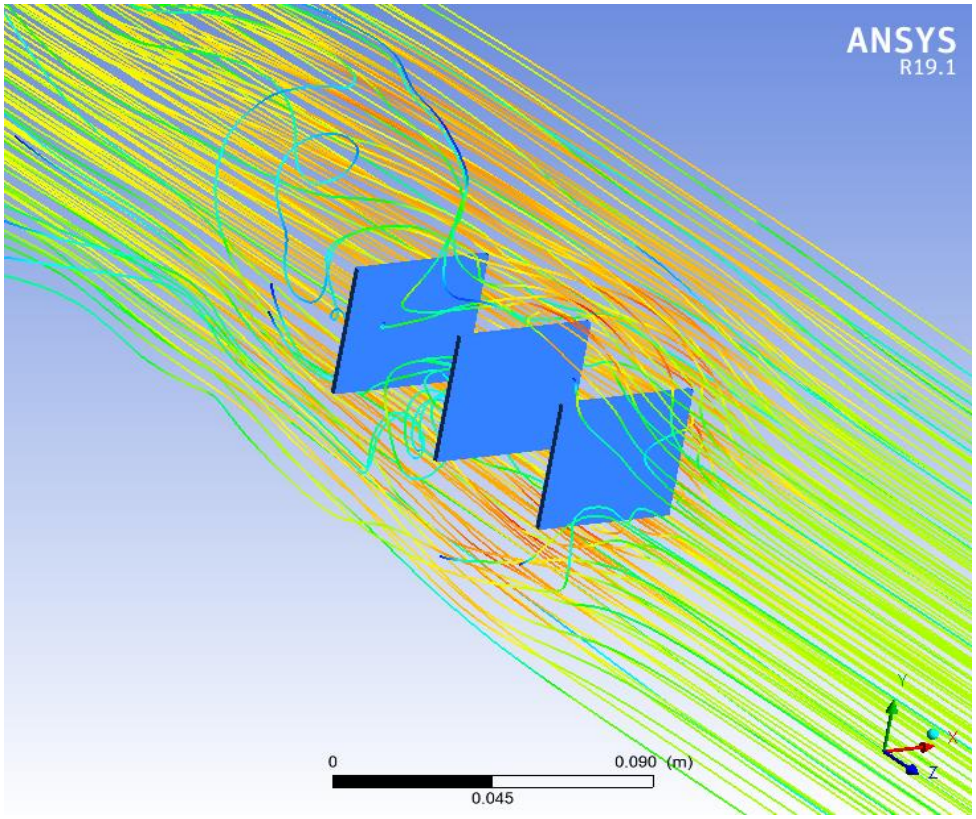

Figure 7.7: Illustration of the streamlines of the aluminium plate BTMS simulations

7.2.2 Experimental verification of the numerical results

A comparison of the analytical and numerical fin temperature distributions are shown in Figure 7.8. These temperatures represent the temperatures from the bases to the tips of the fins. Using the velocities from Figure 7.5 in the analytical solution, it was possible to generate a more accurate analytical solution. This is evident from the close comparison between the analytical and numerical results in Figure 7.8. The numerical solution for the first and third fin differs slightly from the experimental results. The temperature of fin 1 was over predicted whilst the temperature of fin 3 was under predicted. However the difference in temperatures of the numerical and experimental results is below 0.5 °C.

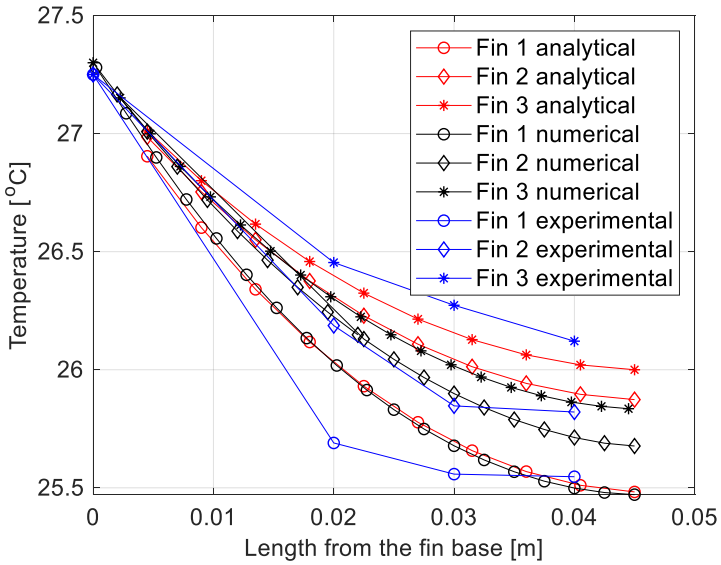

Figure 7.8: Verification of the aluminium fin temperature distribution

The seemingly inversely proportional deviations of the experimental results for fin 1 and 3 as compared to the analytical results could be accredited to a number of reasons. However it is assumed that the main reason is due to the way in which the air flow was modelled in the analytical solutions. For instance a constant average velocity was assumed over each fin. Which in real life is not the case, especially for the fins downstream. This in turn could have affected the calculation of the convective heat transfer coefficient. The addition of the thermocouples to the back of the fins could also have had an influence on the experimental results.

The average temperature distribution along the lines shown in Figure 7.4 is shown in Figure 7.9. It can be seen that there is a close correlation between the experimental, numerical and analytical results.

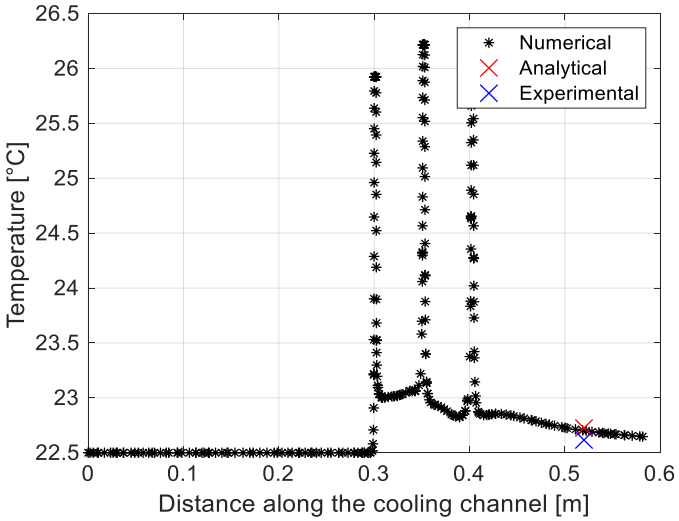

Figure 7.9: Verification of the Temperature along the cooling channel for the aluminium plate BTMS

7.2.3 Experiment 1 results

The effect of the difference in fin temperatures can clearly be seen in Figure 7.10 and 7.11. In Figure 7.10 it can be seen that when the cooling fan was switched on, the temperature drop of cell 1 was 1.497 °C. Whilst the temperature drop of cell 4 was 0.878 °C.

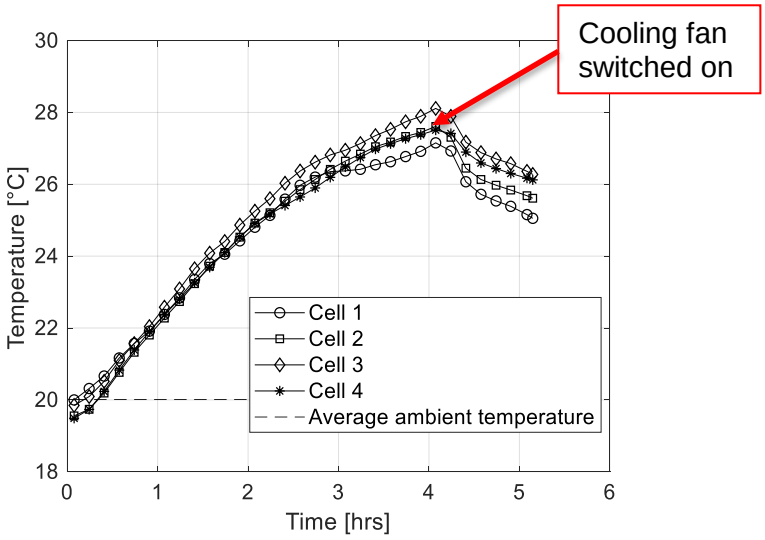

Figure 7.10: Average cell temperatures with cooling after approx. 4 hours for the aluminium plate BTMS

Figure 7.11 compares the average cell temperatures between the cases where the cooling fan was switched on from the start and where the cooling fan was off. It

can be seen that with cooling fan on, the cells reached equilibrium at ± 5 °C above the ambient temperature. The effect of the different fin cooling rates on the temperature of cell 1 is also illustrated, as it is on average 0.6 °C colder than the other cells.

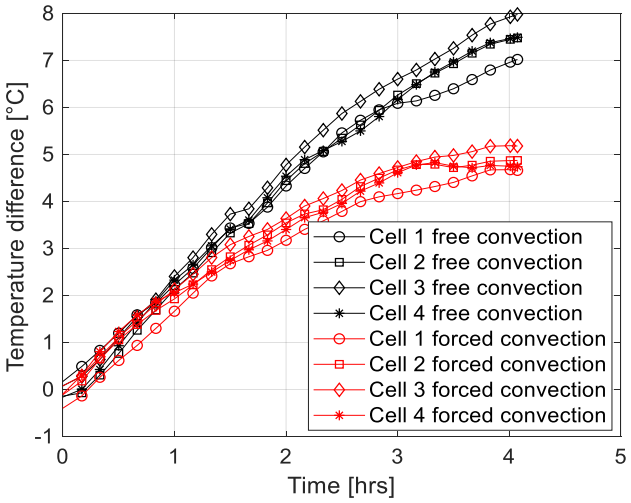

Figure 7.11: Comparison of the average cell temperatures of the first experiment

7.3 Thermosyphon heat pipe BTMS results

This section presents the analytical, numerical and experimental results of the THP BTMS. To accurately compare the different results, identical operating conditions were chosen for all three cases. The properties of the ambient air supplied to the system was determined at 21 °C. According to the fan curve in Appendix B, the intake velocity at the average operating point was 5.1 m/s. The sample calculations of the results from this section are shown in Appendix C.

7.3.1 Comparison of analytical and numerical results

As mentioned in Section 4.3 two different methods were used to calculate the analytical convective heat transfer coefficient of the finned condenser section. The first method was that of Frass (2015) and the second that of Kröger (1998).

The ambient air was modelled at 21 °C. According to the fan curve in Appendix B, the relevant intake air velocity was 4.6 and 5.6 m/s when using the method of Kröger (1998) and Frass (2015) respectively. Since the fins were orientated parallel to the flow, this velocity was assumed constant across the BTMS. A comparison of the results of the two methods is shown in Table 7.2.

Table 7.2: Comparison of the analytical results of the THP BTMS

	Frass	Kröger
Average temperature [°C]	23.82	23.69
Heat transfer coefficient [W/m^{2}K]	62,59	71,52
Heat dissipated [W]	6.4818	7.0743

Since the results of these two methods were relatively similar. It was decided to use the results of the method by Kröger (1998) for the rest of the analytical solution.

To determine the average velocity magnitude over the THPs along the cooling channel, three lines were created along the cooling channel. An illustration of these lines is shown in Figure 7.12. From Figure 7.13 it can be seen that the velocity magnitude increased as it entered the heat sink. This was as a result of the flow separation over the THPs. The average total pressure drop over the THPs along the cooling channel is illustrated in Figure 7.14. From this figure it can be seen that the average total pressure drop as a result of the flow over the THPs was less than that of the aluminium plate BTMS illustrated in Figure 7.6.

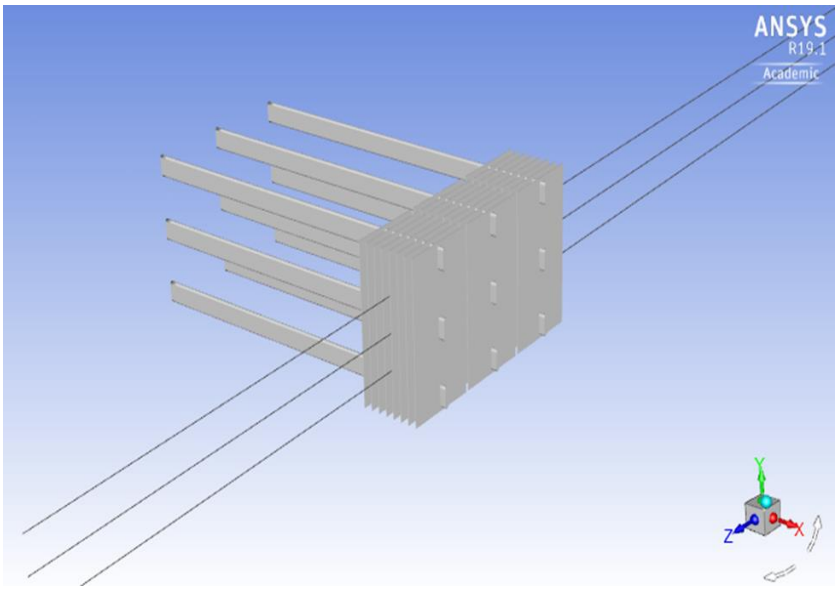

Figure 7.12: An illustration of the lines used to determine the average velocity, pressure and temperature along the cooling channel

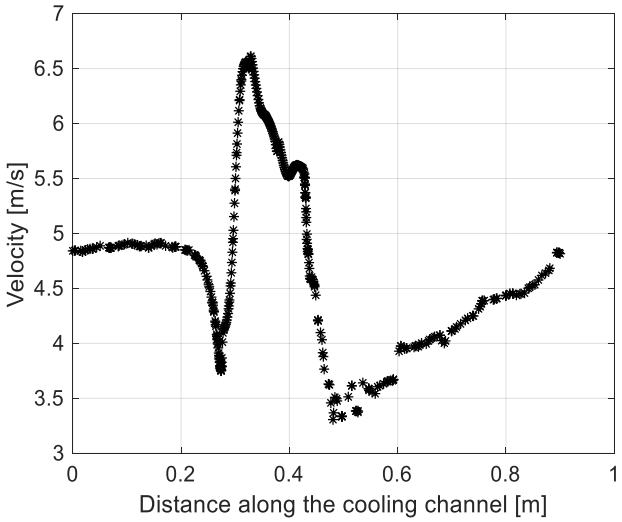

Figure 7.13: Average velocity along the cooling channel for the THP BTMS

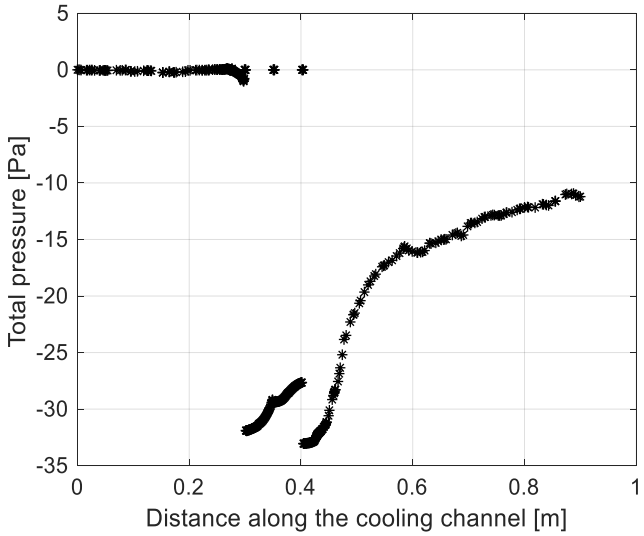

Figure 7.14: Total pressure along the cooling channel

A comparison of the analytical and numerical results can be seen in Table 7.3. There is a reasonable comparison between the results. The main reasons for the differences can be accredited to the way the THPs are modelled in the numerical solution, as well as the higher heat transfer coefficients predicted by the method of Kröger (1998). This is discussed in the next section.

Table 7.3: Comparison of the analytical and numerical results of the THP BTMS

	Analytical			Numerical		
	THP 1	**THP 2**	**THP 3**	**THP 1**	**THP 2**	**THP 3**
Average temperature [°C]	23,11	23,35	23,6	22,8	23,24	23,56
Heat transfer coefficient [W/m2 K]	71,52	67,08	58,26	68,71	48,24	36,3
Heat dissipated [W]	7,509	6,8338	6,1586	4,7549	4,7931	4,7855

The improvement in the uniformity of the heat dissipation results can be accredited to the improvement of the airflow over the BTMS. Figure 7.15 illustrates the streamlines of the airflow between the copper fins. It can be seen in this figure that there is a definitive improvement over the airflow from the aluminium plate BTMS.

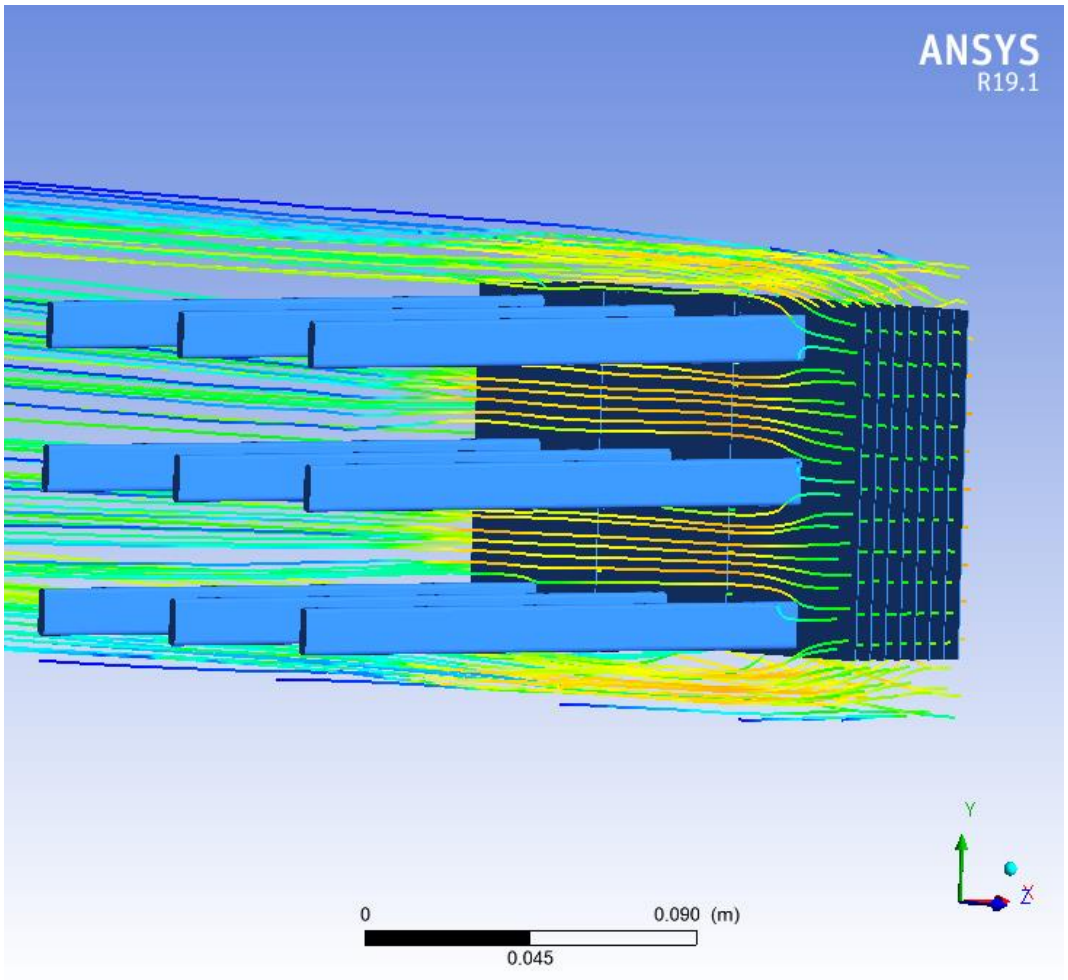

Figure 7.15: Illustration of the streamlines of the THP BTMS simulations

7.3.2 Experimental verification of the numerical results

As mentioned in Section 5.2.3 a heat flux of 456 W/m^2 was applied as input to the THPs. A comparison between the analytical, numerical and experimental temperature distributions in the THPs are shown in Figure 7.16. The origins of the THPs were taken at the evaporator endcaps. As expected from most simplified analytical solutions of THPs, there was an almost constant evaporator and condenser temperature distribution. As a result the temperature distribution in the fins connected to the condenser section were almost identical as evident from the results in Table 7.3. As predicted by Chong et al. (2016) the numerical solution of the THPs slightly under predicted the evaporator and slightly over predicted the condenser temperatures. There was an average difference of 6 % and 4 % in the condenser and evaporator temperatures respectively.

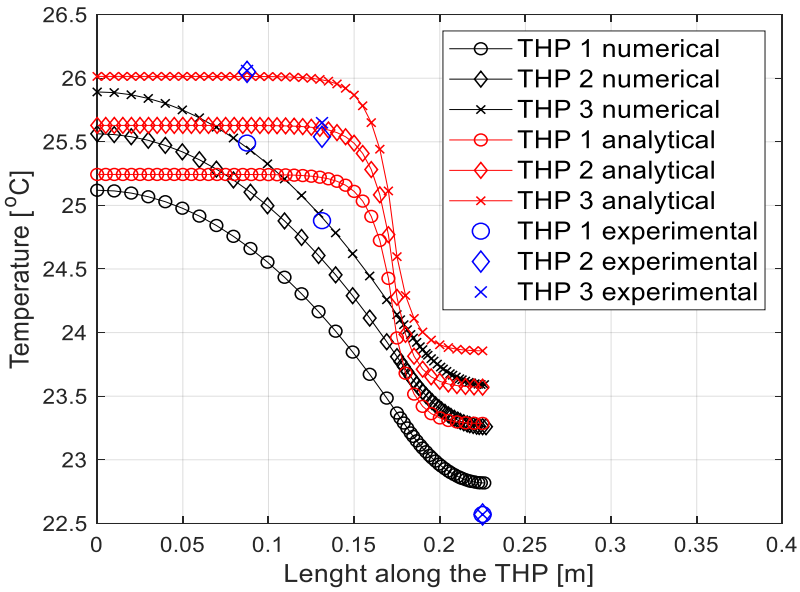

Figure 7.16: Comparison of the analytical, numerical and experimental temperature distributions in the THPs

The middle line from Figure 7.12 was used to illustrate the temperature increase along the cooling channel. This increase is illustrated in Figure 7.17. It can be seen that there was a good correlation between the analytical, numerical and experimental results.

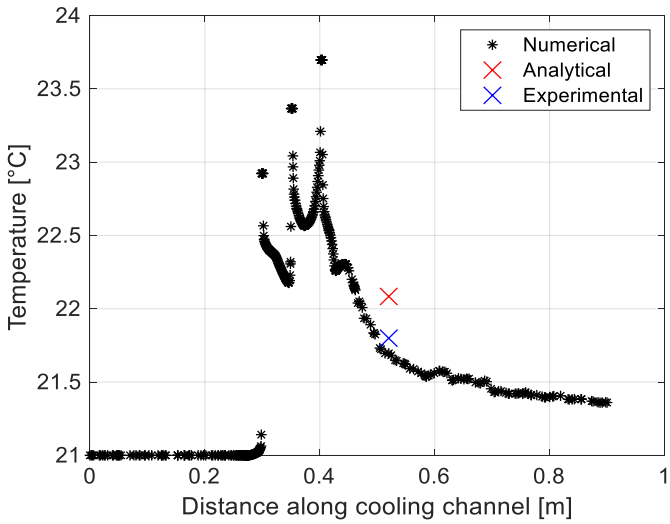

Figure 7.17: The temperature increase along the cooling channel for the THP BTMS

7.3.3 Experiment 2 results

As mentioned in Section 6.4 the second experiment focussed on the thermal characterization of the four Li-ion cells and the THP BTMS. Like the first experiment, this experiment was conducted for two cases. For the first the cooling fan was only switched on after approximately 4 hours and for the second the cooling fan was switched on from the start. Figure 7.18 illustrates the average evaporator temperature for the heating and cooling cycle. It can be seen that the average temperature of the evaporator section drops with $\pm$1 °C when the cooling fan is switched on.

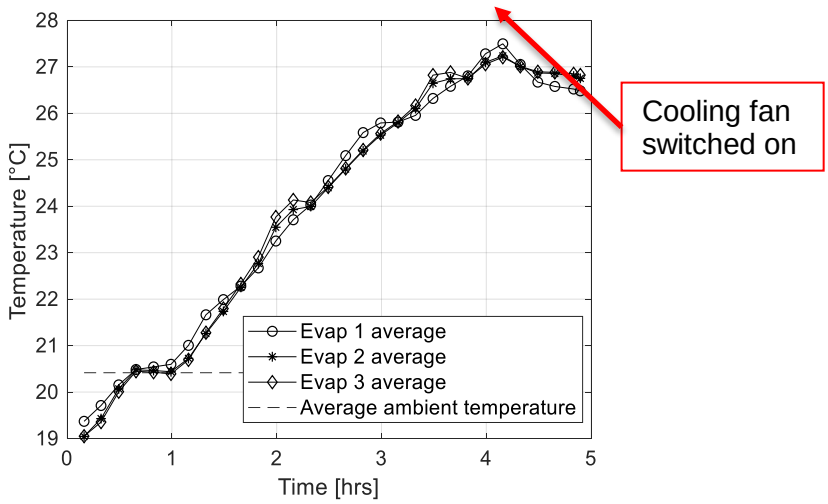

Figure 7.18: Average evaporator temperature when cooling fan is switched on after approx. 4 hours

The effect of the THP BTMS on the average cell temperature is shown in Figure 7.19. In this figure it can be seen that the average cell temperature decreases by ±1.2 °C when the cooling fan is switched on. It can also be seen that there is an improvement in the temperature uniformity of the cells, with the difference in cell temperature ± 0.5 °C.

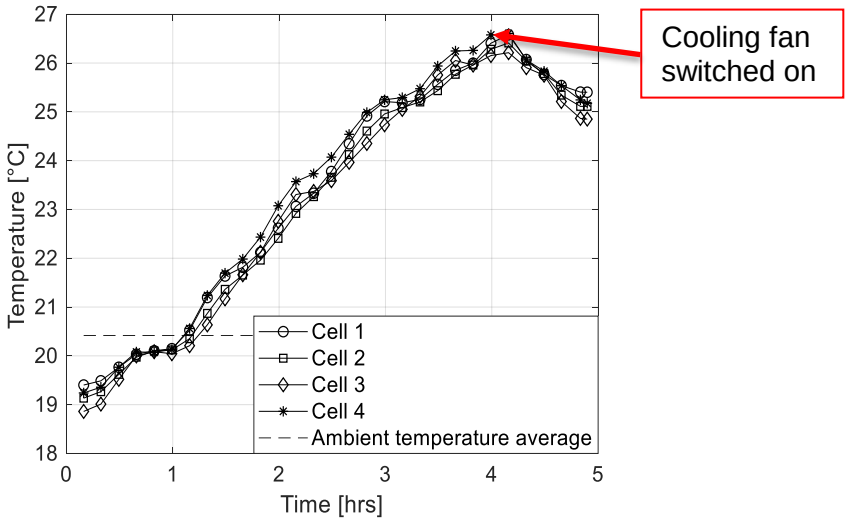

Figure 7.19: Average cell temperature when cooling fan is switched on after approx. 4 hours

The average temperature of the evaporator sections for the second case can be seen in Figure 7.20. It can be seen that at after 4 hours the temperature has risen to ±5 °C above ambient.

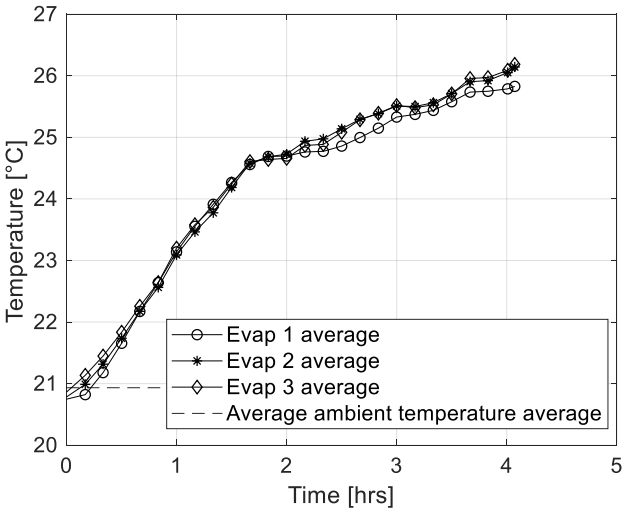

Figure 7.20: Average evaporator temperature when the cooling fan is switched on from the start

A comparison of the average cell temperature for the two cases can be seen in Figure 7.21. In the second case it can be seen that the THP BTMS only started to cool the cells after approximately 1.5 hours. The probable reason for this was that the temperature of the evaporator section had to first reach a certain point, in order for the working fluid to start evaporating. After this point there is a clear difference in the temperatures, with the cells reaching equilibrium at 4 °C above ambient temperature, more than 2 °C lower than the first case.

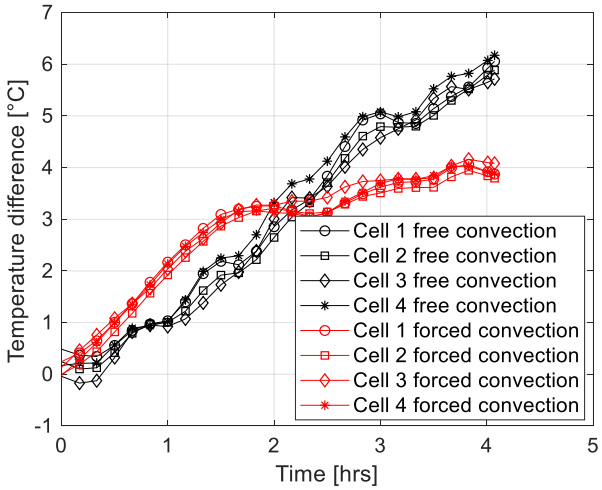

Figure 7.21: Comparison of the cell temperatures of the second experiment

7.4 Comparison of the BTMSs

The systems were compared based on the total heat dissipated and temperature uniformity. This temperature uniformity is resented as the average temperature difference between the temperatures of the four cells. The findings are summarized below in Table 7.4.

Table 7.4: Comparison of the two BTMSs

		Average temperature difference[°C]	Heat dissipated [W]
Aluminium plate	**Analytical**	0,19	2,0647
	Numerical	0,125	2,3733
	Experimental	0,38	2,137
THP	**Analytical**	0,36	20,461
	Numerical	0,32	14,3335
	Experimental	0,28	10,51
	Percentage increase	-36%	589%

It can be seen from the table above, that the THP BTMS dissipates a lot more heat from the cells. This effect is also visible when comparing the cell temperatures in Figure 7.10 and 7.19. The table also shows that there is theoretically no improvement in the temperature uniformity. However the experimental results did suggest a minor improvement.

7.5 Sensitivity analysis

A sensitivity analysis was conducted on the numerical solutions for the quantification of the heat dissipated from each BTMS. The effect of varying the inlet velocity and inlet air temperature on the total heat transfer was plotted in Figure 7.22 and 7.23 respectively. The heat inputs of each BTMS was set to a constant temperature of 26 °C. It can be seen in Figure 7.22 that varying the inlet velocity from 2 m/s to 12 m/s caused a difference in total heat transfer of 1.14 W for the aluminium plate BTMS and 23.15 W for the THP BTMS. It was noted that due to the orientation of the aluminium fins, the increase in air velocity resulted in a decrease in temperature uniformity. This was due to the increase in size of the low pressure wake left by the first fin. As a result the heat dissipated from the second and third fins decreased.

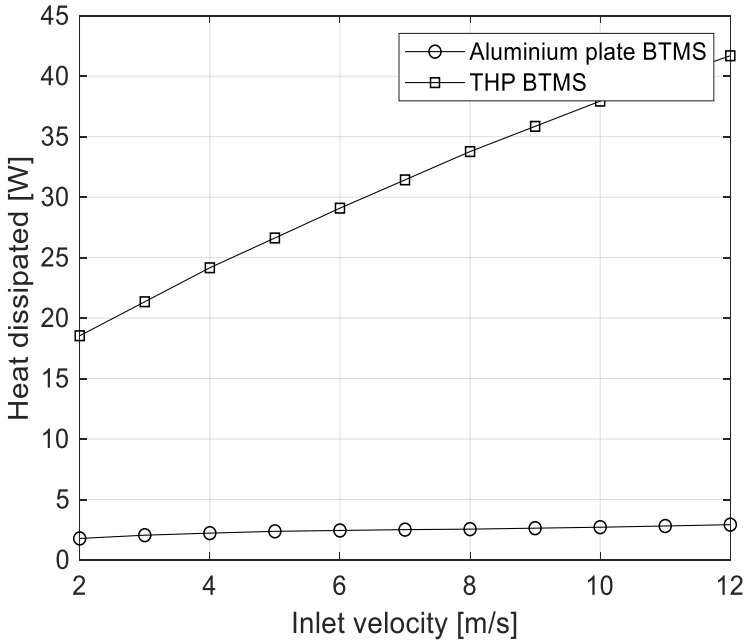

Figure 7.22: The effect of varying the inlet velocity on the heat dissipation

In Figure 7.23 it can be seen that the variation of the inlet temperature resulted in a reduction of 10.1 W and 107.33 W in the heat dissipated from the aluminium plate BTMS and THP BTMS respectively.

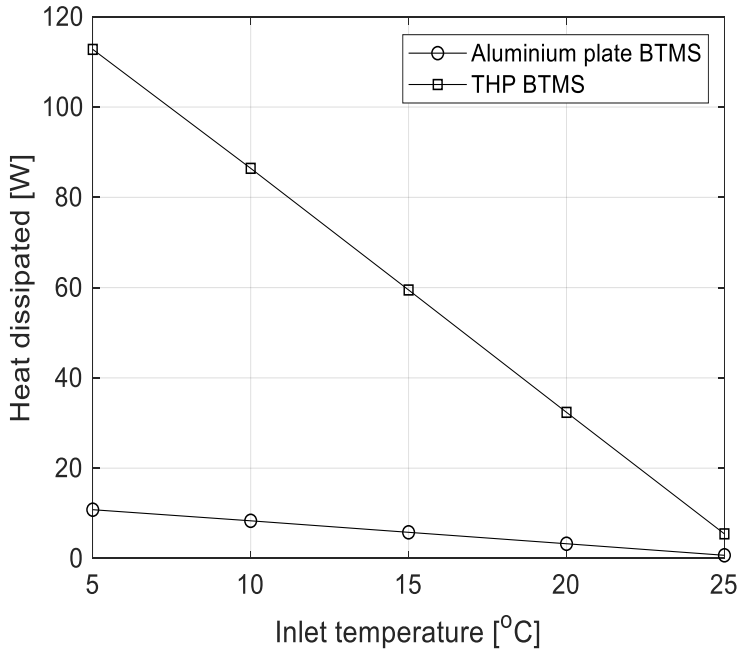

Figure 7.23: The effect of varying the inlet air temperature on the heat dissipation

8 Conclusions and recommendations

The conclusions and recommendations of this thesis are presented below.

8.1 Conclusions

As part of this study, an analytical model was developed for each BTMS. In order to improve these analytical solutions Computational Fluid Dynamics (CFD) simulations were conducted on each BTMS. Experimental studies were performed on a small scale battery pack to characterise the thermal behaviour of each BTMS and Lithium-ion (Li-ion) cells, as well as to verify the CFD simulations. The results were compared to meet the objectives stated in Section 1.2. The following conclusions were drawn from this study:

1. Through the thermal characterization of the Li-ion cells the theoretical and experimental heat generation rates could be determined. The variation in the experimental heat generation rate was smaller than that of the theoretical heat transfer rate. The reason for this was most probably the fact that the theoretical heat generation rate uses the internal resistance of a Li-ion cells that are available in open literature (SONY-US18650 cells). It was observed that when computing the heat generation rate with the internal resistance values of Rust (2017), the values range from 1800 W/m^3

to 2100 W/m^3 during a charge cycle and from 2000 W/m^3 to 2500 W/m^3 during a discharge cycle (depending on the State of Charge (SOC)).

2. The developed analytical and numerical models of the aluminium plate BTMS showed good correlation with the experimental results. The effect of the low pressure wake left by the first fin was clear in all three solutions, as the average temperature of each fin increased downstream. This effect was also evident in the heat transfer rate of the fins, as the second and third fins dissipated less heat. The results of the velocity distribution along the cooling channel was used to improve the analytical model by providing a more accurate representation of the specific velocities over the fins. This resulted in more accurate heat transfer rates being calculated.

3. The results of experiment 1 supported the findings of the analytical and numerical solutions as the temperature of cell 1 was on average 0.6 °C colder than the other cells. It was noted that this is a very small value, however it does give an indication of the trend for a full scale installation where the differences will be much higher. It was also observed that the temperature of the first cell dropped significantly more when the cooling fan was switched on.

4. The temperature distribution of the Thermosyphon Heat Pipes (THPs) in the analytical model was less accurate than that of the previous BTMS. However the average heat transfer coefficient calculated from the results of the methods by Frass (2015) and Kröger (1998), resulted in a good correlation between the average fin temperatures of the analytical and numerical results.

5. The method of Chong et al. (2016), in which the THPs were modelled as solid superconductors for the CFD simulations, performed as expected. The method slightly under predicted the evaporator temperatures and over predicted the condenser temperatures by 4 % and 6 % respectively. This method also resulted in a good correlation between the heat transfer results in the fins attached to the condenser section.

6. The results of experiment 2 were very promising. There was a good uniformity in the cell temperatures, however the temperature of cell 1 was still lower than the rest of the cells. This however can be expected as the first row of THPs were exposed to colder, “cleaner” air. When consulting Table 7.4 it can be seen that the theoretical results did not predict an improvement in the temperature uniformity of the pack. A part of the reason for this is due to the increase of the air temperature as it is flowing through the finned condenser section. It could be seen in Figure 7.7 and 7.13 that the THP BTMS caused a higher increase in air temperature as a result of the better heat transfer. This affected the heat transfer downstream of the first THPs.

8.2 Recommendations

The recommendations for future research are presented below:

In order to better test the effects of the BTMS, it is recommended to test the system for a variety of ambient conditions. The experimental results of this thesis were limited to the ambient conditions at the time of testing. The use of a thermal chamber could aid in this recommendation, as it would allow the user to test at certain set temperatures. It could also speed up the pre-heating of the cells to reduce the testing time.

It is also recommended to use a variable load to discharge the cells as this would allow the cells to be discharged at different rates, therefore decreasing testing time and allowing more cells to be tested.

To increase the accuracy of the heat generation rate of the cells it is recommended to use heat flux sensors to correlate the heat generation rate, since the heat generation rate in this thesis was calculated using experimental values of the internal resistance in analytical formulas.

To improve the temperature uniformity of the cells it is recommended to alter the layout of the battery pack to allow the airflow to pass between the cells. This would eliminate the need for conduction materials and therefore decrease the overall weight of the battery pack. A possible way to do this would be to change the location of the inlets to the side of the battery pack and suck air between the cells into the channel and out.

8.3 Closing statement

The development of this improved BTMS is important to the growth of local expertise and furthering the awareness of the advances in battery cooling technology. This is essential for the implementation of locally developed EVs. This thesis concluded that the suggested THP BTMS illustrated an improvement in the heat transfer capability compared to that of the current system. It would therefore be worthwhile continuing this research.

9 References

ANSYS (2013a) *ANSYS Fluent Theory Guide*.

ANSYS (2013b) *ANSYS Fluent User ' s Guide*.

Arduino (2019) *Read Analog Voltage*. Available at: https://www.arduino.cc/en/Tutorial/ReadAnalogVoltage (Accessed: 29 October 2019).

Bayley, F. J. and Cohen, H. (1955) 'Heat Transfer Problems of Liquid Cooled Gas Turbine Blades', *Proc. Instn. Mech. Engrs.*, 169, pp. 1063–1080.

Brandt, F. (1985) 'Waermeuebertragung in Dampferzeugern und Waermeaustauschern', in *FDBR Fachbuchreihe*. Vulkan Verlag Essen.

Cengel, Y. A. and Cimbala, J. M. (2014) *Fluid Mechanics*. Third Edit. McGraw Hill.

Cengel, Y. A. and Ghajar, A. J. (2015) *Heat and Mass Transfer, Fundamentals & Application, Fifth Edition in SI Units*, *McGraw-Hill, 5th Edition*.

Chen, J. Q. *et al.* (2018) 'Experimental Investigation on Cooling / Heating Characteristics of Ultra - Thin Micro Heat Pipe for Electric Vehicle Battery Thermal Management', *Chinese Journal of Mechanical Engineering*. Springer Singapore. doi: 10.1186/s10033-018-0255-0.

Chen, K.-W. and Li, X.-G. (2014) 'Accurate determination of battery discharge characteristics—A comparison between two battery temperature control methods', *Journal of Power Sources*, (247), pp. 961–966.

Chen, M. M., Faghri, A. and Morgan, M. (1989) 'Heat Transfer in Two-Phase Closed Conventional and Concentric Thermosyphons', *ASME J. Heat Mass Transfer*, 111, pp. 611–618.

Chen, Y. and Evans, J. W. (1994) 'Thermal analysis of lithium polymer electrolyte batteries by a two dimensional model -Thermal behaviour and design optimization', *Electrochimica Acta*, 39, pp. 517–526.

Chong, A., Jouhara, H. and Ramos, J. (2016) 'Experimental and numerical investigation of a cross flow air-to-water heat pipe-based heat exchanger used in waste heat recovery', *International Journal of Heat and Mass Transfer*. Elsevier Ltd, 102, pp. 1267–1281. doi: 10.1016/j.ijheatmasstransfer.2016.06.100.

Delmas, C. *et al.* (2003) *Atomic resolution of lithium ions in LiCoO2*. vol. 2.

Desmet, B. *et al.* (2014) 'Experimental investigation on the feasibility of heat pipe cooling for HEV / EV lithium-ion battery', *Applied Thermal Engineering*. Elsevier Ltd, 63(2), pp. 551–558. doi: 10.1016/j.applthermaleng.2013.11.048.

Dhameja, S. (2002) *Electric Vehicle Battery Systems*. Newnes.

Dobson, R. T. and Meyer, A. (2006) 'Thermal Performance of R134a and Butane Charged Thermosyphons', 22(3), pp. 26–34.

Dunn, D. P. and Reay, D. (1994) *Heat Pipes*. 4th Ed. Pergamon.

Electro-Automatik (2012) 'BCI-800R User Manual'.

Engineering Toolbox (2019) *Methanol - Thermophysical Properties*. Available at: https://www.engineeringtoolbox.com/methanol-methyl-alcohol-properties-CH3OH-d_2031.html (Accessed: 28 October 2019).

Faghri, A. (1995) *Heat Pipe Science and Technology*. Taylor & Francis.

Faghri, A. and Harley, C. (1994) 'Complete Transient Two-Dimensional Analysis of Two-Phase Closed Thermosyphons including Falling Condensate Film', *ASME J. Heat Transfer*, 116, pp. 418–426.

Fan, L.-W., Khodadadi, J. M. and Pesaran, A. (2013) 'A parametric study on thermal management of an air-cooled lithium-ion battery module for plug-in hybrid electric vehicles', *Journal of Power Sources*, (238), pp. 301–312.

Frass, F. (2015) *Principles of Finned-Tube Heat Exchanger Design for Enhanced Heat Transfer*. 2nd edn. Vienna, Austria: WSEAS Press.

Ganesan, V. and Mills, A. F. (1999) *Heat Transfer*. 2nd Ed. Pearson.

Gorbis, Z. R. and Savchenkov, G. A. (1976) 'Low Temperature Two-Phase Closed Thermosyphon Investigation', in *2nd Int. Heat Pipe Conf.* Bologna, Italy, pp. 37–45.

Gross, U. and Kaminski, S. (2000) 'Luftseitiger Waermeuebergang und Druckverlust in Lamellenrohr Waermeuebertragern', *KI Luft- und Kaeltetechnik*, 1, p. 13.

He, R. and Xu, X. M. (2013) 'Research on the heat dissipation performance of battery pack based on forced air cooling', *Journal of Power Sources*, (240), pp. 33–41.

Horn, B. V. W. (2017) 'The Development of a 48V, 10kWh LiFePO4 Battery Management System for Low Voltage Battery Storage Applications', (March), p. 120.

Inui, Y. *et al.* (2007) 'Simulation of temperature distribution in cylindrical and prismatic lithium ion secondary batteries', *Energy Conversion and Management*, 48, pp. 2103–2109.

Karimi, G. and Li, X. (2013) 'Thermal management of lithium-ion batteries for electric vehicles', *International Journal of Energy Research*. John Wiley & Sons, Ltd, 37(1), pp. 13–24. doi: 10.1002/er.1956.

Kays, W. M. and Londen, A. L. (1984) *Compact Heat Exchangers*. 3rd Editio. New York: McGraw Hill.

Kröger, D. G. (1998) *Air-cooled Heat Exchangers and Cooling Towers*.

Larminie, J. and Lowry, J. (2003) *Electric Vehicle Technology Explained*.

Li, J. and Zhu, Z. (2014) 'Battery Thermal Management Systems of Electric Vehicles', p. 79. Available at: http://publications.lib.chalmers.se/records/fulltext/200046/200046.pdf.

Li, N., Ren, Y. and Wu, B. (2012) 'LiFePO4 Cathode Material', in *Electric Vehicles â€“ The Benefits and Barriers*. Beijing, p. 200. doi: 10.5772/18995.

Liou, W. W. *et al.* (1995) 'A New k-epsilon Eddy-Viscosity Model for High Reynolds Number Turbulent Flows - Model Development and Validatio', *Computers Fluids*, 24(3), pp. 227–238.

MakeItFrom.com (2019) *5754 Aluminum*. Available at: https://www.makeitfrom.com/material-properties/5754-AlMg3-3.3535-A95754-Aluminum (Accessed: 28 October 2019).

Matthe, R., Mettlach, H. and Turner, L. (2011) 'Voltec Battery System for Electric Vehicle with Extended Range', *SAE International Journal of Engines*, (JANUARY 2014), pp. 1944–1962. doi: 10.1016/B978-0-444-59513-3.00008-X.

McAdams, W. (1954) *Heat Transmission*. New York: McGraw Hill.

Menter, F. R. (1994) 'Two-Equation Eddy-Viscosity Turbulence Models for Engineering Applications', *AIAA Journal*, 32(8), pp. 1598–1605.

Mirkovics, Z. (1974) *Heat Transfer and Flow Resistance Correlation for Helically Finned and Staggered Tube Banks in Crossflow*. New York: McGraw Hill.

MIT Electric Vehicle Team (2008) 'A Guide to Understanding Battery Specifications', (December). Available at: http://web.mit.edu/evt/summary_battery_specifications.pdf.

Mohammadian, S. K. and Zhang, Y. (2017) 'Cumulative effects of using pin fin heat sink and porous metal foam on thermal management of lithium-ion batteries', *Applied Thermal Engineering*, 118, pp. 375–384. doi: 10.1016/j.applthermaleng.2017.02.121.

Panchal, S. (2016) 'Experimental Investigation and Modeling of Lithium-ion Battery Cells and Packs for Electric Vehicles', p. 171. Available at: https://ir.library.dc-uoit.ca/bitstream/10155/747/1/Panchal_Satyam.pdf.

Pioro, L. S. and Pioro, I. L. (1997) *Indusrial Two-phase Thermosyphons*. Begell House.

Rao, Z. *et al.* (2013) 'Experimental investigation on thermal management of electric vehicle battery with heat pipe', *Energy Conversion and Management*. Elsevier Ltd, 65, pp. 92–97. doi: 10.1016/j.enconman.2012.08.014.

Reed, J., Gerner, F. and Tien, C. (1987) 'Transient Condensation of a Laminar

Film onto a Vertical Plate', in *AIAA 22nd Thermophysics Conf.* Honolulu, Hawaii.

Rohsenow, W. M. (1952) 'A method of correlating heat-transfer data for surface boiling of liquids', *Trans. ASME*, 74, pp. 969–976.

Russwurm, A. E. (1980) 'Q-pipes add a new dimension to waste heat recovery, Part 1', *Refrigiration and Airconditioning*, pp. 27–39.

Rust, N. (2017) *Capacity and impedance study of 85Ah LiFePO4 cells at various temperatures*. Port Elizabeth.

Schmidt, E. (1963) 'Der Waermeuebergang an Rippenrohre und die Berechnung von Rohrbuendelwaermeaustauschern', *Kaeltetechnik 15*, p. 88.

Skrinska, A. and Stasiulevicius, J. (1988) *Heat Transfer of Finned Tube Bundles in Crossflow*. Washington New York Londen: Hemisphere Publ. Corp.

Van der Spuy, S. J. and Von Backström, T. W. (2009) 'Performance of low noise fans in power plant air cooled steam condensers', (August 2014). doi: 10.3397/1.3151851.

Strel'tsov, A. I. (1975) 'Theoretical and Experimental Investigation of Optimum Filling for Heat Pipes', *Heat Transfer-Soviet Research*, 7(1), pp. 23–27.

SUNONWEALTH (2008) 'EEC0382B1-0000-A99 Series'.

Wang, F., Wang, S. and Zhang, J. (2012) 'Investigation on flow and heat transfer characteristics in rectangular channel with drop-shaped pin fins', *Propulsion and Power Research*. Elsevier, 1(1), pp. 64–70. doi: 10.1016/j.jppr.2012.10.003.

Zhu, J. (2014) *Synthesis, Characterization and Performance of Cathodes for Lithium Ion Batteries*.

Van Zuydam, A. (2018) 'Evaluating the Cooling of an Electric Vehicle Battery Pack'.

Appendix A: Two dimensional analysis of THPs

Faghri and Harley (1994) developed a two dimensional steady/transient thermosyphon model which accounts for the falling liquid film and conjugate heat transfer through the wall. This model simulates the entire thermosyphon, unlike other models that only simulate the condenser section. It is important to note that the effects of gravity cannot be neglected, as gravity is required to return the condensate to the evaporator section. However the vapour velocity is often large enough to neglect free convection. Figure A.1 shows the coordinate system and labelling convention of this analysis. The cylindrical coordinates are notated by z in the axial direction and r in the radial direction. Upon conversion to a two dimensional system the axial and radial coordinates are changes to x and y respectively.

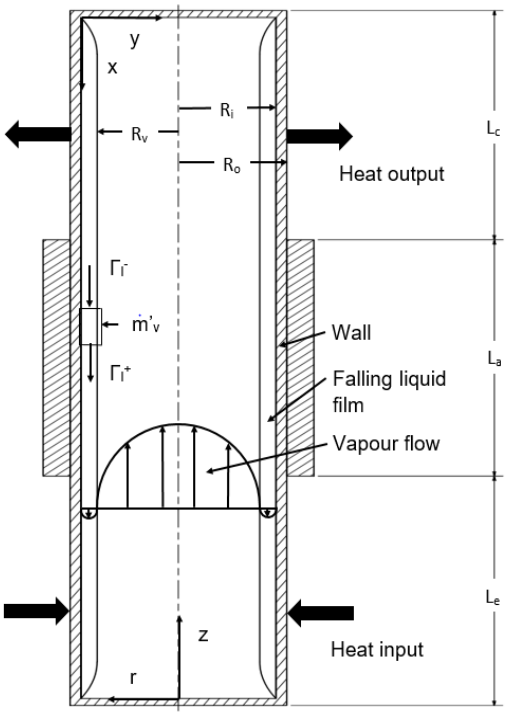

Figure A.1: The configuration and coordinate system of the thermosyphon

According to Faghri and Harley (1994) the differential equations in cylindrical coordinates for transient, laminar, compressible flow in the vapour channel of a two phase thermosyphon, assuming constant viscosity is expressed as follows.

Mass:

$$\frac{\partial \rho}{\partial t} + \nabla \cdot \left(\rho \vec{V}\right) = 0 \tag{A.1}$$

Momentum:

$$\rho \frac{D\vec{V}_v}{Dt} = -\nabla p + \frac{1}{3}\mu \nabla\left(\nabla \cdot \vec{V}_v\right) + \mu \nabla^2 \vec{V}_v + \rho \vec{g} \tag{A.2}$$

Energy:

$$\rho c_p \frac{DT_v}{Dt} - \nabla \cdot k \nabla T_v - \frac{Dp}{Dt} - \mu \Phi = 0 \tag{A.3}$$

With the equation of state given by:

$$p = \rho_v R_g T_v \tag{A.4}$$

where R_g refers to the gas constant. The conservation of energy equation of the pipe wall can be expressed as:

$$\rho_w c_{pw} \frac{\partial T}{\partial t} = k_w \left[\frac{1}{r}\frac{\partial}{\partial r}\left(r \frac{\partial T}{\partial r}\right) + \frac{\partial^2 T}{\partial z^2}\right] \tag{A.5}$$

where c_{pw} and ρ_w are the specific heat and density of the thermosyphon pipe wall respectively. The transient, laminar, incompressible liquid flow two dimensional conservation equations for the falling condensate film are expressed as follows.

Mass:

$$\frac{1}{r}\frac{\partial}{\partial r}(r v_l) + \frac{\partial w_l}{\partial z} = 0 \tag{A.6}$$

Radial momentum:

$$\rho_l \left(\frac{\partial v_l}{\partial t} + v_l \frac{\partial v_l}{\partial r} + w_l \frac{\partial v_l}{\partial z}\right) = -\frac{\partial p_l}{\partial r} + \mu_l \left[\frac{1}{r}\frac{\partial}{\partial r}\left(r \frac{\partial v_l}{\partial r}\right) - \frac{v_l}{r^2} + \frac{\partial^2 v_l}{\partial z^2}\right] \tag{A.7}$$

Axial momentum:

$$\rho_l \left(\frac{\partial w_l}{\partial t} + v_l \frac{\partial w_l}{\partial r} + w_l \frac{\partial w_l}{\partial z}\right) = -\frac{\partial p_l}{\partial z} + \mu_l \left[\frac{1}{r}\frac{\partial}{\partial r}\left(r \frac{\partial w_l}{\partial r}\right) + \frac{\partial^2 w_l}{\partial z^2}\right] + g\rho_l \tag{A.8}$$

Energy:

$$\rho_l c_{pl} \frac{\partial T_l}{\partial t} + v_l \frac{\partial T_l}{\partial r} + w_l \frac{\partial T_l}{\partial z} = \frac{1}{r}\frac{\partial}{\partial r}\left(r k_l \frac{\partial T_l}{\partial r}\right) + \frac{\partial}{\partial z}\left(k_l \frac{\partial T_l}{\partial z}\right) \quad \text{(A.9)}$$

where w_l and v_l are the axial and radial liquid velocity respectively, and g represents the gravitational acceleration, assumed to be negative in the z-direction for a vertical thermosyphon.

It is, however, not obligatory to solve these complex system of equations. Reed et al. (1987) determined the importance of modelling the transient effects by using the simplified version of the boundary layer equations to examine the transient vapour condensation onto a flat plate. It was concluded that when the Jakob-Prandtl number and the Jakob number ratio are both in the order of one, that the film thickness of the falling liquid film predicted by the quasi-steady analysis will be close to that predicted by the actual transient analysis. Therefor the model developed by Faghri and Harley (1994) uses a quasi-steady Nusselt type solution for the falling liquid film. The assumptions of the analysis are:

1. The vapour condensation is filmwise.
2. Liquid subcooling, inertia and convection effects in the liquid are negligible.
3. The liquid film thickness is very small compared to the vapour space radius.
4. The vapour density is very small compared to the liquid density.
5. The circumferential temperature and velocity gradients are negligible.

Based on these assumptions and through coordinate transformation the liquid film equations simplify to:

$$\frac{\partial^2 w_l}{\partial y^2} = \frac{1}{\mu_l}\frac{dp_l}{dx} - \frac{\rho_l g}{\mu_l} \quad \text{(A.10)}$$

and

$$\frac{\partial^2 T_l}{\partial y^2} = 0 \quad \text{(A.11)}$$

Where x represents the distance from the condenser section end cap and y is the distance from the pipe wall. At the liquid-wall interface $(y = 0)$ a no slip condition is assumed.

$$w_l = 0 \quad \text{(A.12)}$$

At the liquid vapour interface $(y = \delta)$, the vapour shear stress is equal to that of the liquid.

$$\mu_l \frac{\partial w_l}{\partial y} = -\mu_v \frac{\partial w_v}{\partial r} \tag{A.13}$$

With a boundary layer assumption on the radial liquid pressure gradient, Equation A.10 can further be simplified. By assuming a constant liquid pressure across the film, the axial-direction pressure gradient in the liquid can be approximated by:

$$\frac{dp_l}{dx} = -\frac{dp_v}{dz} \tag{A.14}$$

By utilizing these assumptions and using equations A.12 and A.13 to integrate Equation A.10 twice with respect to y yields:

$$w_l(y) = \left(g\rho_l + \frac{dp_v}{dz}\right)\frac{\delta^2}{\mu_l}\left[\frac{y}{\delta} - \frac{1}{2}\left(\frac{y}{\delta}\right)^2\right] + \frac{\mu_v y}{\mu_l}\frac{\partial w_v}{\partial r}\bigg|_{r=Rv} \tag{A.15}$$

The axial liquid mass flow rate per unit width is defined as.

$$\Gamma_l = \int_0^{\delta} \rho_l w_l(y) dy \tag{A.16}$$

By multiplying the inner circumference of the thermosyphon with equation A.16 will yield the total liquid mass flow rate. Substituting equation A.15 into equation A.16 yields the liquid mass flow rate per unit width as

$$\Gamma_l = \left(g\rho_l + \frac{dp_v}{dz}\right)\frac{\rho_l \delta^3}{3\mu_l} + \frac{\rho_l \mu_v \delta^2}{2\mu_l}\frac{\partial w_v}{\partial r}\bigg|_{r=Rv} \tag{A.17}$$

From the conservation of mass it is assumed that mass will enter a fixed control volume by both condensation and evaporation of the liquid and vapour flow at any axial position in the thermosyphon. This mass conservation equation can be expressed as:

$$\Gamma_l^{+} - \Gamma_l^{-} = \frac{d\Gamma_l}{dx} dx = \dot{m}_{v'} \tag{A.18}$$

where $\dot{m}_{v'}$ is the vapour condensation/evaporation rate over the control volume, the superscripts (+) and (-) indicate the conditions at the entrance and exit of the control volume respectively. The mass flow rate is related to the vapour condensation/evaporation rate through:

$$\dot{m}_{v'} = \rho_\delta v_\delta dx \tag{A.19}$$

where v_δ refers to the interfacial radial vapour velocity through the control volume. Combining equations A.18 and A.19 gives:

$$\Gamma_l = \int_0^x \rho_\delta v_\delta dx = \int_z^{L_t} \rho_\delta v_\delta dz \tag{A.20}$$

From equations A.17 and A.20

$$\left(g\rho_l + \frac{dp_v}{dz}\right)\frac{\rho_l \delta^3}{3\mu_l} + \frac{\rho_l \mu_v \delta^2}{2\mu_l}\frac{\partial w_v}{\partial r}\bigg|_{r=Rv} \delta^2 = \int_z^{L_t} \rho_\delta v_\delta dz \tag{A.21}$$

The film thickness at the condenser section end cap is assumed to be zero.

$$\delta|_{x=0} = 0 \tag{A.22}$$

If the vapour pressure drop and interfacial shear stress are ignored, the closed form expression of the film thickness is:

$$\delta = \left[\left(\int_z^{L_t} \rho_\delta v_\delta dz\right)\frac{3\mu_l}{g\rho_l}\right]^{1/3} \tag{A.23}$$

Solving equation A.11 results in a linear temperature profile across the liquid film. The latent heat of the condensing vapour is assumed to be removed only by the heat transfer via conduction through the liquid. This falling film analysis by Faghri and Harley (1994) however, is only valid when operating with the critical liquid fill ratio. This ratio is defined as the amount of liquid that results in a zero film thickness at the end caps of the thermosyphon i.e. $(z = 0,\ z = L_t)$. Therefore this analysis neglects the possibility of a liquid pool forming in the bottom of the evaporator section and assumes that condensation and evaporation only transpires from the surface of the condensate film. The no slip and adiabatic conditions for velocity and temperature are also applied to the end caps of the thermosyphon. Due to the formulation used for the film the film thickness at the evaporator end cap cannot be specified, however when the condensation and evaporation rates in the thermosyphon reach steady state the film thickness will be zero.

$$z = 0: \quad v_v = w_v = \frac{\partial T}{\partial z} = 0 \tag{A.24}$$

$$z = L_t: \quad v_v = w_v = \delta = \frac{\partial T}{\partial z} = 0 \tag{A.25}$$

At the centreline $(r = 0)$ the radial gradients of the temperature and axial velocity and the radial vapour velocity are zero.

$$v_v = \frac{\partial w_v}{\partial r} = \frac{\partial T}{\partial r} = 0 \tag{A.26}$$

To ensure that the conditions at the liquid vapour interface in the evaporator are saturated, the Clausius-Clapeyron equation is utilised to calculate the temperature at the interface.

$$T_{sat} = \left(\frac{1}{T_0} - \frac{R_g}{h_{fg}} ln \frac{p_v}{p_0}\right)^{-1} \tag{A.27}$$

The radial velocity at the interface is calculated through determining the evaporation rate at which the heat transfer requirements will be satisfied.

$$v_\delta = \frac{\left(k_l \frac{T_\delta - T_w}{\delta} - k_v \frac{\partial T_v}{\partial r}\right)}{\left[h_{fg} + (c_{pv} - c_{pl})T_\delta\right]\rho_v} \tag{A.28}$$

Due to the no slip condition, the velocity of the vapour and condensate must be equal at the liquid vapour interface. The mechanical force balance must also be satisfied.

$$w_v = w_l(\delta)$$

$$\tau_l = -\tau_v(\delta) = -\mu_v \left.\frac{\partial w_v}{\partial r}\right|_{r=Rv} \tag{A.29}$$

To simulate the condensation process in the condenser section a heat source is applied to the wall at the liquid vapour interface. The liquid temperature is set equal to the vapour temperature to account for temperature continuity.

$$q_s = \left[h_{fg} + (c_{pv} - c_{pl})T_\delta\right]\rho_v v_\delta \tag{A.30}$$

The heat flux at the liquid wall interface must satisfy the conservation of energy.

$$k_w \frac{\partial T}{\partial r} = -\frac{k_l}{\delta}(T_\delta - T_w) \tag{A.31}$$

Appendix B: Properties and specifications

This Appendix presents the specifications of the Lithium-ion cells and the cooling fan. As well as the properties of air, aluminium, copper and methanol.

B.1 Lithium –ion cell specifications

The specifications of the cells are summarized in Table B.1.

Table B.1: Specifications of the Li-ion cells

Cell parameter	Value [Units]
Cell dimensions	Height: 0,128 m Length: 0,175 m Width: 0,049 m
Nominal capacity	75 Ah
Nominal voltage	3,2 V
Charging cut-off voltage	3,8±0,05 V
Discharging cut-off voltage	2,5±0,05 V
Weight	2 kg

B.2 Fan specifications

The fan used for this thesis was a 24 V, 138 CFM Sunon fan. The fan was installed at the end of the cooling channel to supply air to the BTMSs. The specifications of the fan are presented in Table B.2 and the fan dimensions are shown in Figure B.1.

Table B.2: Fan performance characteristics (SUNONWEALTH, 2008)

Fan parameter	Value [Units]
Rated speed	3100 rpm
Air flow	138 CFM
Static pressure	0,36 Inch-H_2O
Acoustic noise	48 dB(A)

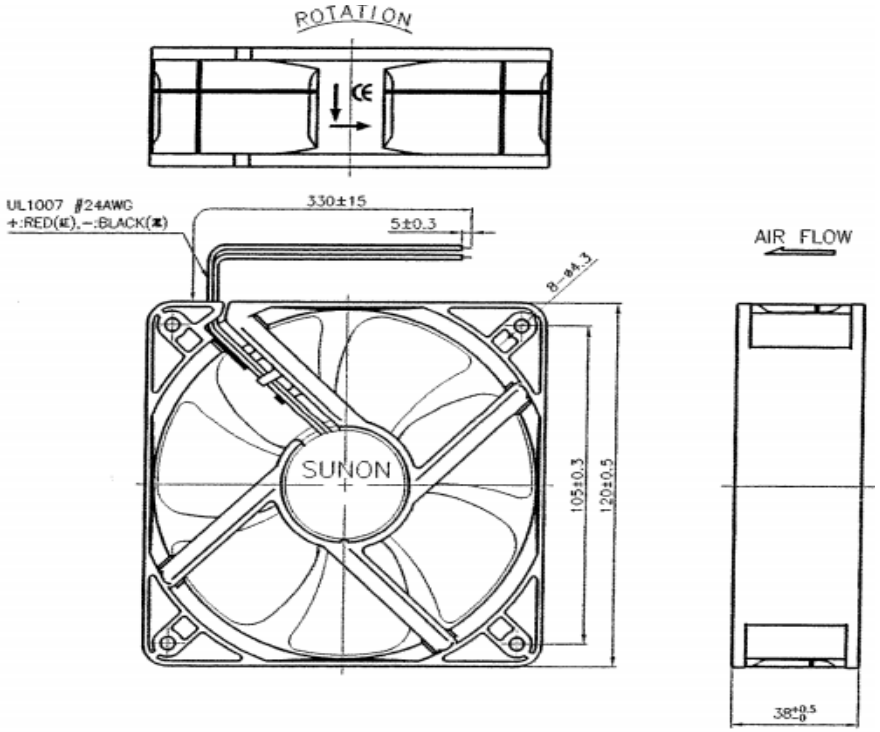

Figure B.1: Dimensions of the cooling fan (SUNONWEALTH, 2008)

The fan curve in terms of axial velocity is shown in Figure B.2. The pressure drop curves of the two BTMSs is also plotted to indicate the operating points. As mentioned in Section 5.1.3 the fan pressure was converted to a static-to-static pressure in order to find the operating points.

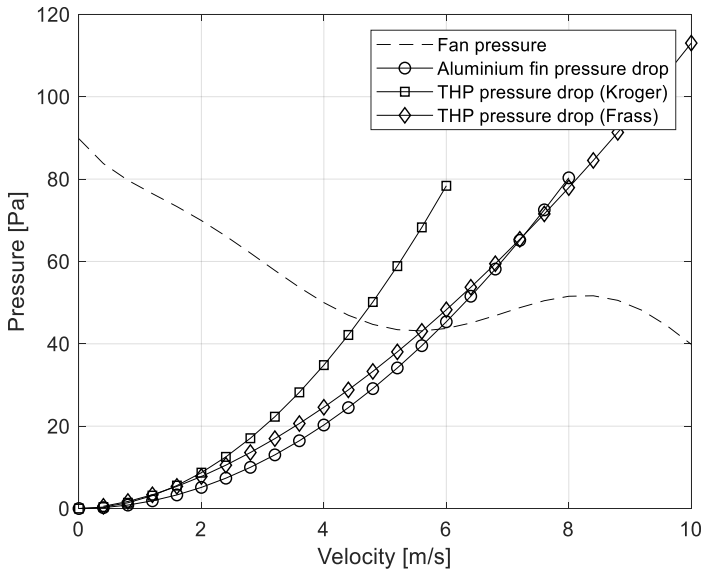

Figure B.2: Fan pressure curve

B.3 Fluid properties

The properties of air at the average ambient temperature, 25 °C is summarized in Table B.3.

Table B.3: Properties of air at 25 °C (Cengel and Cimbala, 2014)

Parameter	Value [Units]
Density	1,184 kg/m^3
Specific heat	1007 J/kg K
Thermal conductivity	0,02551 W/m K
Dynamic viscosity	1,849 x 10^{-5} kg/m s
Kinematic viscosity	1,562 x 10^{-5} m^2/s
Prandtl number	0,7296

The properties of the working fluid, methanol, is summarised in Table B.4.

Table B.4: Properties of methanol (Engineering Toolbox, 2019)

Parameter	Value [Units]
Density gas	0,22 kg/m^3
Density liquid	786,3 kg/m^3
Specific heat gas	3,62 kJ/kg K
Specific heat liquid	2,53 kJ/kg K
Thermal conductivity	0,202 W/m K
Dynamic viscosity	0,544 cP
Kinematic viscosity	0,692 cSt
Gas constant	259,5 J/kg K

B.4 Material properties

The aluminium plates are manufactured from Aluminium 5754, the properties of this material is shown in Table B.5.

Table B.5: Properties of Aluminium 5745 (MakeItFrom.com, 2019)

Parameter	Value [Units]
Density	2660 kg/m^3
Specific heat	900 J/kg K
Thermal conductivity	130 W/m K

The THPs were manufactured from copper and modelled as superconductors in Chapter 5. The material properties of copper and the superconductor material (THP) is shown in Table B.6.

Table B.6: Properties of copper and the superconductor material (Cengel and Ghajar, 2015)

Parameter	Copper [Units]	THP [Units]
Density	8933 kg/m^3	3316,616 kg/m^3
Specific heat	385 J/kg K	385 J/kg K
Thermal conductivity	401 W/m K	3032,9 W/m K

Appendix C: Sample calculations

The sample calculations for this thesis are presented in this Appendix. All calculation use the properties defined in Appendix B.

C.1 Heat generation

Consider the cell to be charging, and be at a State of Charge (SOC) of 50 % and 25 °C. Using the parameters of the cell given in Table B.1.

The internal resistance will then be:

$$R_i = 2.258 \times 10^{-6} SOC^{-0.3952}$$
$$R_i = 2.9696 \times 10^{-6}\ \Omega\ m^3$$
$$R_i = 2.7055\ m\Omega$$

and the change of entropy of the cell is:

$$\Delta S = 99.88\ SOC - 76.67$$
$$\Delta S = -26.73\ kJ/kmol\ K$$

If the charge current is 25 A, the corresponding heat generation rate is:

$$q = R_i i^2 - iT\frac{\Delta S}{F}$$
$$q = 2.9696 \times 10^{-6} \times \left(\frac{25}{(0.128 \times 0.175 \times 0.049)}\right)^2 - 25 \times 25 \times \frac{-26.73}{96485}$$
$$q = 1540\ W/m^3$$

C.2 Aluminium plate BTMS calculations

Using the properties of the cooling channel and aluminium fins given in Table 3.1 and 3.2, the hydraulic diameter of the rectangular cooling channel can be calculated as:

$$D_h = \frac{4V_f}{A_w}$$
$$D_h = \frac{4 \times (1 \times 0.111 \times 0.128 - 3 \times 0.002 \times 0.043 \times 0.045)}{2 \times 1 \times (0.111 \times 0.128) + 3 \times \left((0.043 + 0.002) \times 2 \times 0.045 - 2 \times 0.002 \times 0.043\right)}$$
$$D_h = 0.1154\ m$$

The corresponding Reynolds number is:

$$Re_{Dh} = \frac{v_{max} D_h}{\upsilon}$$
$$Re_{Dh} = \frac{5.9 \times 0.1154}{1.516 \times 10^{-5}}$$
$$Re_{Dh} = 44912$$

The Nusslet number can then be calculated as:

$$Nu = 0.015 \times {Re_{Dh}}^{0.816}$$
$$Nu = 93.84$$

The convective heat transfer coefficient is therefore:

$$h_{conv} = \frac{Nu\ k}{L_c}$$
$$h_{conv} = \frac{93.84 \times\ 0.02514}{0.046}$$
$$h_{conv} = 51.2893\ W/m^2\ K$$

The temperature halfway down the fin is therefore:

$$m = \sqrt{\frac{2\ h_{conv}}{k\ t}}$$
$$m = 1424$$

$$\frac{T(x) - T_\infty}{T_b - T_\infty} = \frac{\cosh m(L-x) + \left(\frac{h_{conv}}{m \cdot k}\right) \sinh m(L-x)}{\cosh mL + \left(\frac{h_{conv}}{mk}\right) \sinh mL}$$
$$\frac{T(x) - 21.5}{26 - 21.5}$$
$$= \frac{\cosh 1424 \times (0.0225) + \left(\frac{51}{1424 \times 0.02514}\right) \sinh 1424 \times (0.0225)}{\cosh 1424 \times 0.045 + \left(\frac{51}{1424 \times 0.02514}\right) \sinh 1424 \times 0.045}$$
$$T(x) = 23.219\ °C$$

The pressure drop at a velocity of 5.9 m/s is:

$$\Delta P = N C_D \left(\frac{\rho\ v^2}{2}\right) + 4f \frac{L}{D_h} \frac{\rho v^2}{2}$$
$$\Delta P = 3 \times 1.96 \times \left(\frac{1.204 \times\ 5.9^2}{2}\right) + 4 \times 0.0039 \times \frac{1}{0.1183} \frac{1.204 \times 5.9^2}{2}$$

$$\Delta P = 43.86\ Pa$$

C.3 THP BTMS calculations

The sample calculations for the THP are shown below.

Convective heat transfer coefficient and pressure drop according to Frass

The effective heating surface is:

$$A_{Ftot} = 2\left[S_T S_L - a(b-a) - \frac{\pi a^2}{4}\right] + [2(b-a) + a\pi](t_R - s_R)$$
$$A_{Ftot} = 0.004\ m^2$$

The hydraulic diameter is calculated as:

$$D_h = \frac{4\left[(t_R - s_R)\left(S_T\, S_L - \left(a(b-a)\right) - a^2\frac{\pi}{4}\right)\right]}{A_{Ftot}}$$
$$D_h = \frac{4\left[(0.005)\left(0.038 \times 0.049 - \left(0.002(0.009)\right) - 0.002^2\frac{\pi}{4}\right)\right]}{0.004}$$
$$D_h = 0.0096\ m$$

The free cross sectioned area is:

$$A_f = \left(\frac{S_T - a}{S_T}\right)\left(\frac{t_R - s_R}{t_R}\right)$$
$$A_f = 0.8493\ m^2$$

The velocity in the narrowest cross section is:

$$v_{ncs} = \frac{v_0}{A_f}$$
$$v_{ncs} = \frac{5.1}{0.8493}$$
$$v_{ncs} = 6.5938\ m/s$$

This corresponds to a Reynolds number of:

$$Re_{Dh} = \frac{v_{ncs} D_h}{\upsilon}$$
$$Re_{Dh} = \frac{6.5 \times 0.0096}{1.516 \times 10^{-5}}$$
$$Re_{Dh} = 4190$$

The Nusselt number is therefore:

$$Nu = 0.0842\ {Re_{Dh}}^{0.7}\ Pr^{1/3}\left(\frac{D_h}{S_L}\right)^{1/3}$$
$$Nu = 0.0842 \times 4190^{0.7} \times 0.7309^{1/3}\left(\frac{0.0096}{0.049}\right)^{1/3}$$
$$Nu = 14.938$$

Using the outside diameter of the THP as the critical length the convective heat transfer coefficient is:

$$h_{conv} = \frac{Nu\ k}{L_c}$$
$$h_{conv} = \frac{14.938\ \times 0.02514}{0.006}$$
$$h_{conv} = 62.5937\ W/m^2\ K$$

At a velocity of 5.6 m/s the pressure drop is:

$$\xi = 0.7\ {Re_{Dh}}^{-0.339}\ \left(\frac{D_h}{S_L}\right)^{0.6}$$
$$\xi = 0.7 \times 4190^{-0.339} \times \left(\frac{0.0096}{0.049}\right)^{0.6}$$
$$\xi = 0.0074$$

$$\Delta P = N\xi\rho\frac{{v_{ncs}}^2}{2} + 4f\frac{L}{D_h}\frac{\rho v^2}{2}$$
$$\Delta P = 3 \times 0.0074 \times 1.204 \times \frac{5.6^2}{2} + 4 \times 0.0039 \times \frac{1}{0.1183}\frac{1.204 \times 5.6^2}{2}$$
$$\Delta P = 43.03\ Pa$$

Convective heat transfer coefficient and pressure drop according to Kröger

The minimum free flow area through the control volume is:

$$A_{cvc} = (S_T - b)(s_R - t_R)$$
$$A_{cvc} = (0.038 - 0.011)(0.005)$$
$$A_{cvc} = 1.125 \times 10^{-4}\ m^2$$

The corresponding frontal area is:

$$A_{cvfr} = t_R s_R$$
$$A_{cvfr} = 0.0002$$

Using these values the area ratio can be defined as:

$$\sigma_a = \frac{A_{cvc}}{A_{cvfr}}$$
$$\sigma_a = 0.5383$$

The fin surface area in contact with the air stream is:

$$A_{cvf} = 2\left[t_R s_R - a(b-a) - \frac{\pi a^2}{4}\right]$$
$$A_{cvf} = 2\left[0.0055 \times 0.0005 - 0.002 \times (0.009) - \frac{\pi \times 0.002^2}{4}\right]$$
$$A_{cvf} = 0.0038\, m^2$$

The total area in contact with the air stream flowing through the control volume:

$$A_{cva} = A_{cvc} + (t_R - s_R)[2(b-a) + \pi a]$$
$$A_{cva} = 1.125 \times 10^{-4} + (0.005)[2(0.009) + \pi 0.002]$$
$$A_{cva} = 0.0039\, m^2$$

The hydraulic diameter is then calculated to be:

$$D_h = \frac{4A_{cvc}S_L}{A_{cva}}$$
$$D_h = \frac{4 \times 1.125 \times 10^{-4} \times 0.049}{0.0039}$$
$$D_h = 0.0059$$

The air mass velocity flowing through the minimum free flow area of the control volume is:

$$G_{acv} = \frac{\dot{m}_a}{A_{fr}\sigma_a}$$
$$G_{acv} = 10.2891\ kg\ m/s$$

The corresponding Reynolds number is:

$$Re = \frac{G_{acv}D_h}{\mu}$$
$$Re = \frac{10.2891 \times 0.0059}{1.825 \times 10^{-5}}$$
$$Re = 3306$$

Using this Reynolds number the Colburn j-factor is:

$$j = StPr^{0.67} = 0.007 = \frac{h_{conv}Pr^{0.67}}{G_{acv}c_p}$$

This yields the following convective heat transfer coefficient:

$$h_{conv} = \frac{0.007\, G_{acv} c_p}{Pr^{0.67}}$$
$$h_{conv} = 89.3948\, W/m^2\, K$$

For a velocity of 4.6 m/s the pressure drop is:

$$\Delta P = \frac{{G_{acv}}^2}{2}\left[\frac{4Nf}{\rho_m}\left(\frac{A_{cva}}{A_{cvc}}\right) + (1+{\sigma_a}^2)\left(\frac{1}{\rho_o} - \frac{1}{\rho_i}\right)\right] + 4f\frac{L}{D_h}\frac{\rho v^2}{2}$$
$$\Delta P = \frac{10.29^2}{2}\left[\frac{4\times 3\times 0.0275}{1.1738}\left(\frac{0.0039}{1.125\times 10^{-4}}\right) + (1+0.54^2)\left(\frac{1}{1.145} - \frac{1}{1.204}\right)\right] + 4\times 0.0039\times\frac{1}{0.1183}\frac{1.204\times 4.6^2}{2}$$
$$\Delta P = 46.0652\, Pa$$

Temperature distribution in the THP

An iterative process is used to solve the temperature distribution of the THP. Initial temperatures are guessed for the evaporator and condenser walls to determine the saturation temperature of the working fluid:

$$T_{sat} = \frac{T_{w,e}L_e + T_{w,c}L_c}{L_e + L_c}$$
$$T_{sat} = \frac{26\times 0.175 + 22\times 0.052}{0.175 + 0.052}$$
$$T_{sat} = 24.8546\,°C$$

These temperatures are replace after the first iteration in order to determine a more accurate solution. The average convective heat transfer equation for the inside of the condenser section is:

$$\bar{h}_c = \frac{4}{3}\left[\frac{{\rho_l}^2 {k_l}^3 g h_{fg}}{4\mu_l(T_{sat} - T_{w,c})L_c}\right]^{1/4}$$
$$\bar{h}_c = \frac{4}{3}\left[\frac{786.3^2\times 0.202^3\times 9.81\sin 5\times 1165}{4\times 5.44\times 10^{-5}\times(24.85-22)\times 0.052}\right]^{1/4}$$
$$\bar{h}_c = 237.948\, W/m^2\, K$$

The heat transfer coefficient for the evaporator section is coincidentally the same. For a steady state solution the energy balance on the different control volume specified in Figure 4.3 is:

The first control volume in the evaporator section

$$k_{cu}A_c\frac{T_{m+1} - T_m}{\Delta x} + \bar{h}_e A_i(T_{sat} - T_m) + qA_{THP} = 0$$

The middle control volumes in the evaporator section

$$k_{cu}A_c\frac{T_{m+1}-T_m}{\Delta x}+k_{cu}A_c\frac{T_{m-1}-T_m}{\Delta x}+\bar{h}_eA_i(T_{sat}-T_m)+qA_{THP}=0$$

The middle control volumes in the condenser section

$$k_{cu}A_c\frac{T_{m+1}-T_m}{\Delta x}+k_{cu}A_c\frac{T_{m-1}-T_m}{\Delta x}+\bar{h}_cA_i(T_{sat}-T_m)+h_{conv}A_o(T_\infty-T_m)=0$$

The last control volume in the condenser section

$$k_{cu}A_c\frac{T_{m-1}-T_m}{\Delta x}+\bar{h}_cA_i(T_{sat}-T_m)+h_{conv}A_o(T_\infty-T_m)=0$$

To solve the temperatures at each node, the following matrices were developed:

$$MAT_A=\begin{bmatrix}A & B & 0 & \cdots & 0 & 0 & 0\\ B & D & B & & 0 & 0 & 0\\ & \vdots & & \ddots & & \vdots & \\ 0 & 0 & 0 & & B & E & B\\ 0 & 0 & 0 & \cdots & 0 & B & G\end{bmatrix}$$

$$MAT_B=\begin{bmatrix}C\\ \vdots\\ C\\ F\\ \vdots\\ F\end{bmatrix}$$

where:

$$A=\bar{h}_eA_i+\frac{k_{cu}A_c}{\Delta x}$$
$$B=-\frac{k_{cu}A_c}{\Delta x}$$
$$C=\left(T_{sat}\bar{h}_eA_i\right)+(qA_{THP})$$
$$D=\left(\bar{h}_eA_i\right)+\left(2\frac{k_{cu}A_c}{\Delta x}\right)$$
$$E=(h_{conv}A_o)+\left(\bar{h}_cA_i\right)+\left(2\frac{k_{cu}A_c}{\Delta x}\right)$$
$$F=\left(T_{sat}\bar{h}_cA_i\right)+(T_\infty h_{conv}A_o)$$
$$G=(h_{conv}A_o)+\left(\bar{h}_cA_i\right)+\left(\frac{k_{cu}A_c}{\Delta x}\right)$$

To solve the temperatures at each node:

$$MAT_T=MAT_A{}^{-1}MAT_B$$

Thermal conductivity of the solid superconductor material

To calculate the thermal conductivity of the superconductor we must first find the total resistance:

$$R_t = R_{h,e} + R_{k,e} + R_b + R_{in} + R_{cd} + R_{k,c} + R_{h,c}$$

where:

$$R_{h,c} = \frac{1}{h_{h,c}A_{h,c}}, R_{k,c} = \frac{\ln(d_o/d_i)}{2\pi k L_e}, R_{cd} = \frac{1}{h_{ei}A_{ei}}$$
$$R_{h,e} = \frac{1}{h_{h,e}A_{h,e}}, R_{ke} = \frac{\ln(d_o/d_i)}{2\pi k L_e}, R_b = \frac{1}{h_{ei}A_{ei}}$$
$$R_{in} = \frac{8R_g\mu_v {T_v}^2}{\pi {h_{fg}}^2 P_v \rho_v}\left(\frac{(L_e + L_c)/2 + L_a}{{r_i}^4}\right)$$

Therefore:

$$R_t = 66.1786\ °C/W$$

$$k_{THP} = \frac{L}{R_t A_c}$$
$$k_{THP} = \frac{0.227}{66.1786 \times 1.131 \times 10^{-6}}$$
$$k_{THP} = 3032.9\ W/m\ K$$

Heat flux for CFD

The heat generated by each cell is:

$$Q_{gen} = 2400\ W/m^3$$

The heat flux was then calculated, from an energy balance, as follows:

$$q_{CFD} = \frac{2Q_{gen}V_c}{A_{input}}$$
$$q_{CFD} = \frac{2 \times 2400 \times 0.175 \times 0.128 \times 0.049}{0.175 \times 0.011 \times 6}$$
$$q_{CFD} = 456\ W/m^2$$

C.4 Electrical calculations

The target discharge rate was 0.4 C. The cells have a nominal voltage of 3.2 V and a capacity of 75 Ah. Therefore the target current is:

$$I = 0.4 \times 75 = 30\ A$$

and through each of the resistor banks is:

$$I = \frac{30}{2} = 15\ A$$

The nominal voltage is:

$$V_{nom} = 4 \times 3.2 = 12.8\ V$$

Therefore the total resistance of the resistor bank has to be:

$$R = \frac{V}{I}$$
$$R = \frac{12.8}{15}$$
$$R = 0.8\ \Omega$$

However the maximum power would then be:

$$P = V_{max} I^2$$
$$P = 14 \times 15^2$$
$$P = 3150\ W$$

It was then determined iteratively that thirteen 10 Ω 20 W resistors in parallel would suffice. As the maximum power through each would be:

$$P = 14 \times \left(\frac{15}{13}\right)^2$$
$$P = 18.64\ W$$

However, the discharge current will be slightly less since the total resistance is:

$$\frac{1}{R_t} = \sum_{x=1}^{13} \frac{1}{R} + R_{cable}$$
$$R_t = 0.77 + 1.72 \times 10^{-8} \times 10$$
$$R_t = 0.77$$

The discharge current through one resistor bank is therefore:

$$I = \frac{V_{nom}}{R_t}$$
$$I = 16.6\ A$$

The total discharge current is:

$$I = 16.6 \times 2 = 33.2\ A$$

The discharge rate is:

$$C = \frac{33.2}{75} = 0.44$$

Appendix D: Experimental setup

This appendix contains all the extra information regarding the experimental setup and procedure.

D.1 Detailed experimental procedure

The detailed experimental procedure followed during the experiments, may described as follows:

1. The Electro-Automatik BCI 84-40R programmable battery charger was switched on and programmed to supply a constant current of 25 A.

2. The Agilent 34972A TDAS was plugged in, switched on and allowed to initialize. After initialization the instrument was connected to the Agilent Benchlink data logger software and data recording was initiated.

3. The Arduino IDE software was opened and connected to the Generic UNO R3 microcontroller connected to the computer via the USB port. During this stage the emergency stop connected to the relays was engaged preventing any charging or discharging.

4. The PLX-DAQ software was opened and connected to the Generic UNO R3 microcontroller.

5. The Arduino IDE code was uploaded to the microcontroller and the emergency stop was released.

6. The charge/discharge cycle was allowed to continue for approximately 4 hours, at which point the 24 V CPU fan was switched on. This step was ignored for the second part of the experiment where the fan was on from the start.

7. When the temperatures reached equilibrium the TDAS was stopped and the data was exported to an Excel® file and saved. Afterwards the Agilent 34972A TDAS was switched off

8. The Electro-Automatik BCI 84-40R programmable battery charger was switched off.

9. The emergency stop was pressed and the microcontroller USB disconnected from the computer.

10. Finally the lid of the polystyrene foam box was removed to allow the cells to cool down to ambient temperature.

D.2 Experiment 1: Thermocouple locations

The thermocouple locations for the first experiment are shown in Figures D.1, D.2 and D.3.

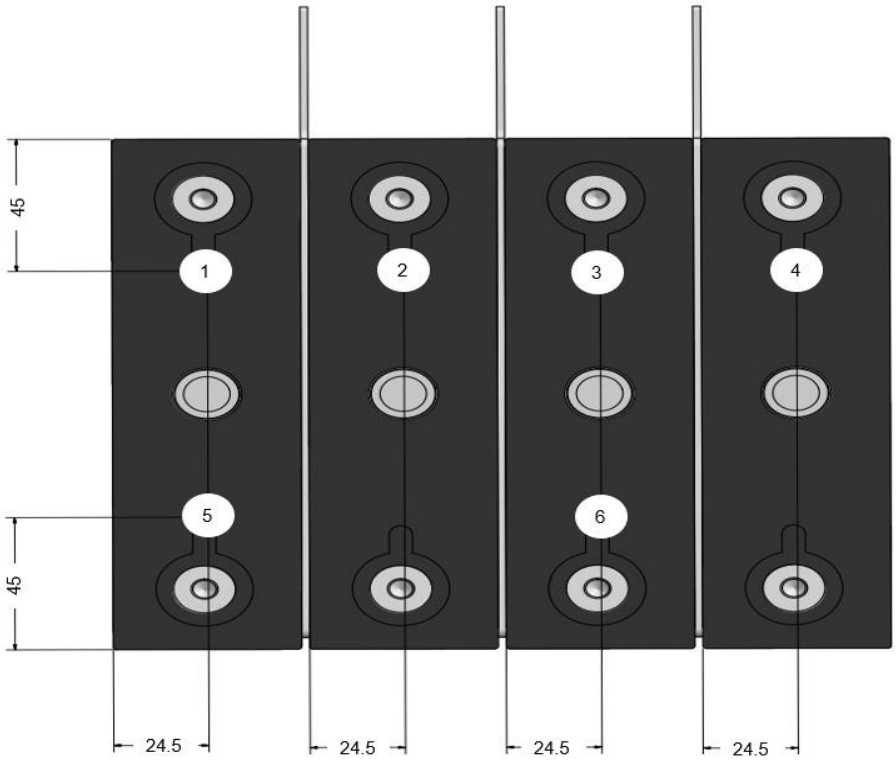

Figure D.1: Cell thermocouple locations for the first experiment

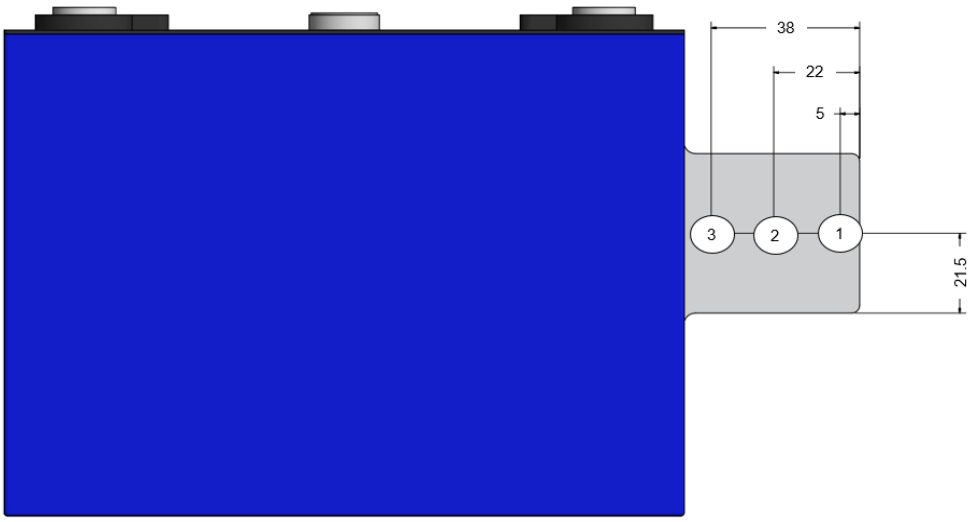

Figure D.2: Fin thermocouple locations

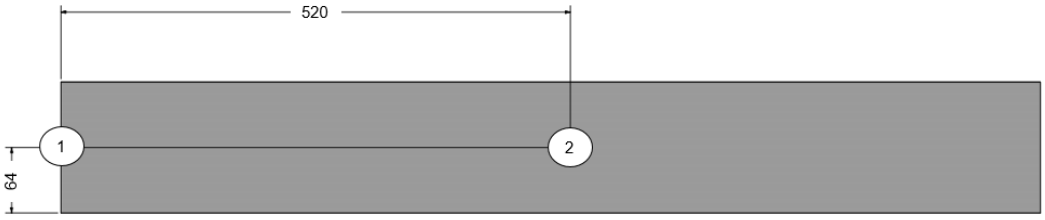

Figure D.3: Cooling channel thermocouple locations

D.3 Experiment 2: Thermocouple locations

The thermocouple locations for the second experiment can be seen in Figures D.4 and D.5. The locations of the thermocouples in the cooling channel stayed the same.

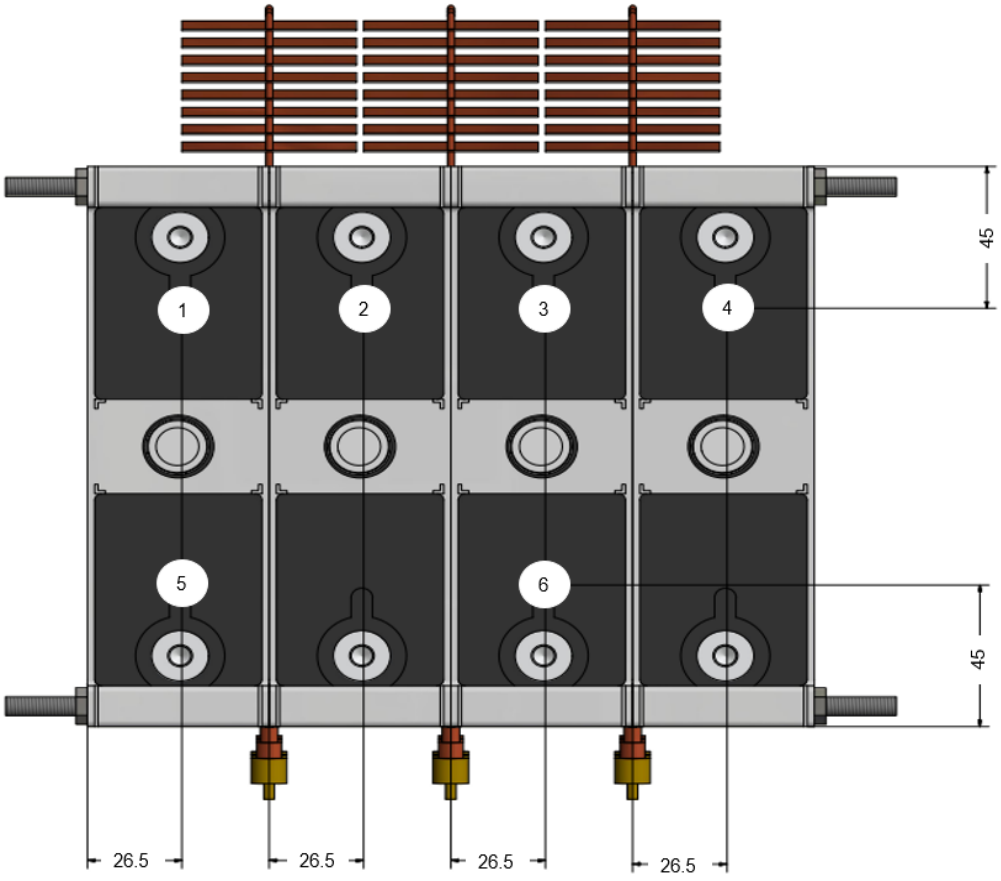

Figure D.4: Cell thermocouple locations for the second experiment

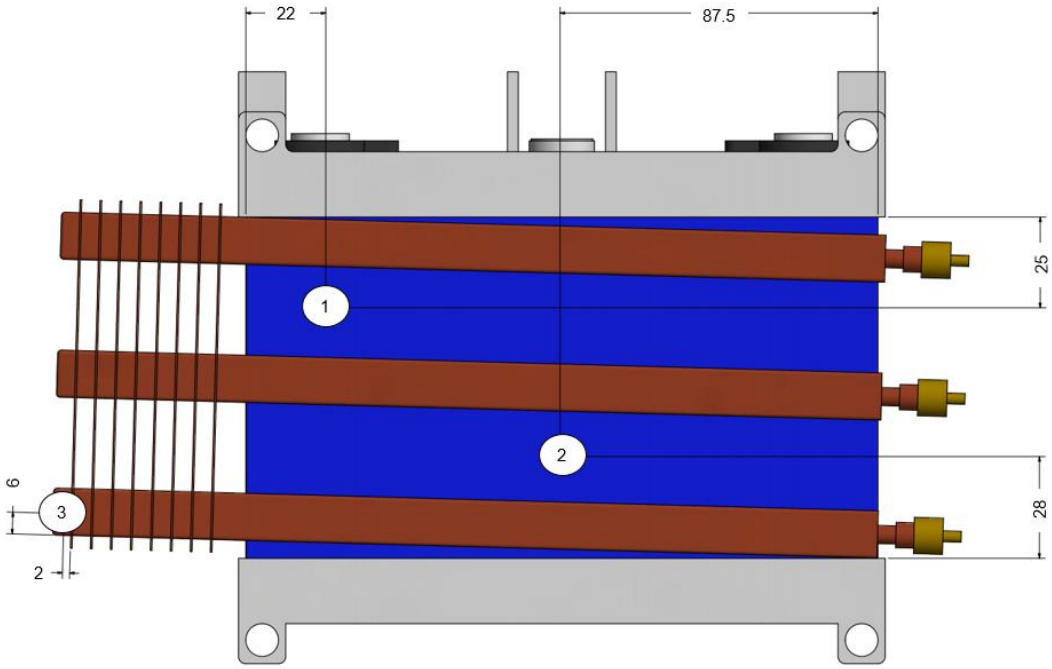

Figure D.5: Thermosyphon heat pipe thermocouple locations

D.4 Arduino Code

Figure D.6 and D.7 indicates the important Arduino IDE code.

```
void loop()
{
  // put your main code here, to run repeatedly:

  ////////////////////////////////////////////////////////////////////////////////////////////

  Vc1 = (analogRead(A0)*(5.0/1023)*(2))-0.28;
  delay(10);

  Vc2 = (analogRead(A1)*(5.0/1023)*(14.7/4.7))-Vc1-0.8;
  delay(10);

  Vc3 = (analogRead(A2)*(5.0/1023)*(6.7/2))-Vc1-Vc2-0.7;
  delay(10);

  Vc4 = (analogRead(A3)*(5.0/1023)*(5.7/1))-Vc1-Vc2-Vc3-1.0;
  delay(10);

  filterValue1 = filterPrevious1+(a*(Vc1-filterPrevious1));
  filterPrevious1 = filterValue1;

  filterValue2 = filterPrevious2+(a*(Vc2-filterPrevious2));
  filterPrevious2 = filterValue2;

  filterValue3 = filterPrevious3+(a*(Vc3-filterPrevious3));
  filterPrevious3 = filterValue3;

  filterValue4 = filterPrevious4+(a*(Vc4-filterPrevious4));
  filterPrevious4 = filterValue4;
```

Figure D.6: Arduino voltage divider and filter code

```
    if (counter2 >= 300)
  {

    if ((filterValue1 > 3.5)||(filterValue2 > 3.5)||(filterValue3 > 3.5)||(filterValue4 > 3.5))
    {
     relay_SetStatus(ON, ON, OFF );//turn on relay 1 and 2 to discharge
    }
    else if ((filterValue1 < 2.8)||(filterValue2 < 2.8)||(filterValue3 < 2.8)||(filterValue4 < 2.8))
    {
      relay_SetStatus(OFF, OFF, ON);//turn on relay 3 to charge
    }

void relay_init(void)//initialize the relay
{
  //set all the relays OUTPUT
  pinMode(IN1, OUTPUT);
  pinMode(IN2, OUTPUT);
  pinMode(IN, OUTPUT);
  relay_SetStatus(OFF, OFF, OFF); //turn off all the relays
}

//set the status of relays
void relay_SetStatus( unsigned char status_1,  unsigned char status_2, unsigned char status_3)
{
  digitalWrite(IN1, status_1);
  digitalWrite(IN2, status_2);
  digitalWrite(IN, status_3);

}
```

Figure D.7: Arduino relay control code

Appendix E: Thermocouple calibration

As mentioned in Section 6.1, the calibration was done using a Fluke® 9142 calibration machine. Since the cell temperature was not expected to differ much from the ambient conditions, the set point temperature range was set between 5 °C and 50 °C.

The Resistance Temperature Detector (RTD) temperature can be calculated from the corresponding resistance using the following formula:

$$T_{RTD} = 0.00111611R^2 + 2.32652102R - 243.7648049 \qquad \text{(E.1)}$$

where R is the relevant resistance. Table E.1 shows the temperature and resistance values of the RTD for each reference temperature. TCR refers to the temperature of the corresponding resistance.

Table E.1: T_{RTD} for each reference temperature

Reference temperature [°C]	Resistance [Ω]	TCR [°C]
5	101,977	5,094
10	103,916	10,050
15	105,855	15,015
20	107,794	19,989
25	109,716	24,927
30	111,637	29,871
35	113,588	34,900
40	115,539	39,938
45	117,463	44,915
50	119,389	49,905

The thermocouple measurements for each reference temperature is shown in Table E.2.

Table E.2: Measured thermocouple temperatures

Reference Temperature [C]	T1	T2	T3	T4	T5	T6	T7	T8	T9
5	4,708	4,769	4,791	4,795	4,996	4,791	4,793	4,760	4,747
10	9,415	9,539	9,582	9,590	9,993	9,582	9,585	9,519	9,494
15	14,385	14,465	14,518	14,555	14,740	14,521	14,543	14,502	14,476
20	19,354	19,391	19,455	19,520	19,488	19,461	19,501	19,485	19,458
25	24,348	24,353	24,433	24,522	24,471	24,445	24,494	24,497	24,470
30	29,341	29,314	29,412	29,523	29,454	29,429	29,487	29,508	29,482
35	34,381	34,317	34,425	34,556	34,422	34,438	34,500	34,531	34,507
40	39,420	39,321	39,438	39,589	39,390	39,446	39,513	39,554	39,532
45	44,422	44,287	44,424	44,592	44,349	44,436	44,509	44,567	44,549
50	49,425	49,252	49,409	49,595	49,309	49,426	49,504	49,580	49,566
Reference Temperature [C]	**T10**	**T11**	**T12**	**T13**	**T14**	**T15**	**T16**	**T17**	**T18**
5	4,759	4,824	4,805	4,713	4,678	4,688	4,718	4,682	4,629
10	9,519	9,649	9,611	9,426	9,356	9,377	9,435	9,363	9,258
15	14,499	14,582	14,533	14,394	14,340	14,355	14,379	14,248	14,195
20	19,479	19,514	19,455	19,362	19,324	19,332	19,323	19,133	19,132
25	24,481	24,485	24,418	24,362	24,332	24,325	24,309	24,099	24,097
30	29,482	29,456	29,380	29,363	29,340	29,317	29,295	29,065	29,063
35	34,505	34,521	34,446	34,375	34,358	34,319	34,297	34,054	34,043
40	39,529	39,586	39,512	39,387	39,376	39,320	39,300	39,043	39,022
45	44,543	44,551	44,469	44,385	44,381	44,311	44,285	44,005	43,989
50	49,558	49,516	49,425	49,382	49,386	49,302	49,270	48,967	48,955

Table E.3 shows the difference between the measured and RTD temperatures.

Table E.3: Temperature corrections of the thermocouples

Reference temperature [C]	T1	T2	T3	T4	T5	T6	T7	T8	T9
5	0,386	0,324	0,303	0,299	0,097	0,302	0,301	0,334	0,346
10	0,635	0,512	0,468	0,461	0,058	0,468	0,465	0,531	0,556
15	0,631	0,550	0,497	0,460	0,275	0,494	0,472	0,513	0,539
20	0,635	0,597	0,534	0,469	0,501	0,528	0,488	0,503	0,531
25	0,579	0,574	0,494	0,405	0,456	0,482	0,433	0,430	0,457
30	0,530	0,557	0,459	0,347	0,417	0,442	0,384	0,363	0,389
35	0,520	0,583	0,475	0,344	0,478	0,463	0,400	0,369	0,393
40	0,518	0,617	0,500	0,349	0,548	0,492	0,425	0,385	0,406
45	0,493	0,628	0,491	0,323	0,566	0,479	0,406	0,348	0,366
50	0,480	0,653	0,496	0,310	0,596	0,479	0,401	0,325	0,339
Reference temperature [C]	**T10**	**T11**	**T12**	**T13**	**T14**	**T15**	**T16**	**T17**	**T18**
5	0,334	0,269	0,288	0,381	0,416	0,405	0,376	0,412	0,464
10	0,531	0,402	0,439	0,624	0,694	0,673	0,615	0,687	0,792
15	0,516	0,434	0,482	0,621	0,675	0,661	0,636	0,767	0,820
20	0,509	0,475	0,534	0,627	0,665	0,656	0,666	0,856	0,857
25	0,447	0,442	0,509	0,565	0,595	0,602	0,618	0,828	0,830
30	0,389	0,415	0,491	0,508	0,531	0,554	0,576	0,806	0,808
35	0,395	0,380	0,454	0,526	0,543	0,582	0,603	0,846	0,858
40	0,410	0,353	0,426	0,551	0,562	0,618	0,639	0,896	0,916
45	0,372	0,364	0,446	0,530	0,534	0,604	0,630	0,910	0,926
50	0,347	0,389	0,480	0,523	0,519	0,603	0,635	0,938	0,950

Based on the temperatures in Table E.3, the average temperature correction for each thermocouple is shown in Table E.4.

Table E.4: Average temperature corrections of each thermocouple

	T1	T2	T3	T4	T5	T6	T7	T8	T9
Average temperature difference	0,541	0,560	0,472	0,377	0,399	0,463	0,418	0,410	0,432
	T10	**T11**	**T12**	**T13**	**T14**	**T15**	**T16**	**T17**	**T18**
	0,425	0,392	0,455	0,546	0,574	0,596	0,600	0,795	0,822

Appendix F: Uncertainty Analysis

The uncertainty analysis of the experimental measurements and derived correlations is presented in this Appendix. The uncertainty of the calculated properties and relationships was established from the accuracy of the measurement equipment.

A similar method to Panchal (2016) was used to calculate the overall uncertainty of the experimental results and the theoretical predictions. According to this method, the result R of an experiment is determined from a set of measurements as:

$$R = R(X_1, X_2, X_3, \dots, X_N) \tag{F.1}$$

Each measurement can be expressed as $X_i \pm \delta X_i$, where δX_i is the uncertainty. Therefore the effect of each measurement error was determined as follows:

$$\delta R_{Xi} = \frac{\delta R}{\delta X_i}\delta X_i \tag{F.2}$$

Therefore the overall uncertainty δR can be determined by:

$$\delta R = \left[\sum_{i=1}^{N}\left(\frac{\delta R}{\delta X_i}\delta X_i\right)^2\right]^{1/2} \tag{F.2}$$

If the result can be described by an equation with the form $R = X_1^a X_2^b X_3^c \dots X_N^m$ then the overall uncertainty can be determined directly from the set of individual uncertainties as:

$$\frac{\delta R}{R} = \left[\left(a\frac{\delta X_1}{X_1}\right)^2 + \left(b\frac{\delta X_2}{X_1}\right)^2 + \cdots + \left(m\frac{\delta X_N}{X_1}\right)^2\right]^{1/2} \tag{F.4}$$

The average surface temperature was calculated using:

$$T_{s,avg} = \frac{\sum(T_{ij}A_{ij})}{A_{tot}} \tag{F.5}$$

To determine the overall uncertainty of the measured average surface temperatures, the uncertainty of the temperature measurements and area measurements was required. These uncertainties were calculated as follows:

1. **Surface temperature, T_{ij}**

   The surface temperature measurements were made with T-type thermocouples and recorded with an Agilent© 34972A thermal data

acquisition system (TDAS). According to the Agilent© User Manual, the uncertainty of the readings is 1 °C. The uncertainty was calculated using:

$$\frac{\delta T}{T} = \frac{1\ °C}{T[°C]} \tag{F.6}$$

2. **Area, A_{ij}**

The areas were measured with a stainless steel ruler, with a resolution of 0.5 mm. Since the areas were calculated as $A_{ij} = wl$, the uncertainty was determined with:

$$\frac{\delta A}{A} = \pm\left[\left(\frac{\delta w}{w}\right)^2 + \left(\frac{\delta l}{l}\right)^2\right]^{1/2} \tag{F.7}$$

To determine the uncertainty in the average surface temperature, let the individual $T_{ij}A_{ij}/A_{tot}$ components be represented by P_{ij}. The error in each P_{ij} product was then determined by:

$$\frac{\delta P_{ij}}{P_{ij}} = \pm\left[\left(\frac{\delta T_{ij}}{T_{ij}}\right)^2 + \left(\frac{\delta A_{ij}}{A_{ij}}\right)^2 + \left(\frac{\delta A_{tot}}{A_{tot}}\right)^2\right]^{1/2} \tag{F.8}$$

The total surface uncertainty was calculated using:

$$\frac{\delta T_{s,avg}}{T_{s,avg}} = \pm\left[\left(\frac{\delta P_1}{P_1}\right)^2 + \left(\frac{\delta P_2}{P_2}\right)^2 + \cdots + \left(\frac{\delta P_N}{P_N}\right)^2\right]^{1/2} \tag{F.9}$$

The uncertainty sample results of the temperature measurements are shown in Table F.1.

Table F.1: Surface temperature uncertainty results

Surface temperature [°C]	Relative Uncertainty [%]	Absolute Uncertainty [°C]
20	0,7416	0,1483
22	0,627	0,1379
24	0,5399	0,1296
26	0,4722	0,1228
28	0,4185	0,1172
30	0,3752	0,1126

The uncertainty analysis presented above was also used for determining the uncertainty of the mass flow rate of the air, the heat generation and heat dissipation

rate. It was assumed that the anemometer had an accuracy of 95% in the mass flow rate measurements. A summary of these results is shown in Table F.2.

Table F.2: Uncertainty of calculated properties

Variable [Units]	Range	Relative Uncertainty [%]	Absolute Uncertainty
Mass flow rate [kg/s]	0,0872-0,1009	12,2474	0,0107-0,0124
Heat generated [W]	1.975-2.744	8,6603	0.171-0.2376
Heat transferred [W]	0.7451-18.55	7,5798	0.0564-1.406

Appendix G: Convergence

This appendix contains the convergence levels of the Computational Fluid Dynamics (CFD) simulations of the aluminium plate and Thermosyphon Heat Pipe (THP) Battery Thermal Management System (BTMS).

G.1 Aluminium plate BTMS convergence

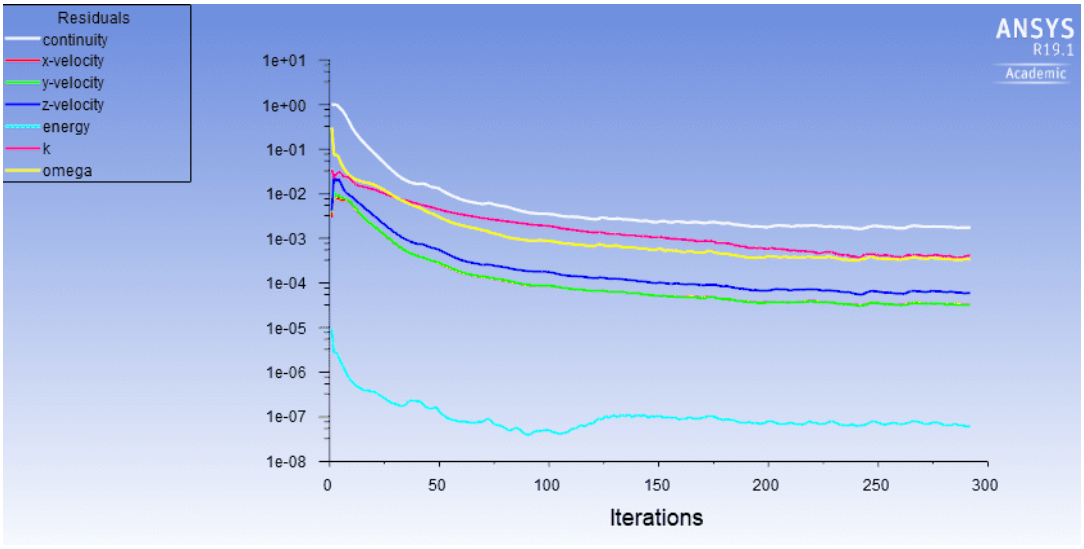

Figure G.1: Residual plot of the aluminium plate BTMS simulations

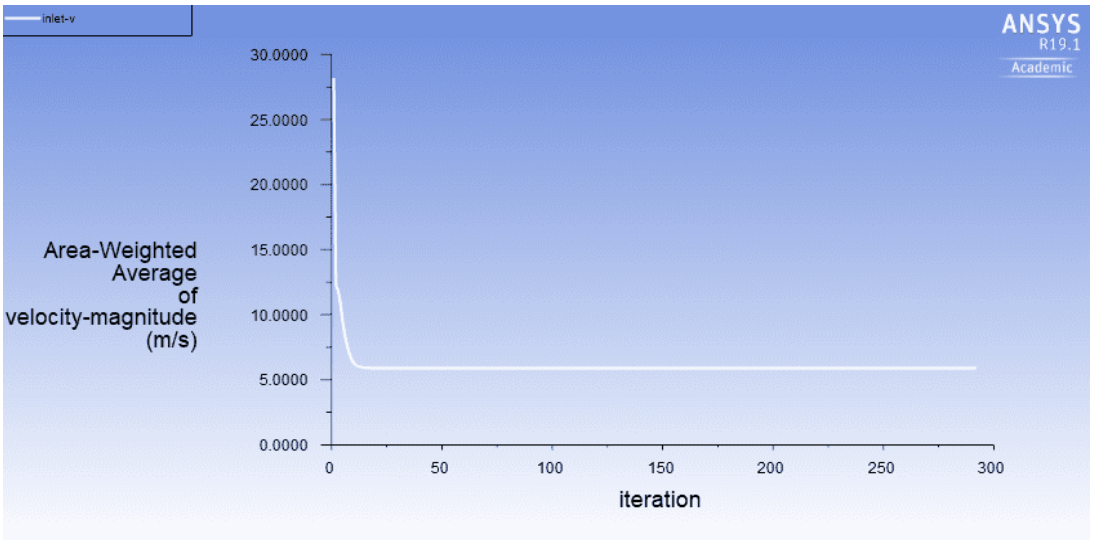

Figure G.2: Inlet velocity convergence of the aluminium plate BTMS simulations

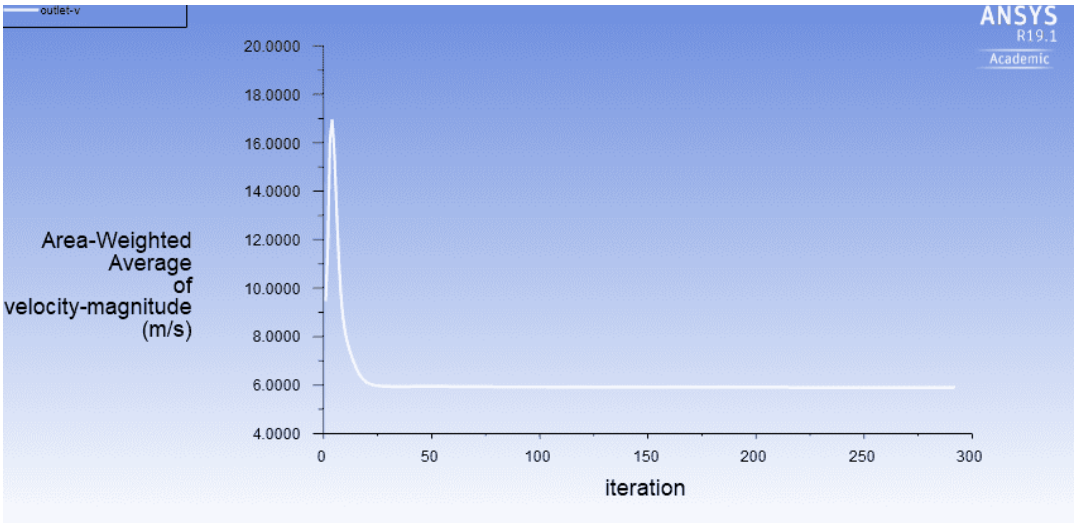

Figure G.3: Outlet velocity convergence of the aluminium plate BTMS simulations

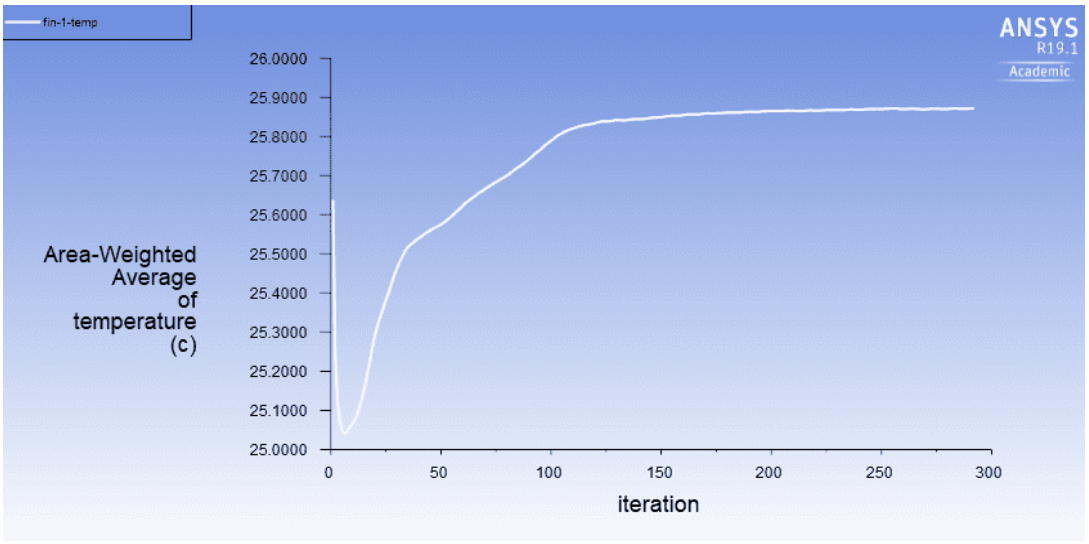

Figure G.4: Fin temperature convergence of the aluminium plate BTMS simulations

G.2 THP BTMS convergence

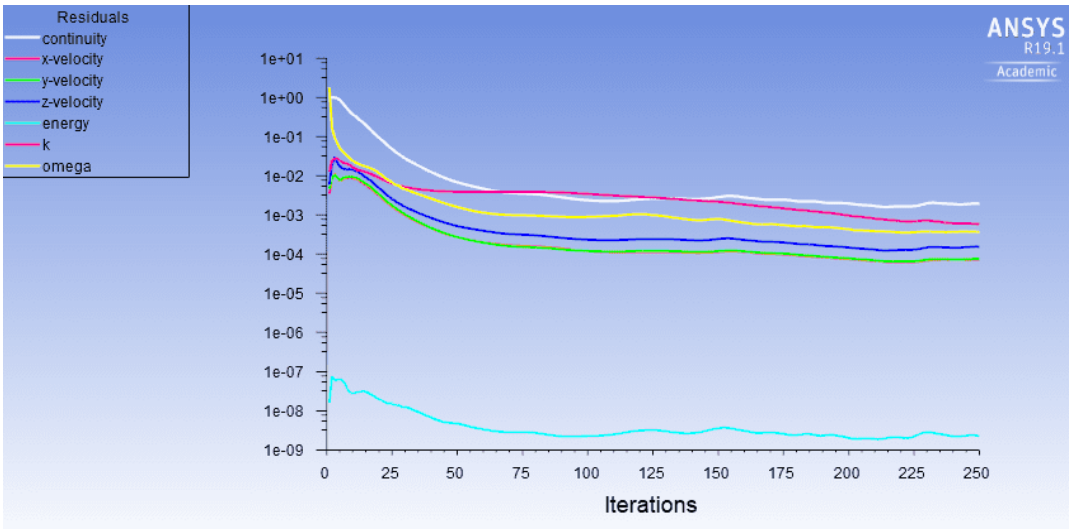

Figure G.5: Residual plot of the THP BTMS simulations

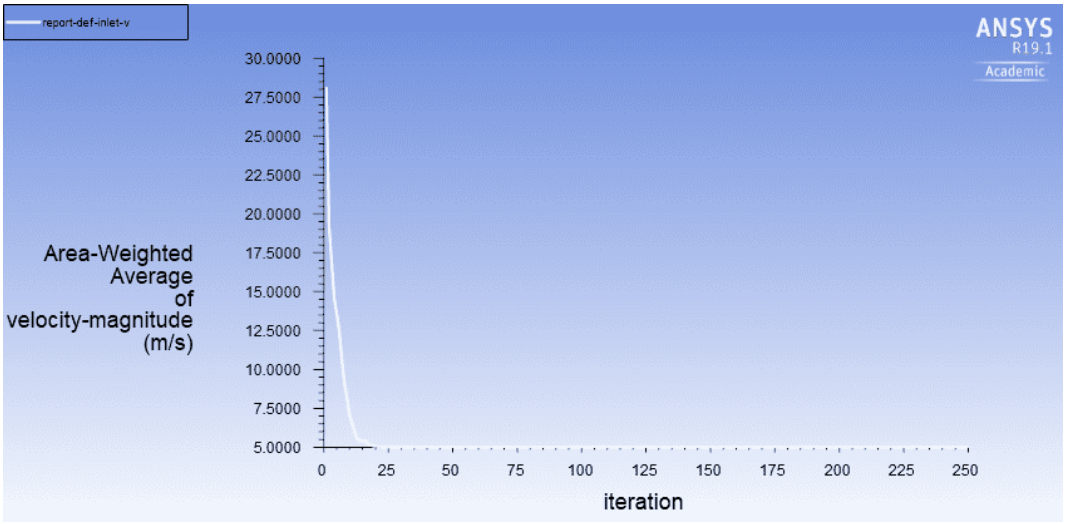

Figure G.6: Inlet velocity convergence of the THP BTMS simulations

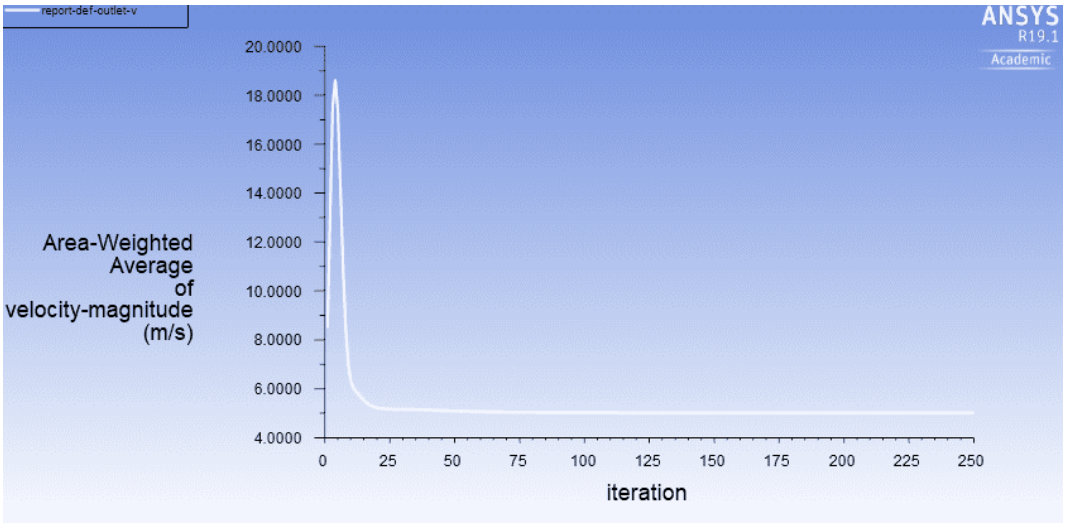

Figure G.7: Outlet velocity convergence of the THP BTMS simulations

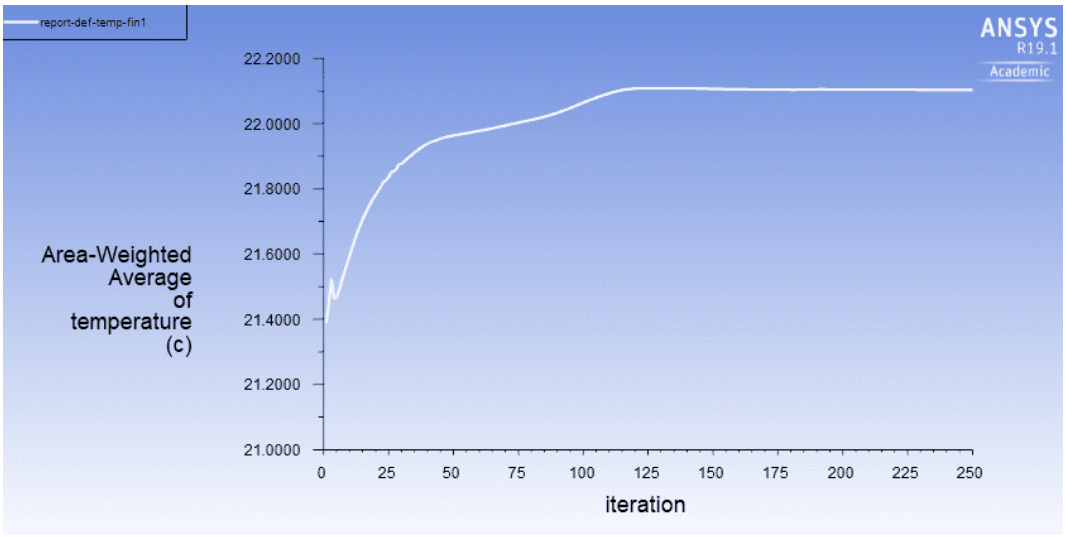

Figure G.8: Fin temperature convergence of the THP BTMS simulations